MULTIFUNCTIONAL BIOMATERIAL TECHNOLOGIES WITH SUSTAINED DRUG DELIVERY FOR DIVERSE PERIODONTAL AND CRANIOFACIAL REGENERATION APPLICATIONS

Seth Woodbury

04/21/2023

This thesis has been read and approved by Prof. Yuji Mishina.

Signed:  Date: 04 / 21 / 2023

Faculty advisor email: mishina@umich.edu Phone: (734) 763–5579

Acknowledgements

The last four years of my life at the University of Michigan have been some of best and most memorable years of my life, even amidst the COVID-19 pandemic. Somehow, I managed to begin my wonderful journey in the Mishina lab during the first completely virtual semester of the pandemic. I will never forget how excited I was when I saw Ben's UROP posting for a biomaterials and tissue engineering research position in the lab; I had no idea such a field even existed, but it immediately became my dream lab. The concept of tissue regeneration sounded like something out of futuristic science-fiction or a superhero movie, and too be honest it still excites me like that. Thus, I am bittersweet as I spend my last few weeks on campus and in the Mishina lab before I move to Seattle to begin my Ph.D. in bioengineering at the University of Washington. I would have never found myself on this track had it not been for this experience, and for that I will always be grateful.

The first person to whom I owe the greatest deal of gratitude towards is my graduate student mentor, Ben Swanson. You were the one who decided to take a chance on me in the lab and you have invested countless hours from your packed D.D.S-Ph.D. class/clinical schedule into mentoring me, assisting me with my projects, and helping me with my life goals. You are a role model to me and you have pushed me to become a better student, scientist, and adult. I have had so much fun designing new projects with you and you have taught me so many invaluable skills. You believed in me and entrusted me with the freedom to pursue my own curiosities and passions in lab; I would not give up this experience or our bond for anything, and I sincerely hope to maintain a tight connection with you after graduation.

Next, I would like to thank my faculty mentor and lab principal investigator, Prof. Yuji Mishina. You are the most passionate scientist that I have ever met and it has always inspired me.

I respect how you treat everyone in the lab with as an intellectual equal, whether an undergraduate or graduate student; it has pushed me to mature as a research scientist and given me the confidence to pursue my own projects and ideas in lab. You have always supported my passions and projects in addition to providing wise and insightful advice when I needed it. I feel highly prepared for graduate school coming out of your lab, and I hope to work under a principal investigator that has similar qualities to you.

In addition, I would like to acknowledge all of my labmates in the Mishina lab for creating a pleasant research environment and always helping me when I asked for it. I would like to especially thank Lindsey Douglas for assisting me with the image analysis and staining experiments for the thermosensitive scaffold project in Chapter 3, which yielded powerful results that are ultimately the backbone of the project. Additionally, I would like to thank Coral Chen and Jaylynn Jones for helping me with the paraffin sectioning of the explanted scaffolds after the *in-vivo* experiment, which allowed for the scaffolds to be stained and visualized. I also owe a huge thank you to Jackson Albright for significantly contributing to the micro-computed tomography analysis of Chapter 2, which demonstrated the incredible results that our technology exceeded an FDA-approved commercial technology at regenerating periodontal bone tissue. Jackson, it has been a pleasure teaching you scaffold fabrication this year and I am excited to see where you will take these projects next after I leave.

It is also important that I express gratitude to Prof. Marco Bottino and his lab for allowing me to use their UV crosslinking chamber, which I used in the fabrication of every thermosensitive shape-memory (TSM) biomaterial construct of this thesis. You have been one of the kindest people that I have had the pleasure of meeting during my undergraduate career and you were genuinely excited to help me succeed. Everyone in your lab was so respectful and kind to me when I used

the crosslinking chamber, it was always a pleasure to interact with them. Finally, I am extremely grateful for Dr. Renan Dal Fabbro's assistance with the *in-vitro* seeding experiments of Chapter 1 and his continued guidance and contribution to the *in-vivo* experiments of Chapter 2 demonstrating our tissue engineering membrane technology.

To the Undergraduate Research Opportunities Program (UROP) and the Honors Program, I would have never found the Mishina lab or had the unique undergraduate opportunity to conduct a thesis without the support from these wonderful programs. I will forever be thankful for the UROP Travel Grants, which allowed me to present at the 2022 Society For Biomaterials National Conference in Baltimore, MD and to virtually attend the 2022 American Association for Dental Research National Conference. Additionally, my undergraduate thesis dissertation research was continually supported by funding from the Honors Program over four semesters in the form of generous donations from alumni. I also appreciate the Office of Innovation Partnerships at the University of Michigan for funding and assisting Ben, Dr. Mishina, and me with the intellectual property protection of the biomaterial technologies that resulted from my thesis dissertation research. This was one of my proudest achievements and I still cannot appreciate how lucky I am to be a named inventor on a provisional patent, which will soon be filed for a utility patent at the end of April, 2023.

Lastly, I want to thank all of my family and friends for creating an undergraduate experience and memories that I will always cherish. To my five roommates from 1137 Michigan Avenue, you guys are my best friends and like brothers to me. We shared an incredible dynamic and camaraderie that I am not sure I will ever find again in my life. I am overcome with nostalgia and happiness when thinking about the fun and wild experiences that we shared, I would not change a single detail or trade it for anything. As for this year, I want to give a shoutout to my

amazing residents on 6th Bush Hall in South Quad where I am an Honors Resident Advisor at. In addition, I am so glad to have met Elizabeth Tolrud, Carrie Ciarelli, and Geoffrey Batterbee through this position, who have been phenomenal co-workers and have become dear friends to me this year. Last but not least, I want to thank my mother, father, step-father, and four younger siblings for their unconditional support, encouragement, and love. When times were rough, you all were there to help me preserve and succeed, especially you, mom. It is finally over, we did it.

There are many other influential people in my life that I could not thank or shout out in this brief acknowledgement. Nonetheless, I am extremely grateful for each and every one of you as none of this could have been possible without your support.

Table of Contents

Chapter 1

Development and Characterization of a Biphasic Biomaterial with Nanofibers and a Capacity for Thermosensitive Shape Memory in a Thin Film Construct

1.1 Abstract

This chapter presents a series of biomaterial constructs optimized from a semi-interpenetrating network of PCL-diacrylate (PCL-DA) in PLLA to possess thermal shape memory (TSM) and nanofiber formation through thermally-induced phase separation. The TSM biomaterials exhibited thermosensitive properties at temperatures above 50C, enabling them to attain a rubbery state with better shaping properties or to recover its memorized shape via shape memory. Additionally, the TSM biomaterial membrane displayed biphasic morphology with a smooth top and nanofibrous bottom, a unique property arising from the partial phase separation of PCL-DA and PLLA. This created biphasic hydrolytic degradation in the thin films dictated by the differing hydrophilicities of PLLA and PCL-DA. The incorporation of PLGA-diacrylate (PLGA-DA) into the PCL-DA semi-interpenetrating network within PLLA increased the overall TSM biomaterial hydrophilicity without compromising its shape memory properties, the biphasic morphology, or the biphasic hydrolytic degradation. *In-vitro* experiments confirmed that the nanofibrous bottom layer of the TSM biomaterial thin film supported the proliferation of bone marrow-derived stem cells and periodontal ligament stem cells to the same extent as PLLA thin films, while the smooth top layer of the TSM biomaterial thin films served as a barrier to these stem cells. This unique biomaterial construct holds potential for niche tissue engineering or drug delivery applications, and further exploration is warranted to determine its efficacy in these domains.

1.2 Introduction

One of the most difficult challenges to address in the field of biomaterials and tissue engineering is the ability to clinically-handle and shape biomaterial constructs to patient defects without destroying the desirable properties of the construct.[1,8,9,20,26] Shape memory is the process by which a material can recover its physical properties after being chemically or physically programmed to remember that property.[1,26] Shape memory is a growing strategy that seeks to address the clinical-handling problem of biomaterials.[8,26] The aim of shape memory in the biomaterials and tissue engineering field is to create a biomaterial with certain physical attributes (e.g., macropores) that can be recovered via shape memory *in-vivo* after implantation.[1,8,9,19,25]

A memorized shape can be often programmed into a biomaterial by crosslinking it during construct fabrication to create a low-energy conformation state.[1,8,25] However, the biomaterial must be reactive some stimulus that relaxes its crosslinked network such that the polymer chains can be physically moved or rearranged. This not only allows the biomaterial to be shaped after it receives the stimulus, but the stimulus will also trigger its shape memory after the biomaterial receives a deformation.[1,8,9,19,25] This has been commonly demonstrated with the biomaterial poly-ε-caprolactone-diacrylate (PCL-DA), which can be photocrosslinked to create a memorized shape. Furthermore, PCL-DA has a low melting point between 50 and 60C, which allows its shape memory to be activated by heat at or above these temperatures.[1,25] PCL-DA is a good candidate shape memory biomaterial, but it has a smooth surface topology that is not favorable for stem cell adhesion and proliferation.[1,8,9]

Stem cells typically prefer nanofibrous biomaterials that resemble the extracellular matrices found in the human body, which have high surface areas for stem cell adhesion. Poly-*L*-lactide is one of the most widely used biomaterials because of its high crystallinity which allows it to

undergo thermally-induced phase separation (TIPS) at low temperatures in the correct organic solvent (e.g., tetrahydrofuran (THF)) to form homogenous nanofibers that resemble the dimensions of collagen nanofibers in trabecular bone.[14,15,16] Due to this property, PLLA can be casted onto constructs of any shape or size and will form homogenous nanofibers throughout the entire construct through TIPS just by cooling the construct enough for PLLA to undergo spinodal decomposition and to recrystallize out of organic solution.[13,14,15,16] PLLA is also an FDA-approved material because it is highly biocompatible. Thus, PLLA is a cheap, accessible biomaterial capable of spontaneously forming homogenous nanofibers in any construct, which makes it scalable.[13,14,16]

However, PLLA is fairly brittle and lacks good clinical handling properties.[13,14,16] This makes the biologically favorable aspects PLLA biomaterial constructs (e.g., scaffold macropores) highly prone to destruction upon clinical-shaping and implantation. Thus, the aim of this chapter was to create an optimized biomaterial out of PLLA and PCL-DA that exhibits nanofibers formed through TIPS and a macroscopic construct capable of thermal shape memory at clinically relevant temperatures. This chapter focused on optimizing this biomaterial in a two-dimensional (2D) thin film because of its convenience of fabrication and characterizing physical properties like thermal shape memory. 2D biomaterials are highly relevant in the field of tissue engineering for many applications like skin grafting, periodontal regeneration, and adhesions. Thus, this biomaterial sought to be developed, well-characterized, and well-understood in its 2D thin film construct with the intention of directly applying it to a tissue engineering problem.

1.3 Results and Discussion

1.3.1 Thermally Induced Nanofibers in a Thermosensitive Shape Memory Biomaterial

It was hypothesized that a biomaterial capable of thermal shape memory and thermally induced phase separation (TIPS) nanofiber formation could be synthesized from a semi-interpenetrating network of poly-*L*-lactide (PLLA) and poly-ε-caprolactone-diacrylate (PCL-DA), where the PCL-DA is interpenetrating and crosslinked within a PLLA matrix (**Figure 1.1D**). This strategy aimed to maintain the individual advantageous molecular properties of PLLA (i.e., capacity for TIPS) and PCL (i.e., thermal sensitive properties) by preventing their polymer chains from covalent bonding to form a copolymer while still ensuring that their polymer matrices intermixed to form a mostly homogenous macroscopic material. Furthermore, this strategy was considered advantageous over an interconnected polymer network because it provides more macromolecular freedom of movement in the PCL-DA interpenetrating network to move around since it is not covalently bound to the PLLA matrix, which would give the material better clinical-handling properties. It was also necessary for the PLLA to crystallize during TIPS for the formation of the desirable nanofibrous surface texture, which would not be possible in an interconnected polymer network of PLLA and PCL.

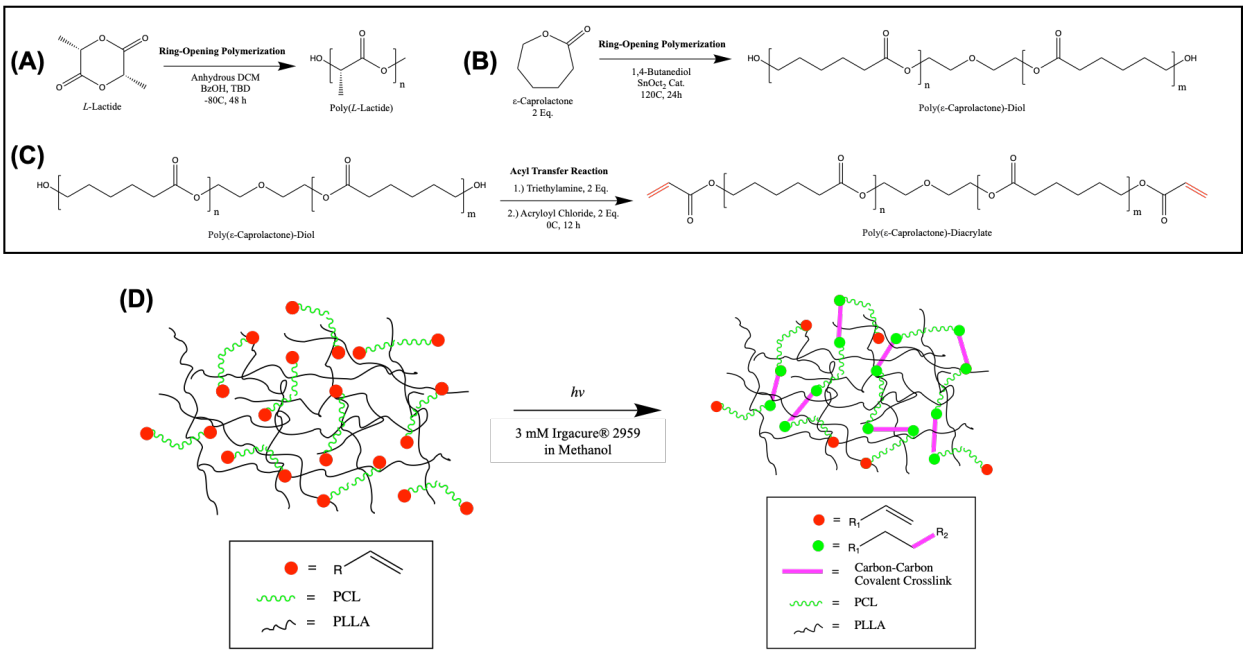

Figure 1.1: Molecular structures and chemical reactions for (A) PLLA, (B) PCL-Diol, and (C) PCL-DA which serve as the biomaterial components for the designed semi-interpenetrating polymer network. (D) The depiction and radical copolymerization synthesis of a semi-interpenetrating network of crosslinked PCL-DA and PLLA from an interpenetrating polymer network PLLA and PC-DA. Note that the pink lines in the semi-interpenetrating network represent the formed crosslinks between acrylate end-groups on PCL-DA.

The thermal shape memory (TSM) biomaterial needed to be optimized for (1) its capacity to form nanofibers through TIPS, (2) its thermosensitive properties, and (3) its shape memory capability. To achieve this, two-dimensional TSM biomaterial films were to be fabricated from varying combinations of PCL-DA and PLLA, where PCL-DA is polymerized *in-situ* via photoinitiated radical chain extension. Although the dimensionality of a biomaterial construct (i.e., 2D vs 3D) has been shown to be an important factor to consider for desirable biological outcomes,[21] it was decided that the fabrication of a two-dimensional biomaterial thin film construct was ideal for TSM biomaterial optimization and pilot testing because of its scalability, conservation of materials and time, simple design for morphology analysis by SEM, and handling convivence for shape memory testing. The thin film size parameters were held consistent by 3D-

printing custom thin film molds that were glued to microscope slides, which were used for TSM biomaterial fabrication (**Figure 1.2A**). The fabrication procedure is detailed in **Figure 1.2B**, where it is noteworthy to mention that the irradiation step imparts the PCL-DA crosslinking and subsequent memorized shape, and that freezing the films at -80C for two days initiates nanofiber formation through TIPS, based on previous methods in the literature.[13,14,15,16]

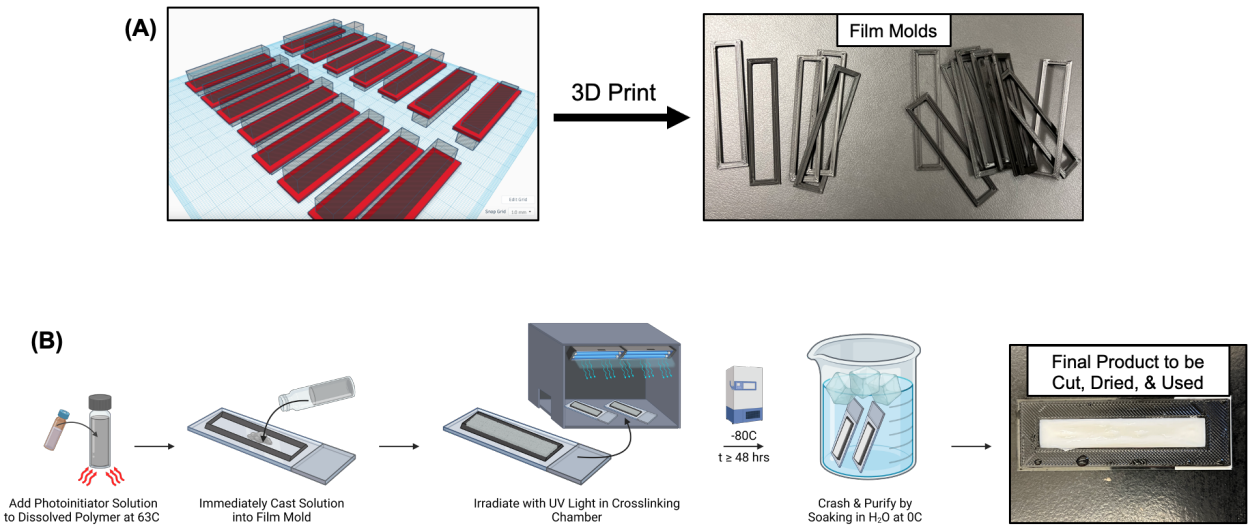

Figure 1.2: (A) Thin film molds designed in TinkerCAD® and their 3D printed structures. The film molds are superglued onto microscope slides to complete the design. (B) Schematic of fabrication procedure for the TSM biomaterial thin films and an image of the end product still in the film mold.

The TSM biomaterial was first optimized for its capacity to form nanofibrous surface topology through TIPS. The first variable that was investigated was the w/w ratio of PCL-DA to PLLA in the polymer blend. The total w/v in THF was fixed at 10% based on previous methods for nanofibrous PLLA scaffold fabrication via TIPS (**Figure 1.3**).[13,14,15,16] SEM was used to evaluate the morphology and surface topology of the fabricated TSM biomaterial film combinations to look for the presence or absence of nanofibers. Unexpectedly, an initial cross section of a 40/60 (40% PCL-DA and 60% PLLA w/w) TSM biomaterial combination revealed a bilayer of opposing surface topologies. Further SEM investigation of each face (i.e., top and bottom) of this thin film

revealed a nanofibrous bottom face and smooth top face (**Figure 1.3A-C**). This was consistently observed among the other TSM biomaterial combinations and was hypothesized to result from a degree of PCL-DA phase separation from PLLA during TIPS, or from contact with the air on the top side of the biomaterial during fabrication.

Nonetheless, the smooth top layer was relatively small in width compared to the nanofibrous bottom layer, demonstrating the bulk of the TSM biomaterial behaved like this. Thus, it was decided to proceed by optimizing the bottom face for nanofibers, since the smooth, thin top layer could be cut off if necessary. Optimizing the PCL-DA to PLLA w/w ratio yielded homogenous, nanofibrous bottom faces in the thin films from the control 0/100 combination (PLLA) up to the 40/60 combination (**Figure 1.3D**). This was a novel result, as any biomaterial blend of PLLA and PCL have never been shown to form nanofibers through TIPS because PCL lacks the specific crystalline properties of PLLA that allow it to form textured and fibrous surfaces.[19] This explains why combinations past 50/50 w/w that were majority-composed by PCL-DA did not form nanofibrous surfaces on the bottom face of the film. It is noteworthy to add that these TSM biomaterial thin films were all fabricated with 10 kDa PCL-DA, which was chosen arbitrarily.

However, the molecular weight of the PCL-DA dictates the crosslinking density and was therefore thought to potentially impact the quality of shape memory. Thus, the 30/70 TSM biomaterial combination was arbitrarily chosen and made from PCL-DA at two additional molecular weights of 2 kDa and 20 kDa to observe if this made an impact on the capacity for nanofiber formation on the bottom face of the thin film (**Figure 1.3E**). This was not observed to drastically impact the ability for nanofibers to form, but the quality of the nanofibers differed slightly. The 2 kDa PCL-DA yielded the thinnest nanofibers while the 20 kDa PCL-DA yielded the thickest nanofibers under these conditions. It was decided that the nanofibers formed under the

conditions using 10 kDa PCL-DA appeared to most closely resemble PLLA nanofibers in the literature, and thus this molecular weight of PCL-DA was used for the remainder of TSM biomaterial thin film fabrication, unless otherwise stated.

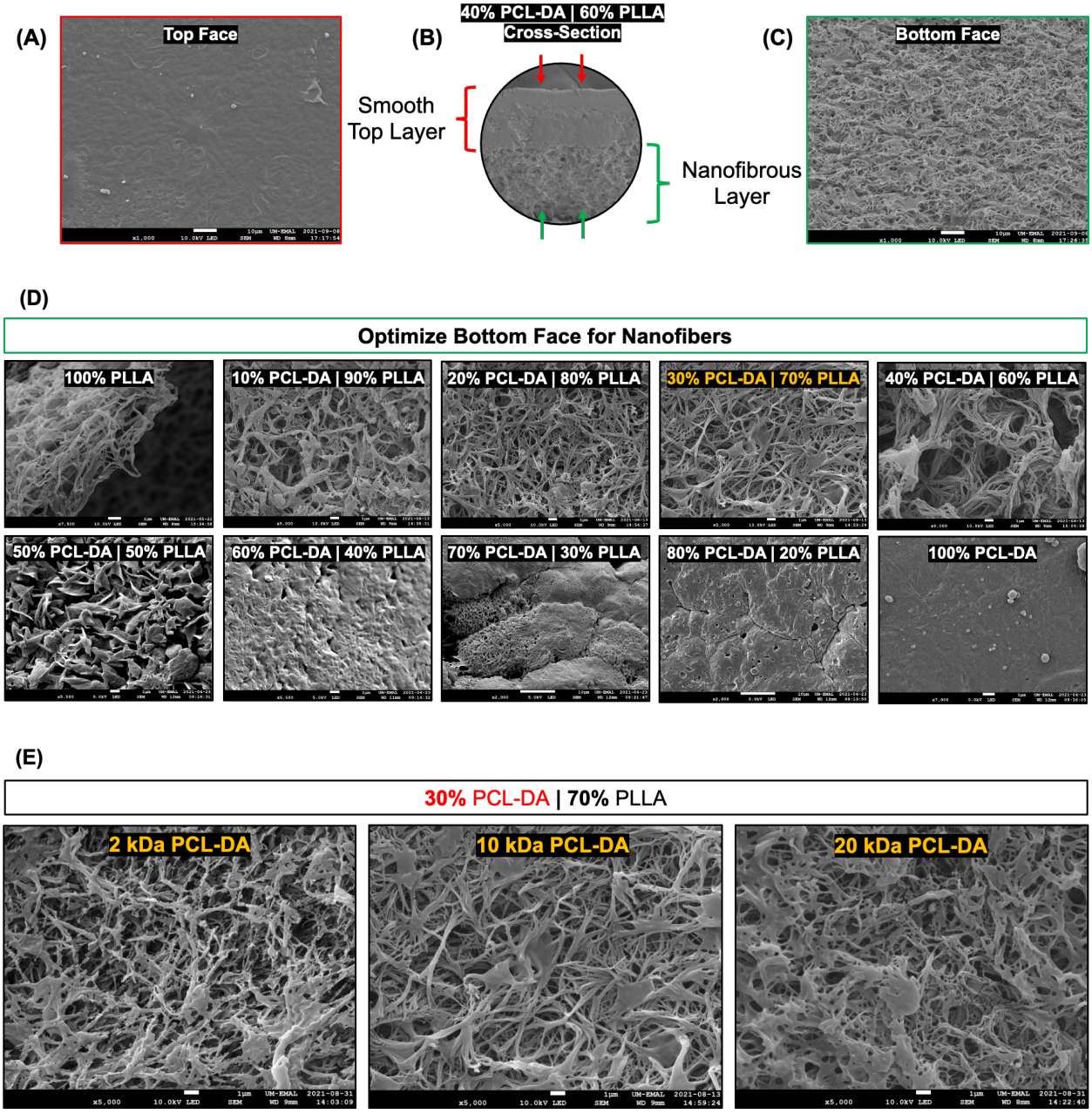

Figure 1.3: SEM surface topology analyses of various TSM biomaterial thin films. (A) SEM image of the top face of a 40/60 w/w film of PCL-DA and PLLA, respectively, demonstrating a smooth surface topology after discovering a bilayer in the (B) SEM image of the cross-section of this thin film. (C) SEM image of the bottom face of the same 40/60 w/w film demonstrating a

nanofibrous surface topology. (D) SEM images of the bottom faces of different w/w combinations of biomaterial thin films composed of PCL-DA and PLLA, respectively. (E) SEM images of the bottom face of TSM biomaterial thin films composed of 30% PCL-DA and 70% PLLA with different molecular weights of PCL-DA.

The tensile modulus of a biomaterial has been extensively demonstrated to be a crucial property in controlling the fate of stem cells, especially skeletal stem cells differentiating towards osteogenic, adipogenic, or chondrogenic fates.[21] Thus, it was desirable to investigate if the TSM biomaterial w/w polymer composition had any effect on the thin film mechanical properties. Only the combinations with nanofibrous bottom faces were investigated. It was observed that the addition of a PCL-DA semi-interpenetrating network to a PLLA matrix significantly strengthened the biomaterial at a 20/80 combination compared to the control PLLA biomaterial thin film, but the other combinations were approximately equivalent in their tensile modulus and did not differ statistically from the PLLA control (**Figure 1.4**). Nonetheless, this suggests that a semi-interpenetrating network of PCL-DA reinforces the PLLA matrix and strengthens the material to a certain point; once the TSM biomaterial starts to become dominated by PCL-DA, the reinforcing effect is outweighed by the lower tensile modulus of PCL-DA, and the material loses mechanical strength.

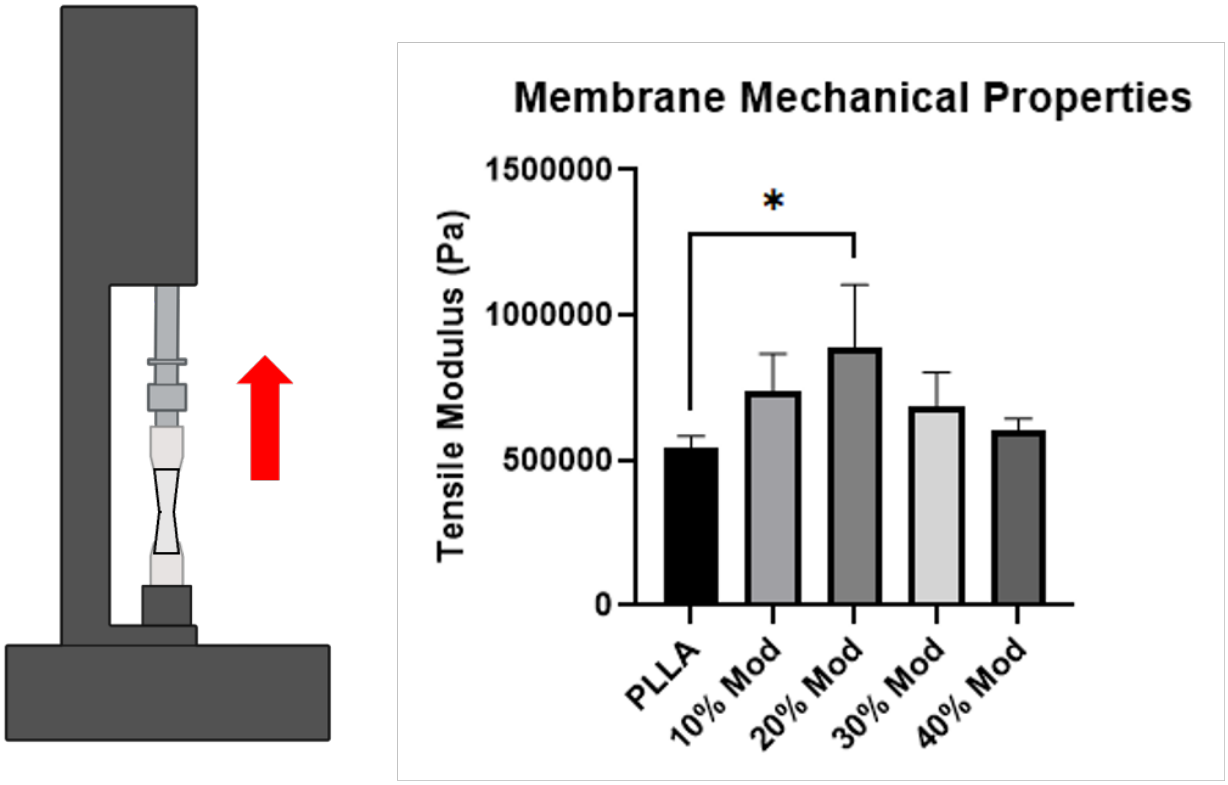

Figure 1.4: Depiction of the thin film tensile testing with a bar graph depicting the measured mean tensile modulus for various TSM biomaterial thin film combinations and error bars of one standard deviation.

The next physical parameter that was investigated in the thin films was their thermosensitive properties, which is an important precursor to shape memory. Dynamic scanning calorimetry (DSC) was performed for three TSM biomaterial combinations in addition to a PLLA thin film and a PCL-DA thin film (**Figure 1.5A**). As predicted, dips in the heat flow were observed for all films with any PCL-DA content between approximately 50 to 60C, but not for the PLLA control, because PCL has a melting point around 60C.[19] An additional dip in the heat flow was observed around 165C to 175C in the thin films containing PLLA, corresponding to the melting point of PLLA.[13,14,15,16] This demonstrates that the polymers are at least partially immiscible, which was desirable so that they each maintain their advantageous physical properties. This helps explain why nanofiber formation with TIPS was observed in lower PCL-DA content films.

The start of the first melting point dip (T_{M1}) was calculated for each thin film from the DSC data because this is where the film begins to achieve a glass-like transition state, as the PCL-DA achieves a liquid-like state but remains stuck and bounded within the PLLA matrix to prevent it from escaping. The T_{M1} was only observed to differ significantly between the PLLA control thin film and the thin films containing any content of PCL-DA, as expected (**Figure 1.5B**). Thus, the TSM biomaterial combinations were confirmed to be thermosensitive at a clinically desirable temperature, lending itself to further investigation. Prior to this investigation, the DSC data for the TSM biomaterial combinations (e.g., 20/80, 40/60, 60/40) was transformed via an inversion and normalization, and the melting point peaks corresponding to PCL-DA and PLLA were integrated to give the enthalpy (H) at each temperature. The ratio of these enthalpies was quantified and plotted as function of thin film percent composition of PLLA (**Figure 1.5C,D**). It was demonstrated that increasing the PCL-DA composition, and subsequently decreasing the PLLA composition, yielded higher enthalpies at the first TSM transition temperature (i.e., PCL-DA T_M) and lower enthalpies at the second TSM transition temperature (i.e., PLLA T_M), and that the ratio between these enthalpies was linearly dependent on the PCL-DA composition of the film. This confirmed that it was the PCL-DA that was imparting relevant thermosensitive properties into the TSM biomaterial and suggested that maximizing the PCL-DA content within the TSM biomaterial would be optimal for TSM.

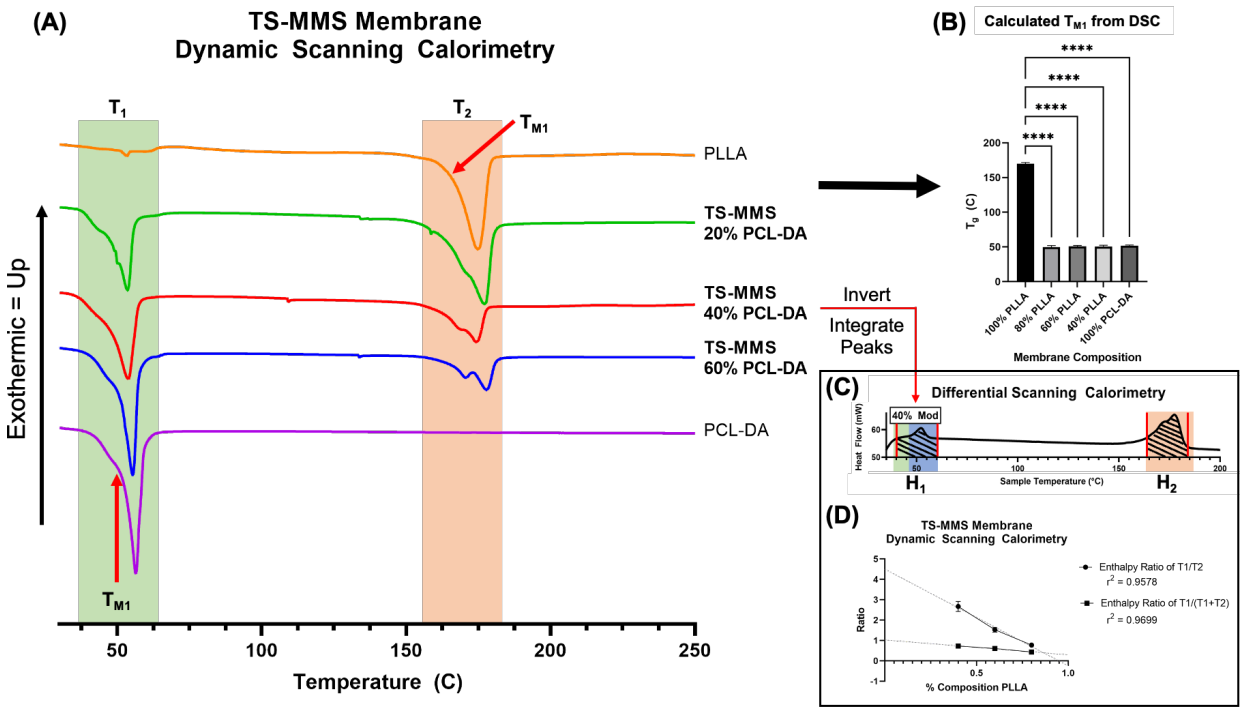

Figure 1.5: Schematic of the characterization of the thermal properties of different biomaterial thin films. (A) Overlaid dynamic scanning calorimetry spectra for different biomaterial thin films with the exothermic direction plotted as up. The two relevant transition temperatures of the film are colored in green and orange corresponding to PCL-DA and PLLA melting points, respectively. (B) Bar graph of the measured mean first melting point (T_{M1}) calculated from the DSC spectra with error bars plotted as the standard deviation and TSM biomaterial comparisons to PLLA. (C) An inverted DSC spectrum for a 40/60 TSM biomaterial thin film with a visual depiction of the regions of integration to calculate enthalpy for a (D) plot of the mean enthalpy ratios between the first TSM biomaterial thin film transition temperature and the second transition temperature as a function of PLLA composition within the film.

After it was demonstrated that the TSM biomaterial had clinically relevant thermosensitive properties, the fabricated thin films from this biomaterial were qualitatively tested for shape memory (**Figure 1.6A**). Different w/w combinations from the PLLA control to 40/60 were tested in addition different PCL-DA molecular weight films at the 40/60 TSM biomaterial combination. The 40/60 combination was chosen as the cutoff for maximal PCL-DA composition as this was the highest PCL-DA combination to exhibit a nanofibrous bottom face from TIPS (**Figure 1.3C**). The films were heated at 80C for approximately 1 minute, which was arbitrarily chosen to be in

large excess of the PCL-DA melting point, and then wrapped around a rod to a coiled shape before being cooled at 0C to instantly lock the deformed shape. The deformed shape was held at room temperature as seen in **Figure 1.6A**. Then, the films were heated at either 50C or 80C to qualitatively observe the TSM whereby the films mostly recovered their memorized, virgin shape from their deformed shape. It is also noteworthy to mention that the PLLA control films were not observed to be more shapeable and flexible at 80C, and more importantly, they were not observed to undergo TSM, as expected because of their lack of a melting point below 165C to 175C.

Videos were captured for every test and the time of recovery movement (i.e., unfolding to memorized shape) was measured for each film at these temperatures using video frame analysis. Because not all of the films recovered a perfectly flat shape and the judgement of shape recovery was subjective, this measurement was thought to reasonably provide a quantitative estimate of the quality of recovery; a longer duration of recovery suggests that more polymeric network rearrangement and relaxation (i.e., shape memory) was occurring, assuming a constant speed for molecular rearrangement at a given temperature and approximately equal deformation shapes for all tested films. The TSM biomaterial films all recovered drastically at 80C and there was no apparent difference in recovery movement duration, likely because the temperature was significantly above the TSM biomaterial films' first transition temperature. However, at 50C the films were observed have recovery movement durations approximately proportional to the amount of PCL-DA composition in the w/w of the film. This result further confirmed the results of **Figure 1.5** demonstrating that maximizing the PCL-DA content subsequently maximized the TSM biomaterial thermosensitive properties for TSM at clinically relevant temperatures, and that TSM would be observable at the T_{M1} point due to PCL-DA achieving a liquid-like state, causing the overall biomaterial film to be rubbery and capable of physical polymeric network rearrangement.

Surprisingly, the PCL-DA molecular weight in the 40/60 TSM biomaterial combination only appeared to have a statistically significant effect for the 2 kDa molecular weight (**Figure 1.6C**). This likely suggests that the increased crosslinking density (theoretically five times greater than the 10 kDa PCL-DA and ten times greater than the 20 kDa PCL-DA) helps to memorize the TSM biomaterial shape more effectively due to a more rigid semi-interpenetrating network, where the minimal material energy for the memorized shape is more constrained in its polymeric arrangement conformations. In other words, a more crosslinked TSM biomaterial can adopt less minimal energy polymeric network conformations during TSM, and thus takes more time to search for a minimal energy network conformation resulting in a recovered shape that more closely resembles the virgin shape and virgin polymeric network conformation.

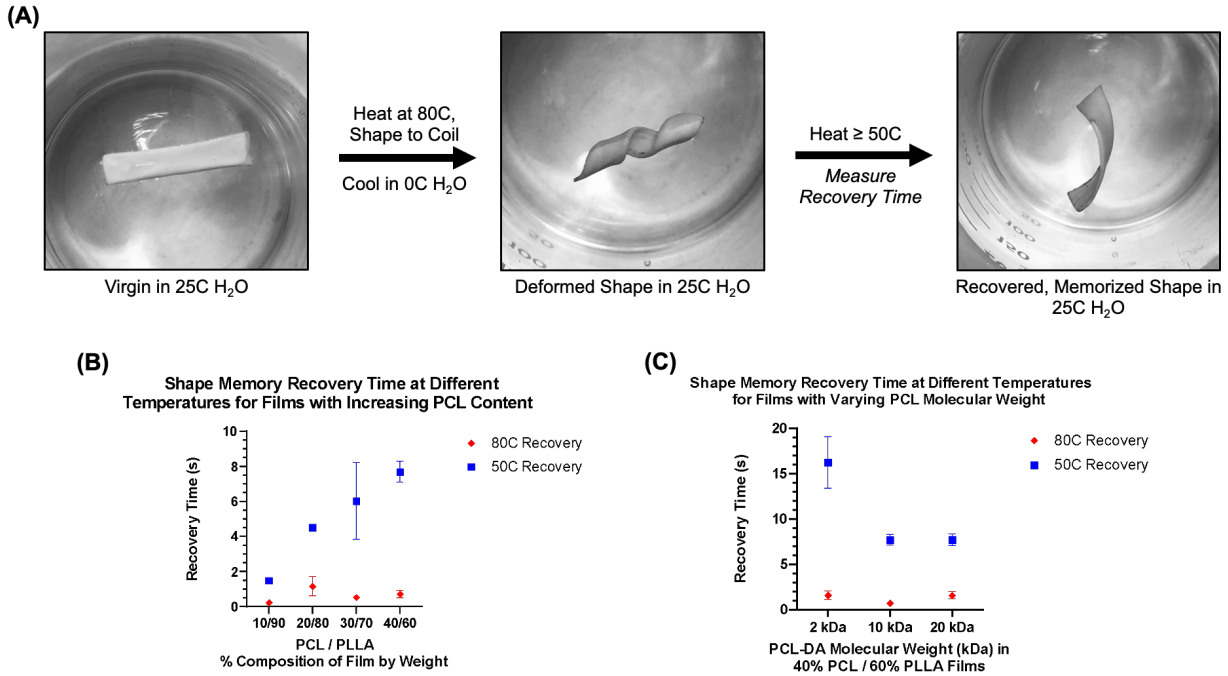

Figure 1.6: Thermal shape memory of TSM biomaterial thin films. (A) Thermal cycling procedure for testing shape memory with images of a TSM biomaterial thin film composed of 40% PCL-DA and 60% PLLA w/w. Each image is taken of the film floating in 25C water. (B) Measured mean shape memory recovery times at 50C and 80C for TSM biomaterial thin films composed of different w/w combinations of PCL-DA and PLLA with error bars depicting the standard deviation. (C) Measured mean shape memory recovery times at 50C and 80C for TSM biomaterial

thin films composed of 40% PCL-DA and 60% PLLA fabricated from different molecular weight PCL-DA with error bars depicting the standard deviation.

Ultimately, the results of the nanofiber optimization steps selected for TSM biomaterial combinations of 10 kDa PCL-DA with w/w ratios of PCL-DA to PLLA from 0/100 to 40/60. From these combinations, the results of the clinically relevant thermosensitive properties and the TSM profiles suggested that maximizing PCL-DA concentration within the w/w ratios would maximize the TSM biomaterial ability for TSM. Thus, it was logically decided to proceed with an optimized combination of 40/60 w/w PCL-DA to PLLA using 10 kDa PCL-DA which yielded desirable nanofiber formation on the bottom thin film face via TIPS and excellent TSM. Thus, all further experiments and investigations were conducted TSM biomaterial films fabricated with these conditions until otherwise stated.

The next relevant question about the TSM biomaterial to investigate was whether the material was fundamentally altered during a thermal cycle for TSM, and if the TSM biomaterial could withstand multiple cycles while maintaining its optimal physical properties. This was a relevant concern since the PCL-DA was theoretically melting at temperatures at 50C, meaning it could possibly escape the thin film polymeric matrix or drastically rearrange within the TSM biomaterial, possibly destroying the nanofibers. First, the tensile modulus was investigated for the optimized TSM biomaterial in thin films as a function of thermal cycling, depicted in **Figure 1.7A**. There was no statistically significant difference in tensile modulus between the virgin TSM biomaterial thin film and a TSM biomaterial thin film cycled one, two, and five times (**Figure 1.7B**). This was a strong preliminary indicator demonstrating that the TSM biomaterial was not being fundamentally altered after at least five cycles, and further suggested that the PCL-DA was staying within the film and not escaping the matrix. Additionally, the fact that these films were able to

undergo continual thermal cycles with TSM supported this claim since PCL-DA is responsible for the thermosensitive behavior and TSM.

Additional films fabricated under the same conditions were deformed without TSM (i.e., shaped to a coil but not reheated to trigger TSM), thermally cycled once, and thermally cycled ten times. SEM of the bottom face of all these films was performed revealing homogenous nanofiber distributions for every group. This was a significant result that further supported the argument that these TSM biomaterial thin films were not significantly altered in any way after continuous thermal cycling, or even during deformation. Thus, the nanofibers are not a recovered structure during TSM, but remain present at every stage, which is highly desirable for clinical implantation scenarios in which the virgin shape does not need to be recovered. This led to a further understanding of the DSC profile in **Figure 1.5A**, which may suggest that the T_{M1} point is more like a glass transition state for the overall TSM biomaterial, since the PCL-DA is stuck within the matrix it likely behaves like a trapped, extremely viscous fluid that acts like a rubber, lending to the favorable clinical handling properties of the TSM biomaterial at elevated temperatures and the TSM effect itself.

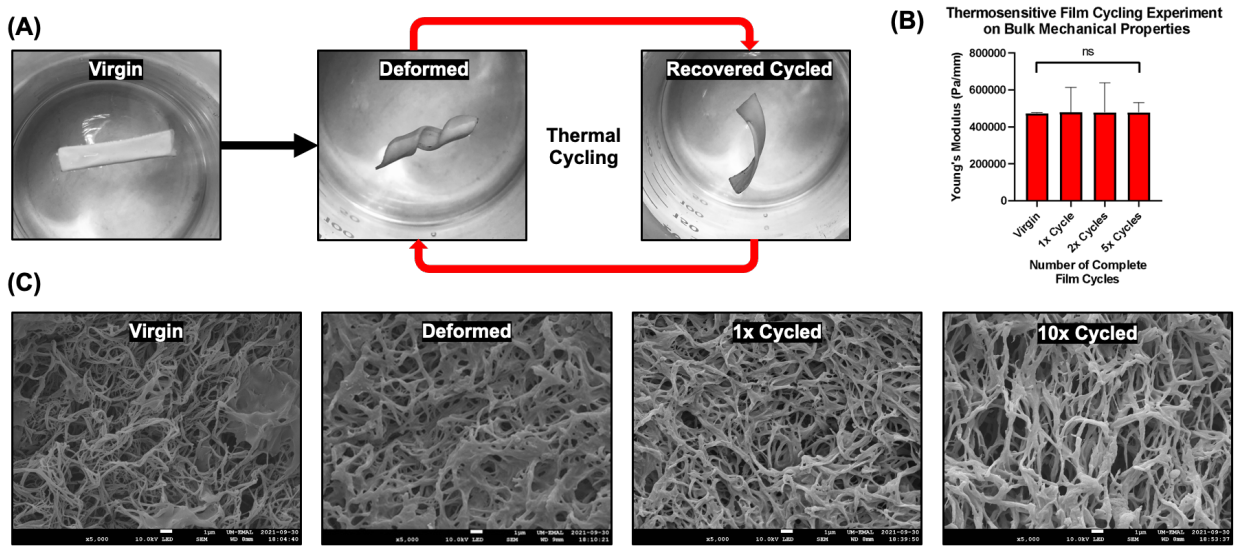

Figure 1.7: (A) Schematic of the thermal cycling for TSM biomaterial thin films with experiment images at each stage of a representative example thermal cycle of a TSM biomaterial thin film composed of 40% PCL-DA and 60% PLLA w/w. Each image is taken of the film floating in 25C water. (B) Bar graph depicting the measured mean tensile moduli for different thermally cycled TSM biomaterial thin films composed of 40% PCL-DA and 60% PLLA w/w. Error bars depict the measured standard deviation in tensile modulus for each group.

1.3.2 Controlled Biphase Formation with Different Surface Morphologies

After confirming that the optimized TSM biomaterial thin films did not alter during thermal cycling, it was still unknown why a bilayer was observed in cross-sections of the TSM biomaterial (**Figure 1.1**). This phenomenon was hypothesized to occur by one or more of three possible mechanisms: (1) altered TIPS at the top thin film surface contacting the air, not properly allowing for adequate PLLA crystallization into nanofibers from the THF solvent, (2) partial macroscopic phase separation between PCL-DA and PLLA during TIPS due to different polymeric miscibility with THF and a less dense PCL-DA network, which is known to be smooth, migrating to the top of the thin film, or (3) partial macroscopic phase separation between PCL-DA and PLLA during PCL-DA photocrosslinking due to a gradient of crosslinking events occurring across the film, maximized at top surface receiving the greatest photon intensity, causing PCL-DA to fall out of

THF as its molecular weight increases with crosslinking events, pulling the polymer toward the surface. Several experiments were conducted to investigate each of these hypotheses, beginning with the second hypothesis.

Nile blue-PLLA and fluorescein isothiocyanate (FITC)-PCL were synthesized by methods according to the literature.[13,14,15,16] A 40/60 TSM biomaterial was to be fabricated from these polymers such that the polymeric distributions of PCL and PLLA could be qualitatively and quantitatively determined by fluorescence because Nile blue and FITC fluoresce at different wavelengths under different excitation wavelengths. Furthermore, the presence of FITC-functional group at the ends of each PCL molecule prevented crosslinking, and thus any significant nonhomogeneous distributions of PCL and PLLA would be attributable to polymeric phase separation during TIPS. Taking cross-sections of thin films synthesized with these polymers, keeping every other step in the TSM biomaterial thin film fabrication constant, including an irradiation step, did indeed result in a nonhomogeneous macroscopic distribution of Nile blue-PLLA and FITC-PCL, although both polymers were still present in the entire film (**Figure 8A,B**). FITC-PCL was observed to be concentrated in a thin band at the top of the film whereas PLLA was observed to be more heavily concentrated toward the bottom of the film. Given that PCL is a smooth biomaterial that cannot spontaneously form nanofibers through TIPS and that PLLA can form nanofibers through TIPS, this polymeric distribution supported the findings in **Figure 1** in that the top face was observed to be smooth, and the bottom face was observed to be nanofibrous. This experiment supported the hypothesis that PCL-DA was partially phase separating from PLLA due to TIPS, causing a PCL-DA concentrated top layer with a smooth surface topology, and a PLLA concentrated bottom layer with a nanofibrous surface topology.

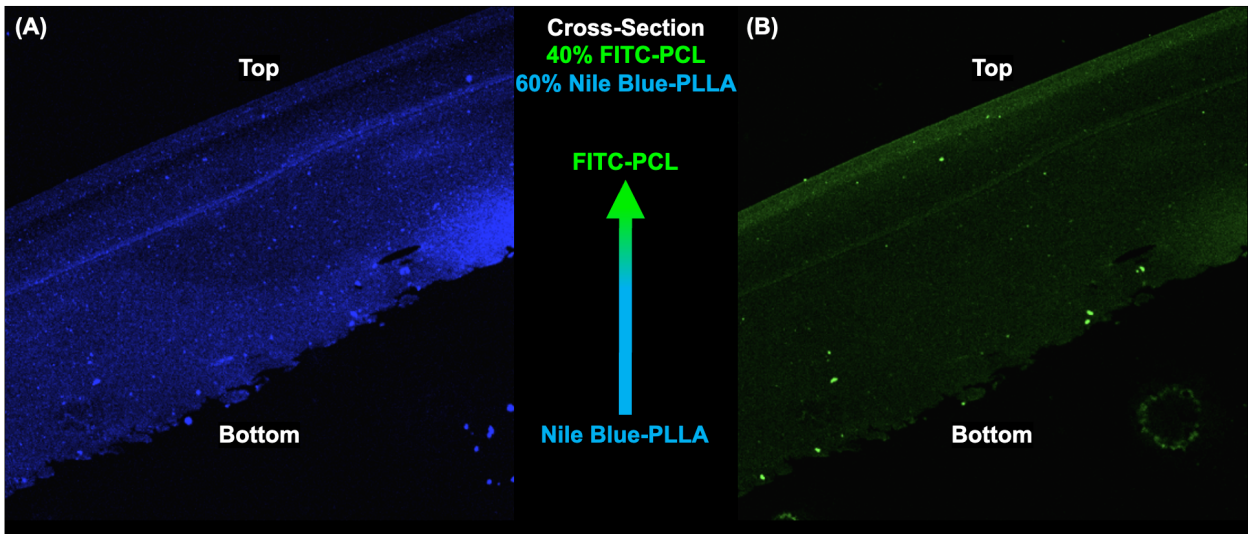

Figure 1.8: Representative confocal microscopy images of the fluorescent polymer experiment showing the spatial distribution of Nile blue-PLLA and FITC-PCL in the perpendicular cross-section of TSM biomaterial thin film after TIPS. The film is composed of 40% FITC-PCL and 60% Nile blue-PLLA w/w. (A) Confocal microscopy image of the fluorescent TSM biomaterial thin film cross-section under a 358 nm excitation laser allowing for the fluorescent visualization of Nile blue-PLLA. (B) Confocal microscopy image of the fluorescent TSM biomaterial thin film cross-section under a 495 nm excitation laser allowing for the fluorescent visualization of FITC-PCL.

The evidence to suggest that the PCL-DA was partially phase separating from PLLA during TIPS did not discredit the other hypotheses for the smooth layer formation, as it was plausible for all the proposed events to contribute to this phenomenon because they can happen independently. Thus, the next hypothesis investigated was the possibility of altered TIPS at the top of the film surface that could interfere with PLLA crystallization into nanofibers. This claim was qualitatively investigated by examining an optimized TSM biomaterial thin film cross-section and comparing it to the top face of a PLLA thin film; the hypothesis was that if the PCL-DA is solely responsible for the smooth layer formation, the PLLA thin film should exhibit a nanofibrous top face because the contact with the air should have no impact on PLLA crystallization into nanofibers.

SEM images of the optimized TSM biomaterial thin film cross-section again revealed a bilayer of a thin, smooth block of polymer at the top face and a nanofibrous bottom layer, which

constituted a majority of the film (**Figure 9**). Let it be noted that the seemingly smooth regions in the bottom layer are likely mostly an artifact of the razor slicing of the film into a cross-section, which probably ripped and flattened out the nanofibrous polymer along the thin slice. This claim is supported by the zoomed in images of these cracks in the nanofibrous bottom region showing uniform nanofibers just beyond the part of thin film that would have come into contact with the razor during a cross-section slice. Toward the top side of the TSM biomaterial film, there is a very distinct boundary between a smooth block of polymer, approximately 100 µm thick, and a nanofibrous region.

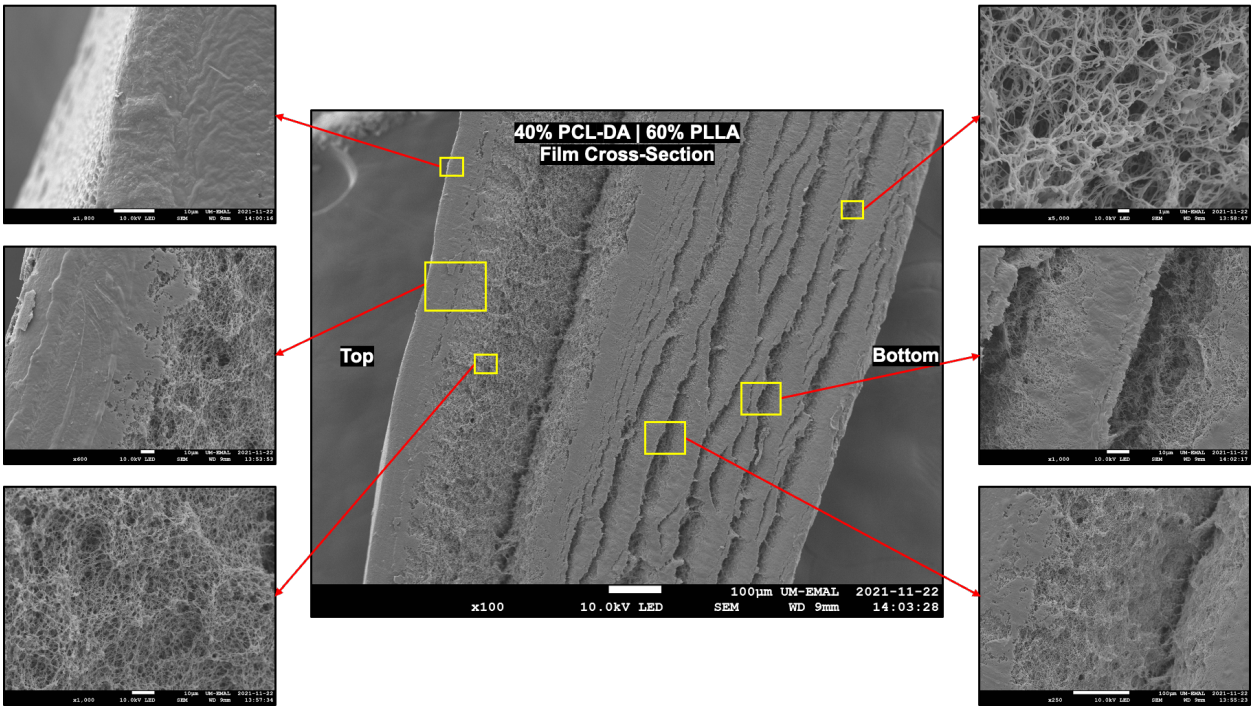

Figure 1.9: Representative scanning electron microscopy images of the biphasic morphology of a TSM biomaterial thin film cross-section composed of 40% PCL-DA and 60% PLLA. The top layer presents a smooth surface topology while the bottom layer presents a nanofibrous surface topology. Yellow boxes represent regions where magnified SEM images were captured.

When investigating the PLLA control film top side, it appeared to have a highly cracked top face where the actual face was smooth, but directly underneath were exposed nanofibers (**Figure 1.10**). A zoomed in image of one of these cracks shows that the smooth boundary is less than 10

μm thick in the PLLA films, which is drastically less than the approximately 100 μm thick smooth region of the TSM biomaterial thin film. Nonetheless, these results suggested that the air contact with the top face does interfere with PLLA crystallization into nanofibers during TIPS directly at surface of the thin film, which is likely due to THF solvent evaporation at the top of the film or an atmospheric miscibility interaction with the PLLA polymer causing it to aggregate and not crystallize. However, this effect is extremely minor as seen by the less than 10 μm smooth layer of the PLLA control film, which was brittle and cracked to expose the nanofibers directly underneath. It accounts for a negligible portion of the TSM biomaterial thin film smooth layer formation, which is much thicker and more distinct than the smooth top surface of a PLLA thin film. Thus, the smooth layer formation in the TSM biomaterial thin film was further confirmed to be a consequence of the PCL-DA incorporation. Thus, the highly distinct bilayer of a nanofibrous bottom layer and smooth top layer was concluded to be a unique, unexpected property of the TSM biomaterial thin films, which cannot be said about the PLLA films.

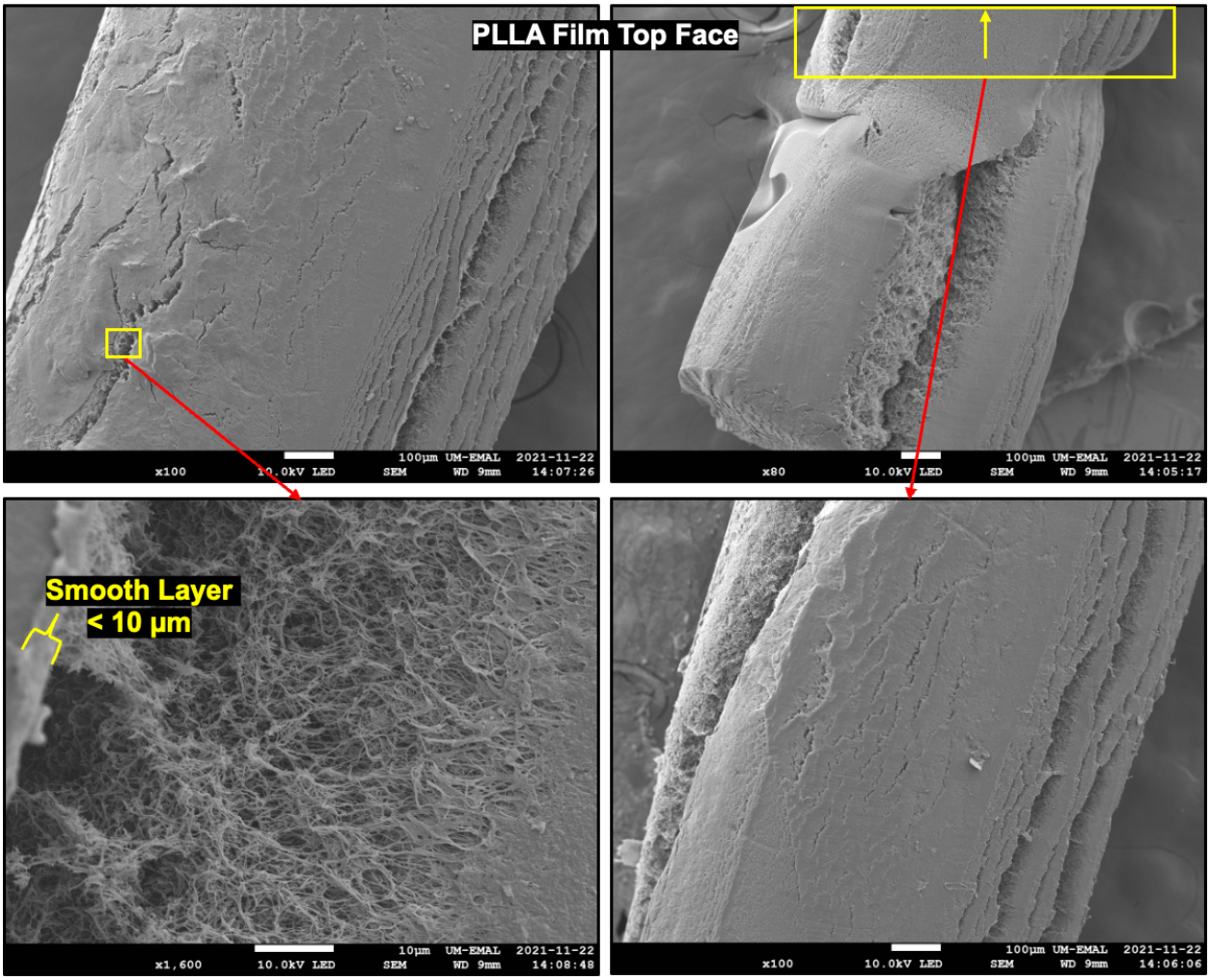

Figure 1.10: Representative scanning electron microscopy images investigating the top face surface topology of a PLLA control thin film. Yellow boxes correspond to regions where higher magnification SEM images were captured. The PLLA control thin film ultimately presents a cracked top face that exposes nanofibers underneath a < 10 µm thick smooth layer.

After determining that the bilayer formation was mostly a consequence of the PCL-DA incorporation, it was desirable to investigate if photocrosslinking also contributed to the mechanism of the bilayer formation, which was hypothesized to be a means of controlling the thickness of the smooth and nanofibrous layers during the TSM biomaterial thin film fabrication. All prior films were irradiated for five minutes during the PCL-DA crosslinking step, which was chosen arbitrarily. This experiment sought to modify the time of irradiation variable to investigate

if the thickness of the smooth layer, relative to the total TSM biomaterial thin film thickness, would be a function of irradiation time. Optimized TSM biomaterial films were made under six irradiation time conditions, where they were cross-sectioned and examined by SEM at the smooth top layer of the cross-section, the approximate separation border between the smooth and nanofibrous layers in the cross-section, and the nanofibrous bottom layer of the cross-section (**Figure 1.11A**).

The results of the thin film cross-sectioned morphology for this experiment qualitatively suggested that increasing the time of irradiation increased the phase separation between PCL-DA and PLLA, or at least increased their abilities to crystallize. This was evident from the nanofibrous layer becoming more distinct and uniformly nanofibrous with an increase in irradiation time, the smooth layer becoming more solidified and smoother as irradiation time increases, and the middle separation barrier between the nanofibrous region and smooth region becoming more distinct at higher irradiation times. This was evidence to confirm the earlier mechanistic hypothesis for phase separation proposing that PCL-DA was partially phase separating from PLLA during PCL-DA photocrosslinking due to a gradient of crosslinking events occurring across the film causing PCL-DA to become immiscible in THF as its molecular weight increased with crosslinking events, pulling the polymer toward the surface where the crosslinking reactions were maximally occurring.

After this qualitative morphology investigation provided support for the hypothesis that the bilayer formation and thickness could be controlled by the irradiation time during the fabrication of the TSM biomaterial thin films, the experiment was repeated using new films of the same optimized TSM biomaterial that were fabricated under seven different irradiation time conditions. They were cross-sectioned and imaged by SEM with low zoom settings to capture the entire width of each cross-section. These images were then processed in ImageJ where the thickness of the smooth layer and the total film thickness were measured at three different points along each sample

image (**Figure 1.11B**). The ratio of the smooth layer thickness to the total film thickness at each point was calculated to be the thickness proportion ratio, and these measurements were plotted as a function of irradiation time (**Figure 1.11C**).

This quantitatively confirmed that the smooth top layer thickness, and consequently the bottom nanofibrous layer thickness, could be controlled by the irradiation time for the TSM biomaterial thin films during their fabrication. Furthermore, this is a consequence of the hypothesized mechanism of the bilayer formation in the TSM biomaterial thin films via PCL-DA crosslinking. It is thought that the crosslinking causes the PCL-DA to partially phase separate from the PLLA as the PCL-DA achieves higher molecular weights with more crosslinking, and begins to crystallize and migrate toward the top of the film; this is likely because that is where the crosslinking is occurring the most or because it becomes immiscible with THF but stays less dense than the dissolved PLLA polymer, resulting in the upward polymeric migration. Regardless, this was a surprising and unintended fabrication property of the TSM biomaterial thin films. It was also interesting to note that the smooth layer thickness proportion increased approximately linearly with irradiation time until a threshold of about 7 minutes, when the thickness proportion stayed roughly the same (**Figure 1.11C**). This is likely because most of the PCL-DA network is crosslinked after about 7 minutes for the 40/60 TSM biomaterial combination, and the PCL-DA therefore receives no further stimuli to assist with phase separation from PLLA and stays locked in its semi-interpenetrating network. It is finally noteworthy to add that the converging thickness proportion approaches 0.4 for the 40/60 TSM biomaterial, which may suggest almost all of the PCL-DA phase separates from the PLLA at high irradiation time points, which may not lead to approximately uniform thermosensitive properties of TSM. Thus, five minutes was maintained as the standard for fabricating TSM biomaterial thin films.

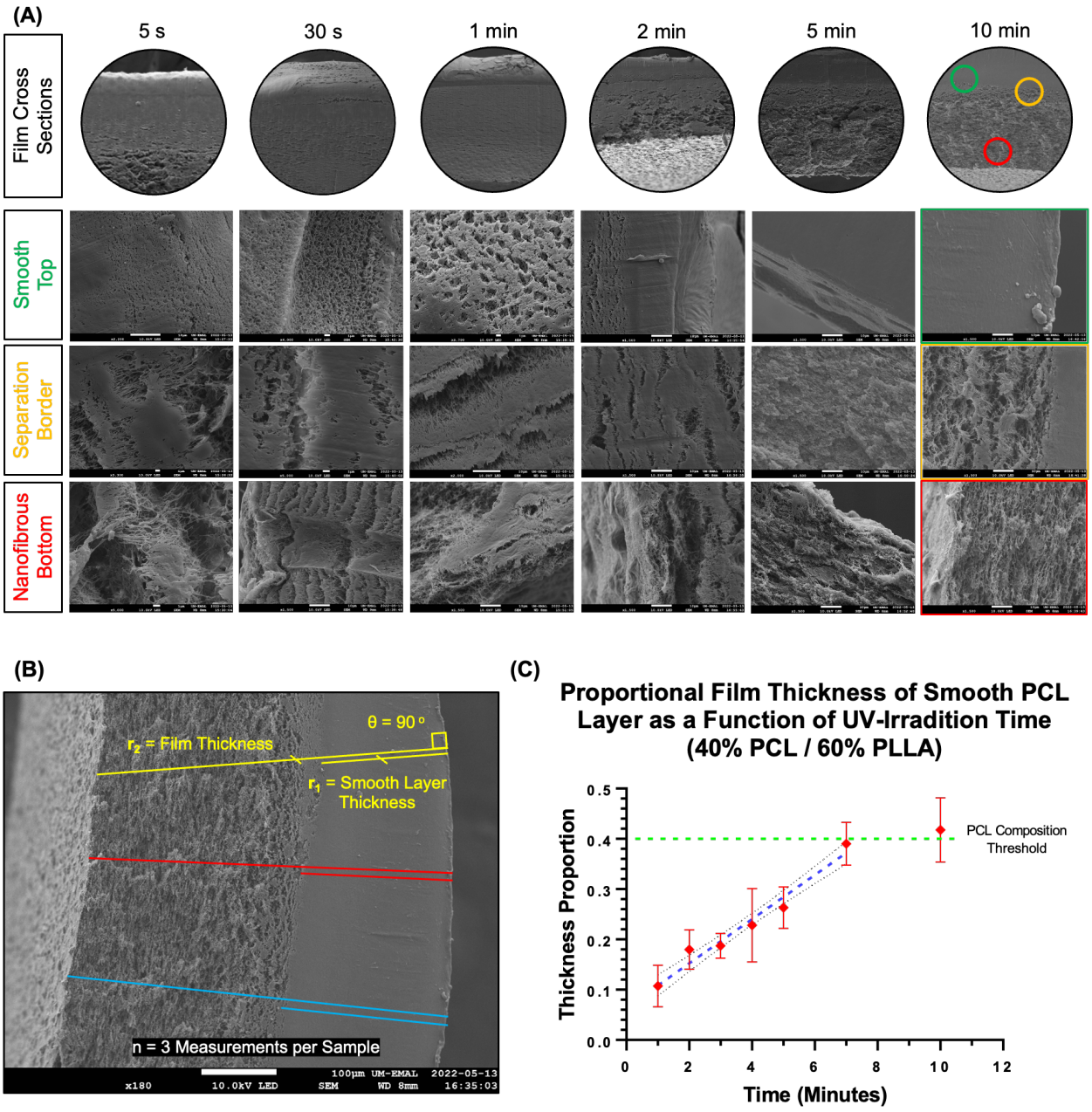

Figure 1.11: Schematic of the experimental investigation of how photocrosslinking PCL-DA within the TSM biomaterial thin film construct influences biphasic morphology formation. (A) Scanning electron microscopy images of different parts of perpendicular cross-sections of TSM biomaterial thin films composed of 40% PCL-DA and 60% PLLA that have been irradiated for different time durations. For each time duration representative SEM images are shown for the overall film cross-section morphology, the smooth top layer of the cross-section, the separation border of the cross-section between the biphasic layers, and the nanofibrous bottom layer of the cross-section, respectively. (B) Scanning electron microscopy image of a cross-section of a TSM biomaterial thin film irradiated for 10 minutes that is composed of 40% PCL-DA and 60% PLLA

with example measurement lines that would have been drawn in ImageJ to measure the smooth layer thickness proportion at three different points in the thin film. Note that the lines of the same color are parallel to each other and perpendicular to the smooth layer edge at the top. (C) Scatter plot of the measured mean smooth layer thickness proportions from ImageJ as a function of irradiation time for TSM biomaterial thin films composed of 40% PCL-DA and 60% PLLA. Error bars depict the measured standard deviation for each group. The dashed blue line was the calculated linear regression with a 95% confidence interval shown as the dashed black lines. The dashed green line represents the PCL-DA composition threshold in the TSM biomaterial thin film (i.e., 40%) representing a theoretical approximation of the upper limit for smooth layer thickness proportion.

1.3.3 Characterized and Modified Hydrolytic Degradation Rates

Ultimately, these sets of experiments concluded that the distribution of PLLA and PCL-DA was not spatially homogenous through the TSM biomaterial thin film. Besides the difference in surface topology between the different faces of the TSM biomaterial thin films, it desirable to investigate what other properties would be affected on different sides of the bilayer since this was a novel biomaterial characteristic. Because the bottom layer was dominated by PLLA and the top layer was dominated by PCL-DA, the different physical properties of each of these individual polymers was examined in the literature to create hypotheses about what might differ across the bilayer of the TSM biomaterial thin film. The molecular structure of PLLA is more hydrophilic than that of PCL-DA, and therefore PLLA hydrolyzes more rapidly than PCL-DA.[19] Thus, it was hypothesized that the TSM biomaterial thin film would exhibit biphasic degradation, whereby the nanofibrous bottom layer dominated by PLLA would hydrolyze and degrade quicker than the smooth top layer dominated by crosslinked PCL-DA.

Thermogravimetric analysis (TGA) was performed on a PLLA control film and an optimized TSM biomaterial film to identify if there were any differences between the degradation profiles of these films and to investigate if the TSM biomaterial thin film exhibited a hypothesized biphasic degradation profile (**Figure 1.12A**). As expected, one film weight derivative peak was observed

in the PLLA film, corresponding to the thermal combustion of PLLA, implying that the PLLA control film degrades at one constant rate. On the contrary, the optimized 40/60 TSM biomaterial thin film exhibited two distinct film weight derivative peaks, one for the thermal combustion of PLLA and one for the thermal combustion of PCL-DA. First, this further confirmed the hypothesis that PCL-DA and PLLA were partially phase separating in the TSM biomaterial thin film, agreeing with the previous experiments, because the TSM biomaterial was not exhibiting a novel, uniform degradation profile, but rather two individual degradation profiles. This also confirms that the TSM biomaterial is a semi-interpenetrating network because the PCL-DA is not chemically crosslinked with PLLA to make an intertwined co-polymer. This would similarly result in a uniform degradation profile because the molecular properties of this resulting polymer would be distinct from PLLA and PCL-DA, and the material would be chemically homogenous.

TGA was useful to confirm that there were two degradation rates present in the TSM biomaterial thin films corresponding to PLLA and PCL-DA, but it does not convey information about if hydrolysis will occur faster in the PLLA bottom region, as hypothesized, or the PCL-DA top region because TGA is based on degradation via thermal combustion. Moreover, it does not provide concrete evidence about how the TSM biomaterial film will morphologically degrade since the films could not be visually examined during or after TGA. Thus, the optimized 40/60 TSM biomaterial thin films were subject to degrade under basic conditions at 37C to accelerate polymeric hydrolysis for qualitatively monitoring the thin films' morphology during degradation (**Figure 1.12B**). After 14 days, it was visually evident that the bottom nanofibrous region had nearly completely degraded away. This was predicted because the nanofibrous bottom region was largely PLLA, which has a faster degradation rate than PCL-DA.

SEM was done of the bottom face of these degraded films to confirm that the leftover TSM biomaterial was indeed the PCL-DA smooth layer, and that the nanofibers had degraded away with the PLLA (**Figure 1.12C**). This was observed as the bottom face had virtually no nanofibers left, which are highly abundant in the bottom face virgin TSM biomaterial films, confirming that it was the PLLA bottom nanofibrous region that had degraded away. Instead, all that was left on the bottom face of the thin film was regions of smooth biomaterial with cracks and micro-tears in addition to an occasional region of leftover, partially-degraded nanofibers. These results confirmed that not only do PCL-DA and PLLA have different hydrolysis profiles in the TSM biomaterial, but that the non-uniform distribution of these polymers due to partial phase separation causes the TSM biomaterial thin film to degrade in two parts: the nanofibrous bottom region characterized by concentrated PLLA degrades almost completely before the smooth top region region characterized by concentrated PCL-DA.

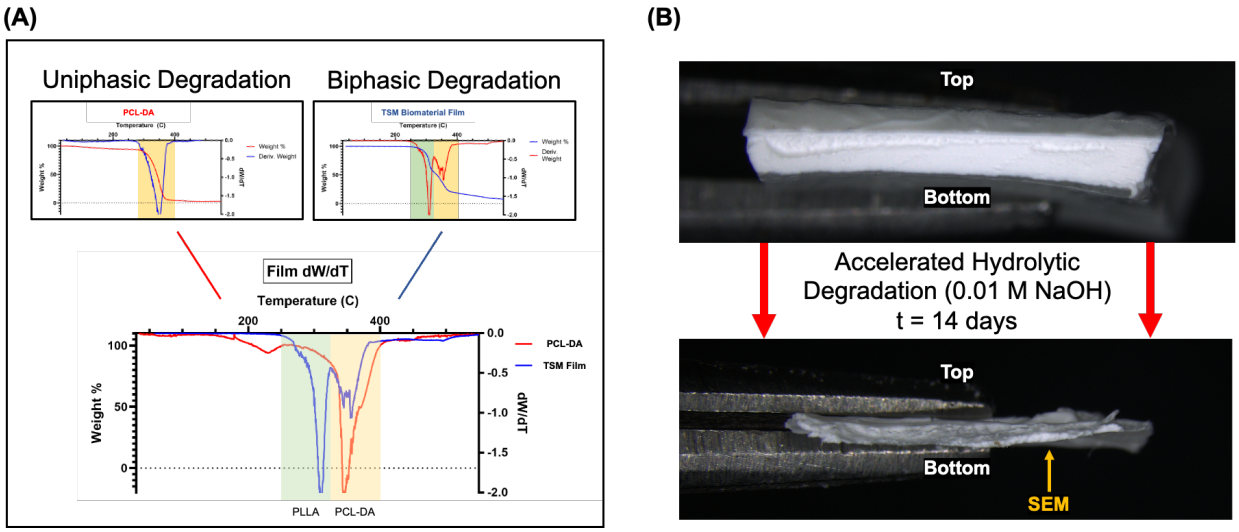

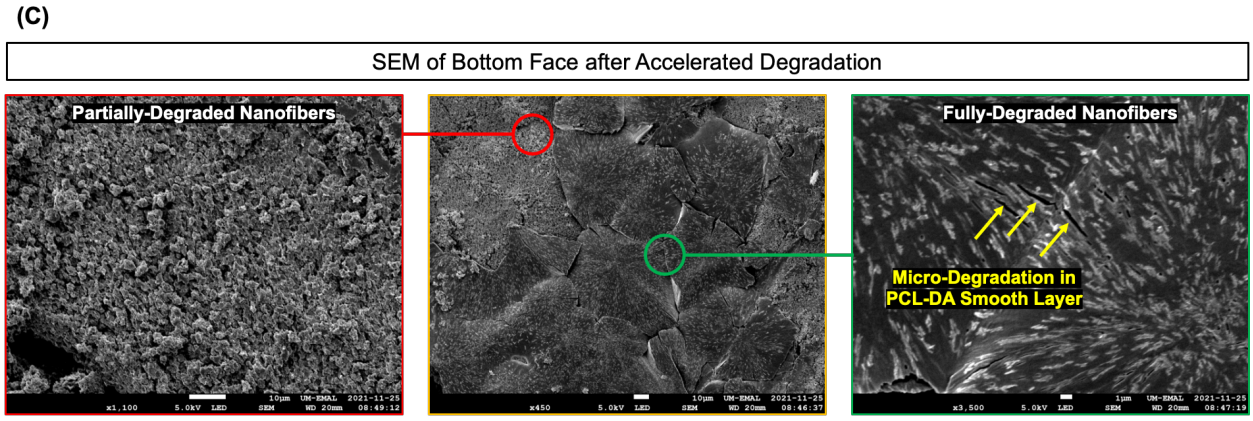

Figure 1.12: Degradation characterization of TSM and PLLA biomaterial thin films. (A) Thermogravimetric analyses (TGA) of PCL-DA bulk polymer, a TSM biomaterial thin film composed of 40% PCL-DA and 60% PLLA, and an overlaid plot of the weight derivatives with respect to temperature (dW/dT) for each of these analyses. The PCL-DA bulk polymer TGA exhibits one dW/dT peak corresponding to the uniphasic combustive degradation of PCL-DA (highlighted with yellow) whereas the TSM biomaterial exhibits two dW/dT peaks corresponding to the combustive degradation of PLLA (highlighted in green) and PCL-DA (highlighted in yellow), respectively. (B) Representative photographs of a TSM biomaterial thin film composed of 40% PCL-DA and 60% PLLA exhibiting biphasic hydrolytic degradation in an accelerated hydrolysis experiment. The bottom nanofibrous layer hydrolyzes before the top smooth layer. (C) Representative scanning electron microscopy photos of the bottom face of the TSM biomaterial thin film photographed in (B) after the accelerated hydrolysis experiment demonstrating significant degradation of the nanofibers.

The difference in the degradation rates between the smooth top layer and the nanofibrous bottom layer of the TSM biomaterial thin film was thought to be partially explained by the relative hydrophobicity of PCL-DA compared to PLLA causing the PCL-DA to hydrolyze slower. This claim sought to be investigated because it was hypothesized that if the relative hydrophilicity of each layer in the TSM biomaterial dictated its rate of hydrolysis, then additional biomaterials or surface coatings with hydrophilic or hydrophobic properties could be added to each layer to speed up or slow down hydrolytic degradation, respectively. This was particularly relevant because PLLA and PCL-DA are both still relatively hydrophobic biomaterials compared to many other existing biomaterials;[19] although their difference in hydrophobicity is great enough to create

biphasic hydrolytic degradation in the TSM biomaterial thin film, both biomaterials still degrade slowly on a biological regeneration time scale. Thus, it was desirable to add a hydrophilic biomaterial to the semi-interpenetrating polymeric network to increase the overall hydrophilicity of the TSM biomaterial thin film with the intention of helping both bilayers degrade more rapidly while still maintaining a bilayer and biphasic degradation.

To this end, poly(lactic-co-glycolic acid) (PLGA) was chosen as a candidate biomaterial to add to the TSM biomaterial since it is partially composed of the same monomer present in PLLA, but is extremely hydrophilic and known for its rapid degradation.[23,24] Thus, it was predicted that this biomaterial may possess an ability to form a nanofibrous or textured surface topology through TIPS, and thus would not necessarily compromise the nanofibrous surface topology in the bottom layer. To ensure that the PLGA would not drastically phase separate from PCL-DA into the bottom layer of the TSM biomaterial thin film due to the vast difference in hydrophilicity between PCL-DA and PLGA, PLGA was end-functionalized with acrylate groups to yield poly(*D,*L-lactide-co-glycolide)-diacrylate (PLGA-DA) so that it could chemically crosslink with PCL-DA via the same photochemical reaction.

TSM biomaterial thin films were fabricated that composed of three different combinations of the w/w/w ratio of PLGA-DA, PCL-DA, and PLLA, respectively. The relative hydrophilicity of each surface on the TSM biomaterial and PLLA control thin films was determined by the contact angle between a water droplet and the respective surface of the film being investigated (**Figure 1.13A**). Surfaces that are more hydrophilic are known to have a smaller contact angle with water droplets because it is thermodynamically favorable for the water to adhere to the hydrophilic surface and spread the droplet out over a larger surface area rather than to oppose the surface in favor of cohesion where the droplet gains height and battles the force of gravity. It was observed

that the top smooth side of every thin film, including the PLLA control film, was more hydrophobic than the bottom nanofibrous side of the thin films. This is justified in the TSM biomaterial thin films because the top smooth layer is dominated by PCL-DA, which is known to be highly hydrophobic.

However, the fact that the PLLA top side and 40/0/60 top side, which is likely dominated by PLGA-DA, were more hydrophobic than the bottom sides was initially surprising. This result can be explained by the fact that the hydrophilicity of a surface is not just dictated by the chemical properties of the surface, but also by the surface topology. Although the PLLA control film is chemically homogenous, the smooth surface that forms at the top of the film due to the air contact inhibiting proper nanofiber formation via TIPS differs from the nanofibrous bottom surface topology; the nanofibrous surface topology has a greater surface area, which allows the water droplet to spread out more easily, decreasing the contact angle and increasing the hydrophilicity relatively to the top surface. On the contrary, the 40/0/60 film is not chemically homogenous as it probably has a gradient of PLGA-DA distribution that is maximized in the top layer due to the partial phase separation occurring from crosslinking as observed with PCL-DA, which would be expected to make the top layer a more hydrophilic surface than the PLLA dominated bottom layer since PLGA-DA is much more hydrophilic than PLLA. However, the top surface morphology of the 40/0/60 TSM biomaterial thin film in **Figure 1.14** reveals that it is relatively smooth, and therefore the nanofibrous surface topology of the bottom layer similarly explains why a lower contact angle was measured and that the bottom layer of the 40/0/60 is more hydrophilic. Nonetheless, the goal of making the TSM biomaterial more hydrophilic by incorporating PLGA-DA was concluded to be successful as increasing the PLGA-DA content yielded relatively more

hydrophilic top and bottom surfaces compared to the other film top and bottom surfaces, respectively (**Figure 1.13C**).

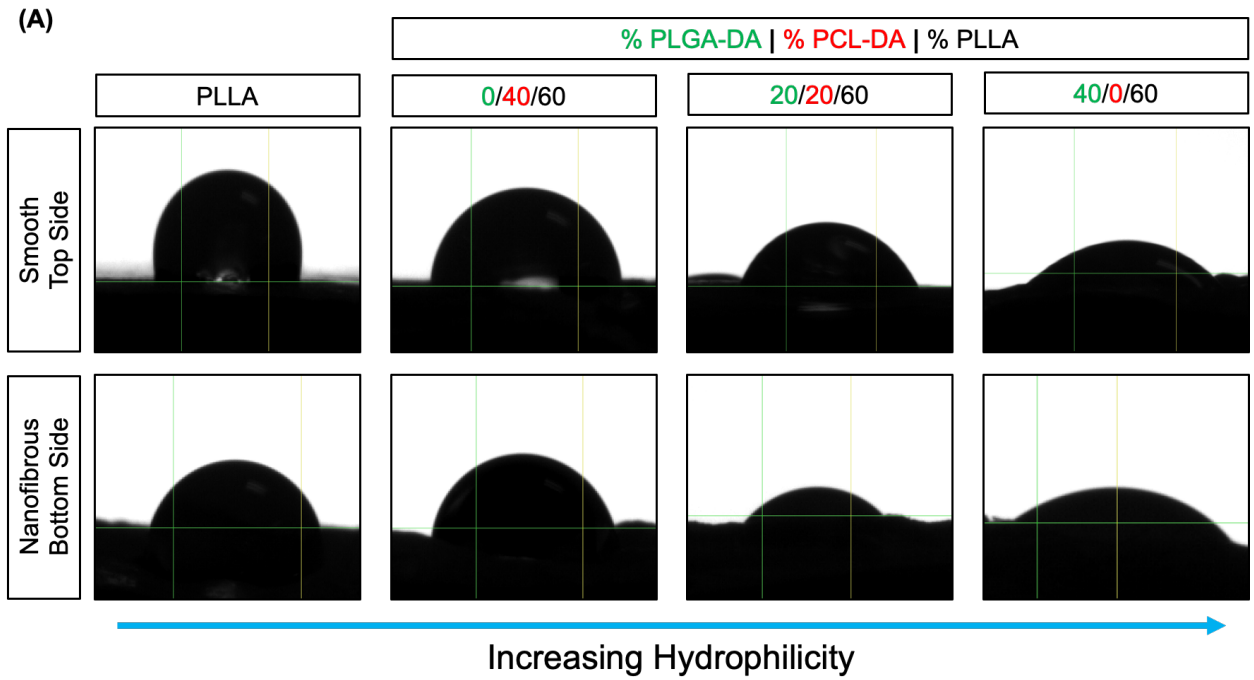

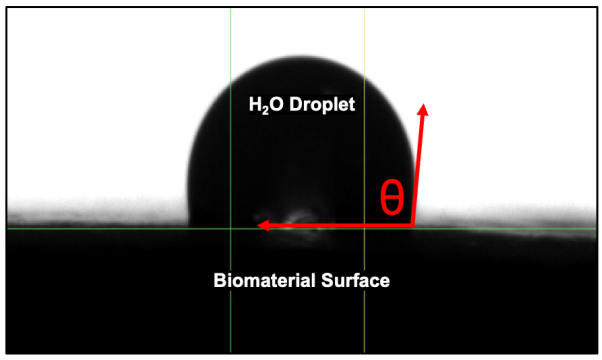

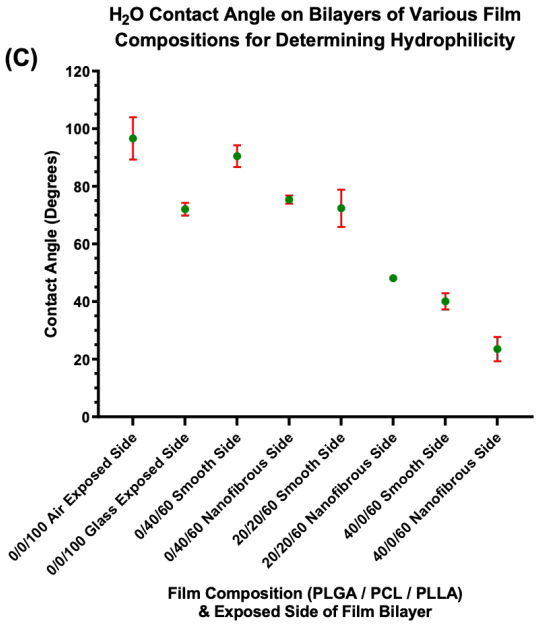

Figure 1.13: Schematic of the contact angle experiment for the surfaces of different TSM biomaterial thin films composed of different combinations of PLGA-DA, PCL-DA, and PLLA w/w/w to approximate hydrophilicity. (A) Representative photographs of water droplets on the top

and bottom surfaces, respectively, for different thin films increasing in hydrophilicity from left to right (i.e., more PLGA incorporation). (B) Example water contact angle on the top surface of a PLLA thin film that would be measured with image analysis. (C) Plot of the measured mean contact angles for the top and bottom surfaces, respectively, for different biomaterial thin films. Error bars depict the measured standard deviation for each group.

After confirming that incorporating PLGA-DA increased the hydrophilicity of the TSM biomaterial thin films, it was important to examine the morphology of the films containing PLGA-DA to investigate if incorporating PLGA-DA into the TSM biomaterial thin films altered the bilayer or top and bottom surface topologies. First, the top and bottom faces of the TSM biomaterial films incorporating PLGA-DA (i.e., 20/20/60 and 40/0/60) were examined by SEM (**Figure 1.14A,B**). Homogenous nanofibers were observed on the bottom face of both TSM biomaterial thin film combinations incorporating PLGA-DA, and mostly smooth surface topologies were observed on the top faces of both combinations. It is noteworthy that the 40/0/60 TSM biomaterial thin film did exhibit small regions of microporosity in the top face, but the overall surface was still relatively smooth. This matches the respective surface topologies observed in the optimized 40/60 TSM biomaterial thin films, suggesting that incorporating PLGA-DA did not significantly alter the surface topology formation, and that it behaves like PCL-DA with respect to phase separation.

Cross-sections of the two TSM biomaterial thin film combinations containing PLGA-DA were then examined by SEM to further ensure that there was a distinct bilayer forming (**Figure 1.14B**). For both combinations, a thick layer of nanofibers was observed on the bottom part of the cross-section. The smooth regions observed in the bottom layer of the cross-section are likely an artifact of damage done by the razor blade during the cross-section slicing, as was observed with the TSM biomaterial thin film cross-section in **Figure 1.9A**. Nonetheless, the bottom layer of the cross-sections for the TSM biomaterial thin films containing PLGA-DA were almost identical to the

cross-section of the bottom layer in the 40/60 TSM biomaterial thin film in **Figure 1.9A**. Similarly, a relatively smooth top layer was also observed in the cross-section of the 20/20/60 TSM biomaterial thin film. However, it was evident that the crosslinked PLGA-DA did impart a small degree of surface texture into this top layer as the outline of dull, poorly separated fibers was observed in magnified SEM images of the top layer of cross-sections, especially in the 40/0/60 TSM biomaterial thin film where the fibers were more distinct.

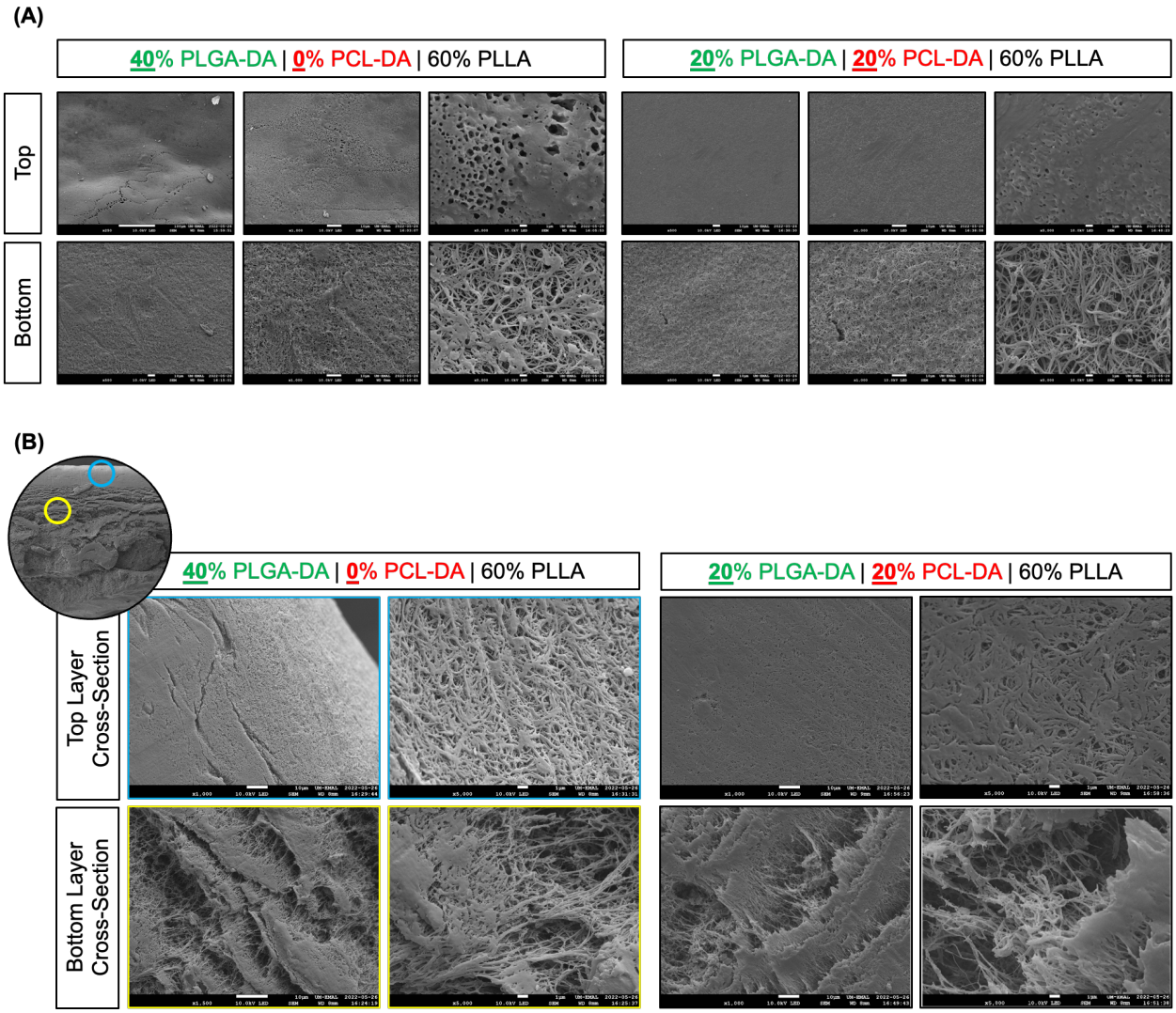

Figure 1.14: Investigation of TSM biomaterial thin film morphology and surface topology with added PLGA-DA incorporation. (A) Representative scanning electron microscopy images of the top and bottom faces, respectively, for two TSM biomaterial thin film combinations composed of PLGA-DA, PCL-DA, and PLLA. (B) Representative scanning electron microscopy images of the

top and bottom layers of perpendicular cross-sections for two TSM biomaterial thin film combinations composed of PLGA-DA, PCL-DA, and PLLA.

The observation that nanofibers induced by TIPS were present in the TSM biomaterial films up to the 40/60 combination and that nanofibers induced by TIPS were present in both combinations of the TSM biomaterial films incorporating PLGA-DA was novel. X-ray diffraction (XRD) was performed on several TSM biomaterial thin film combinations and the raw PCL-DA, PLGA-DA, and PLLA biomaterials to confirm with high confidence if the biomaterials were partially phase separating within the overall TSM biomaterial (**Figure 1.15**). The raw PLLA and PCL-DA polymers were measured to diffract x-rays at separate, distinct angles that were moderately broad, suggesting that the polymers were both somewhere between amorphous and crystalline materials. PLGA-DA was measured to diffract x-rays over a broad range of angles, spanning the range of angles that PLLA and PCL-DA diffract x-rays at, with a poorly defined peak, suggesting that it is between and amorphous and non-crystalline material.

Quantitative XRD of different combinations of the TSM biomaterial thin films showed x-ray diffraction at nearly the identical angles of the PLLA and PCL-DA isolated polymers, with relative intensities of diffraction at these angles corresponding to the amount of the specific polymer in the TSM biomaterial thin film (e.g., the 0/20/80 TSM biomaterial thin film exhibiting higher diffraction intensities at the PLLA diffraction angles than the 0/60/40 film). This experiment further confirmed that PLLA and PCL-DA were partially phase separating and crystallizing into the same amorphous biomaterials as their raw polymers, which for PLLA is a nanofibrous biomaterial and for PCL-DA is a smooth biomaterial. It quantitatively proved that the TSM biomaterial film nanofibers were induced by TIPS, and that incorporating PLGA-DA has no effect on the PLLA amorphous crystallinity contributing to nanofibrosity. However, it should be mentioned that there was relatively little x-ray diffraction at the angles corresponding to PCL-DA

in the 20/20/60 TSM biomaterial thin film, which can be explained by the PCL-DA crosslinking with PLGA-DA to create a new co-polymer with different chemical and physical properties that would not be expected to diffract x-rays the same as PCL-DA.

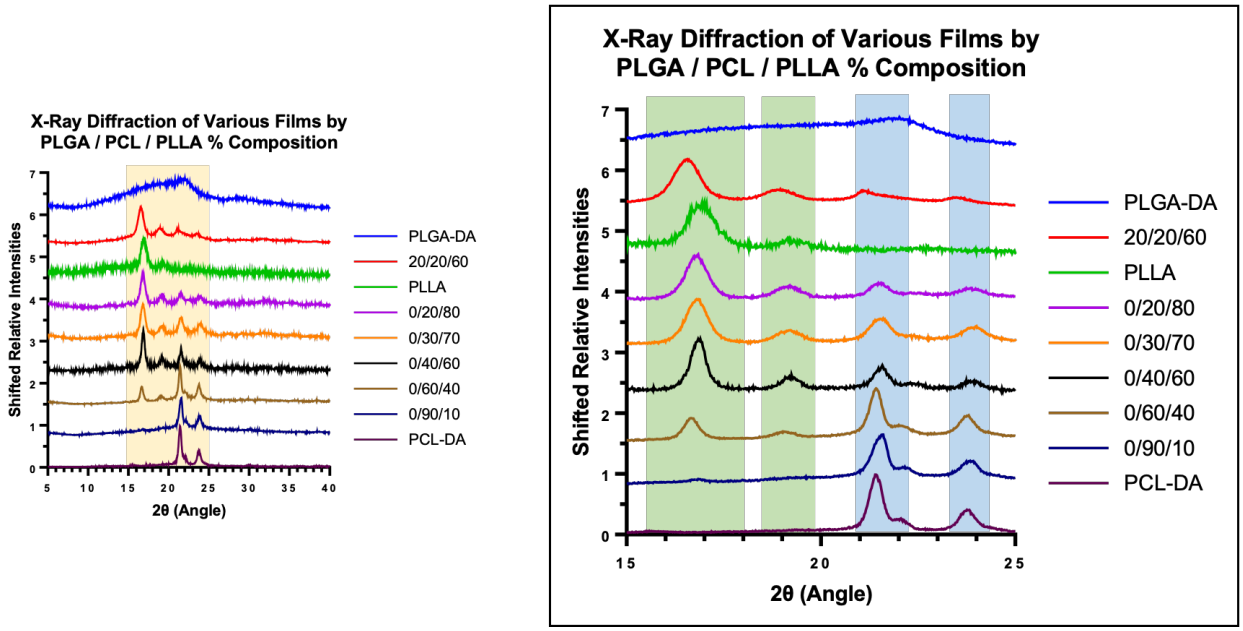

Figure 1.15: Overlaid x-ray diffraction (XRD) spectra for different bulk polymer biomaterials and different TSM biomaterial thin film composition of PLGA-DA, PCL-DA, and PLLA w/w/w. The yellow highlighted rectangle on the left plot represents the region of magnification shown on the right plot. The green rectangles on the right highlight the 2θ ranges where the XRD spectra peaks corresponding to the PLLA bulk polymer occur and the blue rectangles highlight the 2θ ranges where the XRD spectra peaks corresponding to the PCL-DA bulk polymer occur.

It became relevant to consider how incorporating PLGA-DA into the TSM biomaterial thin films would affect the clinically-relevant thermosensitive properties and TSM of the biomaterial, since PLGA is known to have a glass transition temperature between 30-60C and a melting point between 240-280C. Furthermore, it was unknown what thermosensitive properties would arise from the new co-polymer formed by crosslinking PLGA-DA with PCL-DA. Mechanical testing of the PLLA control film, 40/60 TSM biomaterial thin film, and the 20/20/60 TSM biomaterial thin film revealed that both the TSM biomaterial thin films had a statistically significant decrease

in tensile modulus when stretched at 25C and at 80C (**Figure 1.16**). The decrease in the tensile modulus at 80C was expected in the 40/60 TSM biomaterial thin film because the DSC profile in **Figure 1.5** revealed that the film had a T_{M1} around 50C corresponding to the PCL-DA, which would cause the film to achieve a more rubbery state with a lower elastic modulus for easier stretching and shaping. Thus, the observation that the 20/20/60 TSM biomaterial thin film also had a thermosensitive decrease in tensile modulus at 80C suggests a similar mechanism was occurring. However, it should be noted that the 20/20/60 TSM biomaterial had a significantly lower tensile modulus at room temperature than the PLLA or 40/60 thin films, which is likely due to the fact that PLGA is a relatively weak and brittle biomaterial.[23]

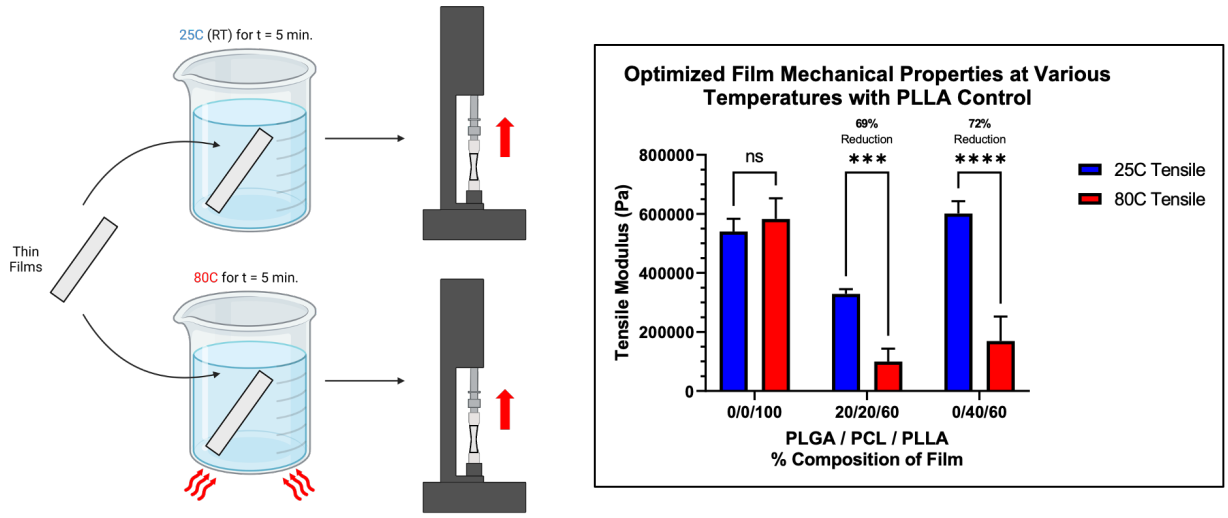

Figure 1.16: Depiction of the thin film tensile testing procedure at different temperatures with a bar graph displaying the measured mean tensile modulus for various TSM biomaterial thin film combinations utilizing PLGA-DA, PCL-DA, and PLLA. Error bars represent one standard deviation.

DSC was additionally performed for the 20/20/60 TSM biomaterial thin films to confirm their clinically relevant thermosensitive properties (**Figure 1.17A**). The DSC spectrum of the 20/20/60 TSM biomaterial film was nearly identical to that of the 40/60 TSM biomaterial thin film, indicating that the incorporation of PLGA-DA was not significantly changing the desirable thermal

properties or the T_{M1} of the 20/20/60 TSM biomaterial thin films. Thus, it was viable to test the thermal cycling and TSM of the 20/20/60 TSM biomaterial thin films because they had a crosslinked, memorized shape and the same T_{M1} as the 40/60 TSM biomaterial thin films, which were proven to possess TSM properties. The 20/20/60 TSM biomaterial thin films were indeed qualitatively observed to demonstrate TSM within a thermal cycle and they were easily shapeable upon heating past the T_{M1} of PCL-DA above 50C (**Figure 1.17B**). Measuring the shape memory recovery times for different TSM biomaterial thin films composed of different amounts of PLGA-DA and PCL-DA revealed that the shape memory recovery times increased with the amount of PCL-DA in the thin film at 50C (**Figure 1.17C**). This was an indicator that more thermal shape memory recovery was occurring due to the increased incorporation of PCL-DA, which is the thermosensitive shape memory component in the thin films.

It is important to note that no TSM recovery was observed in the 40/0/60 TSM biomaterial thin film at 50C because there was no thermosensitive PCL-DA component to achieve a low T_{M1}. However, the 40/0/60 TSM biomaterial thin film was observed to slightly participate in TSM recovery at 80C because the monomer glycolide in PLGA-DA has a melting point around 80C, and the PLGA-DA was crosslinked to help memorize the TSM biomaterial thin film shape. Ultimately, these results demonstrated that PCL-DA is still the thermosensitive component in 20/20/60 TSM biomaterial thin films and that TSM biomaterial thin films simultaneously maximizing hydrophilicity and shape memory properties must strike a balance between PCL-DA and PLGA-DA incorporation, given that PLLA is held constant at its minimum incorporation necessary to achieve nanofibers (i.e., 60% of the TSM biomaterial thin film mass composition).

(A)

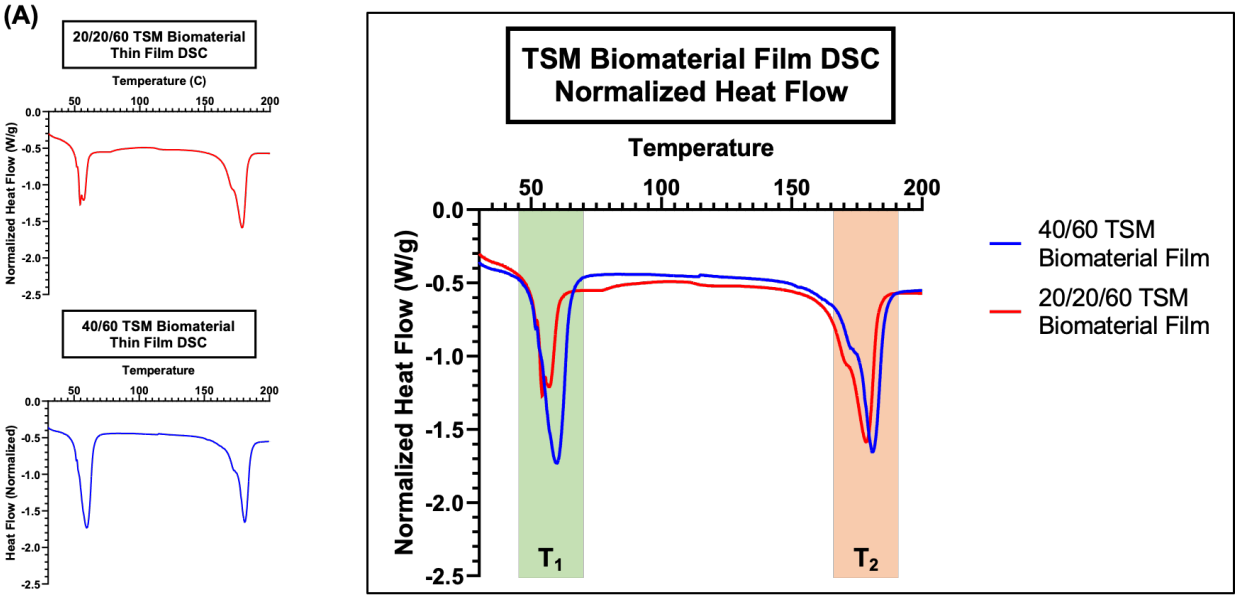
20/20/60 TSM Biomaterial Thin Film DSC
Temperature (C)
Normalized Heat Flow (W/g)
40/60 TSM Biomaterial Thin Film DSC
Temperature
Heat Flow (Normalized)
TSM Biomaterial Film DSC Normalized Heat Flow
Temperature
Normalized Heat Flow (W/g)
T1
T2
40/60 TSM Biomaterial Film
20/20/60 TSM Biomaterial Film

(B)

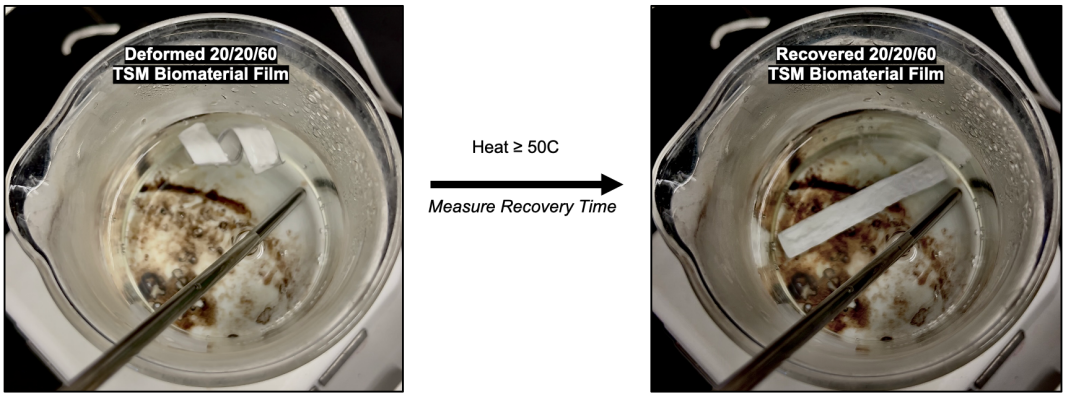
Deformed 20/20/60 TSM Biomaterial Film
Heat ≥ 50C
Measure Recovery Time
Recovered 20/20/60 TSM Biomaterial Film

(C)

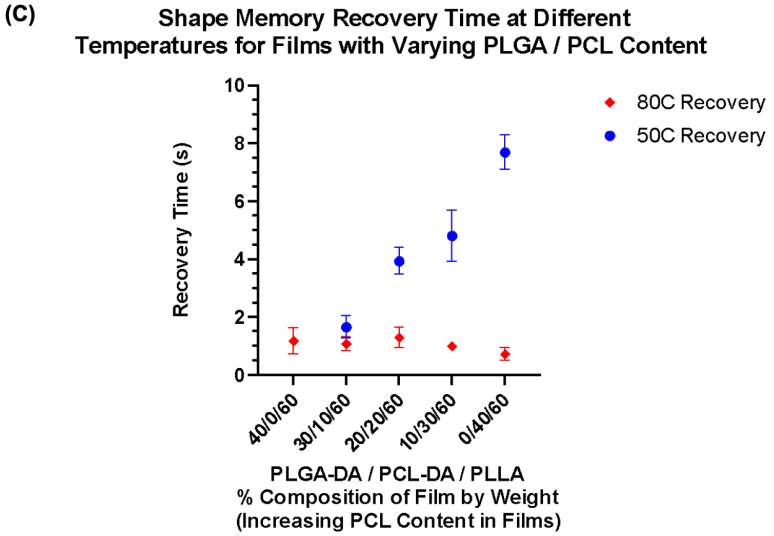
Shape Memory Recovery Time at Different Temperatures for Films with Varying PLGA / PCL Content
Recovery Time (s)
80C Recovery
50C Recovery
40/0/60
30/10/60
20/20/60
10/30/60
0/40/60
PLGA-DA / PCL-DA / PLLA
% Composition of Film by Weight
(Increasing PCL Content in Films)

Figure 1.17: Schematic of the experiments demonstrating the thermal properties and thermosensitive shape memory of TSM biomaterial thin films utilizing PLGA-DA, PCL-DA, and PLLA. (A) Dynamic scanning calorimetry spectra for TSM biomaterial thin films composed of either 40% PCL-DA and 60% PLLA (40/60) or 20% PLGA-DA, 20% PCL-DA, and 60% PLLA (20/20/60). The right-hand DSC spectrum is the overlaid plot of the two TSM biomaterial thin film compositions with the colored rectangles highlighting the melting point of PCL-DA (green) and PLLA (orange), respectively. Both TSM biomaterial thin films exhibit thermosensitivity at a clinically relevant temperature. Note that exothermic is designated as the upward direction in these spectra. (B) Representative images of a thermal cycle for the TSM biomaterial thin film composed of 20% PLGA-DA, 20% PCL-DA, and 60% PLLA. The film exhibits thermosensitive shape memory and thermosensitive clinical shaping properties for deformation to a coiled structure. (C) Plot of measured mean shape memory recovery times at 50C and 80C for different compositions of TSM biomaterial thin films by PLGA-DA, PCL-DA, and PLLA w/w/w. Note that the 40/0/60 is not thermosensitive at 50C because it lacks a PCL-DA component, but is slightly thermosensitive at 80C because glycolide has a melting point around that temperature.

The 20/20/60 TSM biomaterial thin film simultaneously optimizes the PLGA-DA incorporation for maximizing hydrophilicity and PCL-DA incorporation for maximizing TSM and the thermosensitive rubbery state for better clinical shaping. This presented a possible improvement to the TSM biomaterial thin film depending upon its application. However, there was curiosity as to whether the presence of the PLGA-DA in the PCL-DA crosslinked network would destroy the biphasic hydrolytic degradation rate of the thin film. To this end, TGA was performed for the 20/20/60 TSM biomaterial thin film for comparison to the PLLA thin film and the 40/60 TSM biomaterial thin film with known biphasic hydrolytic degradation (**Figure 1.18A**). An overlaid plot of the weight derivatives with respect to temperature for these thin films revealed nearly identical TGA spectra for the 20/20/60 TSM biomaterial thin film and the 40/60 TSM biomaterial thin film (**Figure 1.18B**). More importantly, the 20/20/60 TSM biomaterial thin film TGA dW/dT spectrum revealed two distinct extrema points, like the 40/60 TSM biomaterial thin film TGA dW/dT spectrum, corresponding to the separate thermal combustion temperatures of PLLA and the crosslinked network of PCL-DA and PLGA-DA. This biphasic thermal combustion

degradation suggests different reactivities of the PLLA and the crosslinked network of PLGA-DA and PCL-DA, which implies that these reactivities would also differ with respect to hydrolysis. Therefore, this TGA experiment confirmed the biphasic degradation profile of the 20/20/60 TSM biomaterial thin film. The cumulative results of the experiments with the TSM biomaterial thin films incorporating PLGA-DA ultimately demonstrate that the phase separation, biphasic morphology, and biphasic hydrolytic degradation behavior of the 40/60 TSM biomaterial thin film are not significantly altered by the incorporation of PLGA-DA. Instead, the supplementing the TSM biomaterial thin films with PLGA-DA increases the hydrophilicity and therefore the overall hydrolytic degradation rates of the TSM biomaterial thin film, while maintaining the other properties.

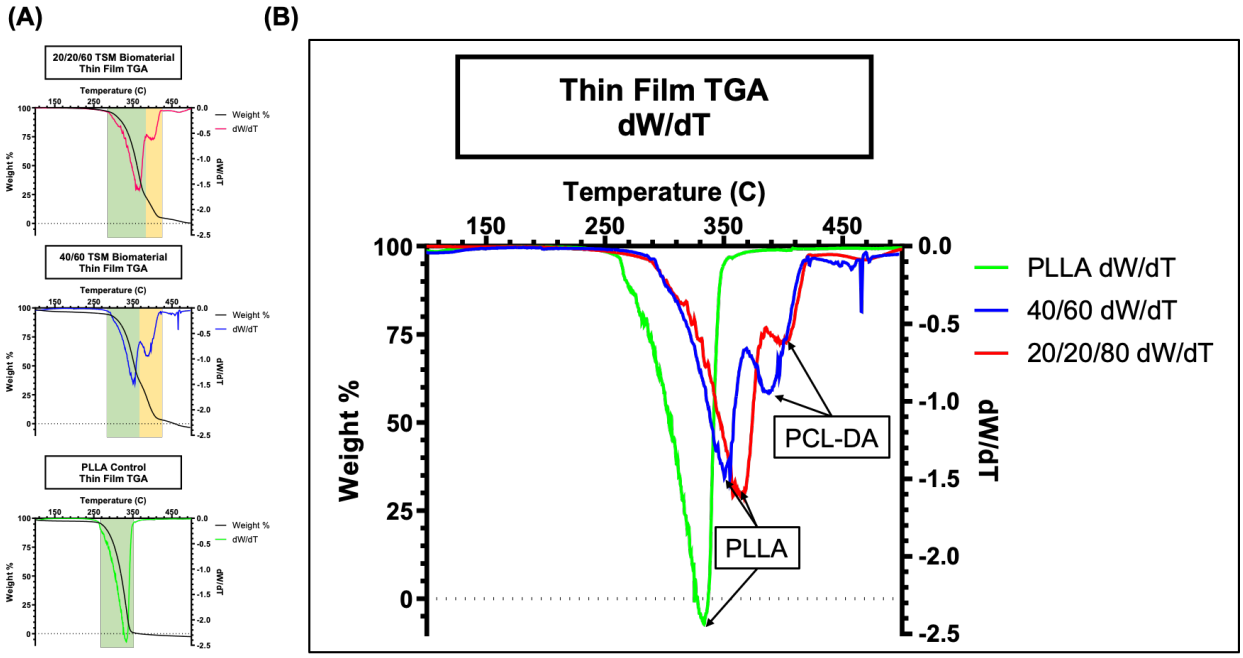

Figure 1.18: Experimental confirmation of biphasic degradation properties in TSM biomaterial thin films containing PLGA-DA, PCL-DA, and PLLA. (A) Thermogravimetric analyses (TGA) of a TSM biomaterial thin film composed of 20% PLGA-DA, 20% PCL-DA, and 60% PLLA (20/20/60), a TSM biomaterial thin composed of 40% PCL-DA and 60% PLLA (40/60), and a PLLA control thin film, respectively. Green highlighted regions correspond to the combustion degradation of PLLA and yellow highlighted regions correspond to the combustion degradation of PCL-DA. (B) Overlaid TGA spectra of the film weight derivatives with respect to temperature

(dW/dT) for the analyzed thin films with labeled peaks corresponding to PLLA and PCL-DA combustion degradation.

1.3.4 Biological Consequence of the Biphasic Biomaterial Thin Film Construct

The biological significance of the biphasic morphology resulting from the TSM biomaterial phase separation sought to be investigated to inspire potential applications of the TSM biomaterial thin film. PLLA is a commonly studied biomaterial for skeletal tissue regeneration because of its similar mechanical properties to trabecular bone; therefore, it was hypothesized that the TSM biomaterial thin films would be conducive to skeletal stem cell proliferation and adhesion. Bone marrow-derived stem cells (BMSCs) were isolated from the long bones of mice and cultured on the TSM biomaterial or PLLA thin films for two, four, six, or eight days. SEM analysis of the top and bottom faces for the PLLA and TSM biomaterial thin film faces revealed a high abundance and density of BMSCs adhering and proliferating on the bottom nanofibrous face for both the PLLA and TSM biomaterial thin films (**Figure 1.19A**). However, almost no cells were found on the smooth top faces for each of these groups (**Figure 1.19A**). Similarly, cross-sections of the TSM biomaterial thin film observed BMSCs penetrating throughout the entire nanofibrous bottom layer, but revealed significantly less BMSCs penetrating throughout the top smooth layer (**Figure 1.19B**). These results agreed with the frequently demonstrated literature results demonstrating that BMSCs prefer a nanofibrous surface topology because it allows them to adhere better to the surface for migration, proliferation, and differentiation. Nonetheless, this was an interesting result that suggested that the top smooth layer could serve as a barrier for cells in the TSM biomaterial thin film.

Finally, confocal microscopy of the stained BMSCs in the cross-sections of the TSM biomaterial and PLLA thin films revealed no difference in the absorbance of 570 nm light between

them at every time point of the experiment (**Figure 1.19C**). This implied that the TSM biomaterial thin films were just as conducive to BMSC proliferation and adhesion as the PLLA thin films. This is a significant result because PLLA is widely demonstrated to be highly conducive to BMSC proliferation, migration, and adhesion; therefore, imparting the favorable physical properties of the TSM biomaterial thin film while maintaining a conducive environment to BMSC proliferation presents a noteworthy advancement to the traditional PLLA biomaterial.

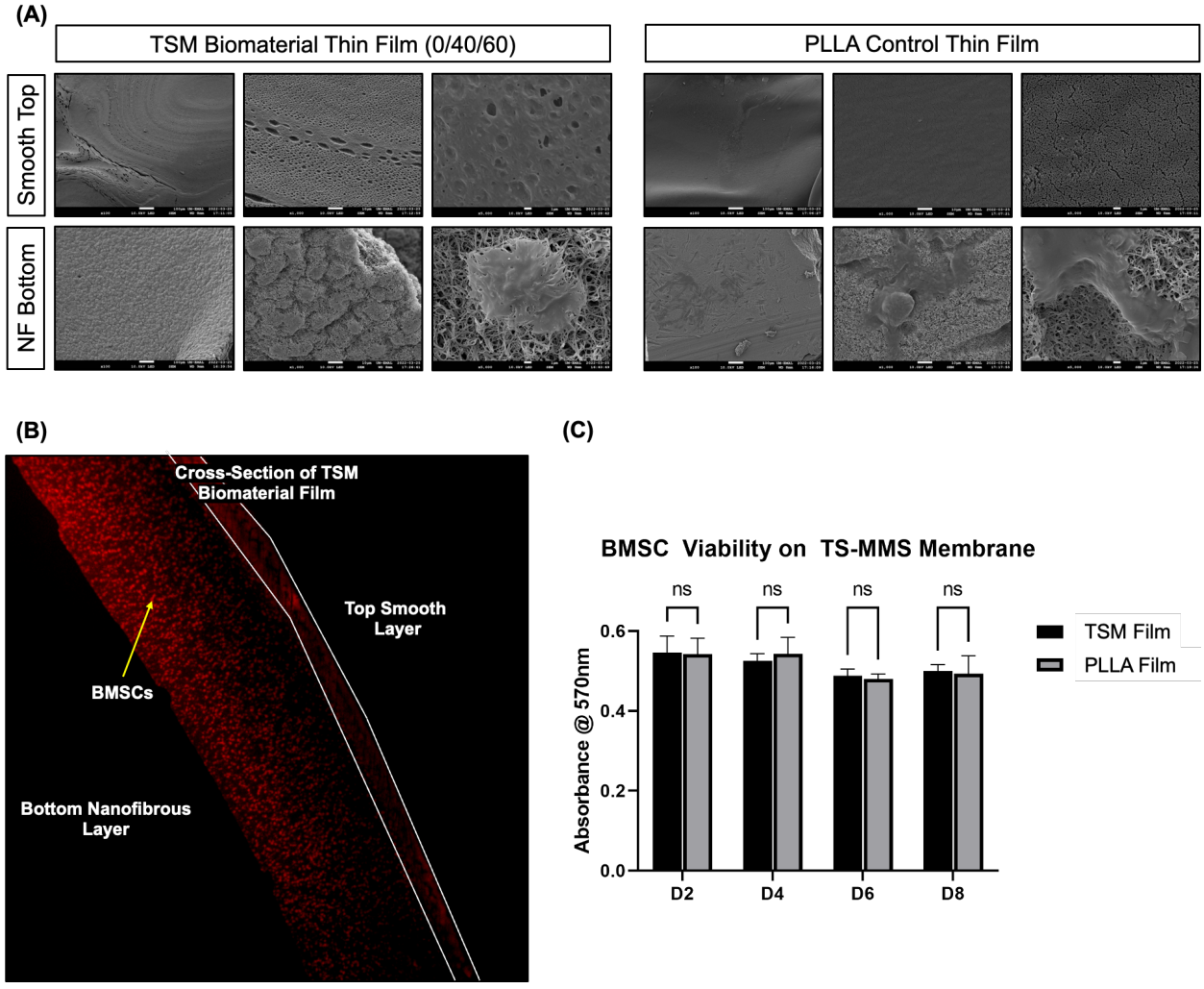

Figure 1.19: *In-vitro* experimental results from culturing bone-marrow derived stem cells (BMSCs) on TSM biomaterial and PLLA thin films. (A) Representative scanning electron microscopy images of different magnification of the top and bottom faces of the TSM biomaterial and PLLA thin films after the 8-day *in-vitro* experiment observing BMSC adhesion and proliferation. BMSCs were predominately observed in the bottom nanofibrous layer for each thin

film. (B) Confocal microscopy with a 570 nm excitation laser of a representative TSM biomaterial thin film cross-section after the *in-vitro* experiment showing the thin film penetration and distribution of BMSCs stained as red dots with NUCLEAR-ID® Red DNA stain. The top smooth layer is outlined by white borders and shows little fluorescence indicating that not many BMSCs are distributed in the top smooth layer. (C) Bar graph of the measured total mean absorbance of 570 nm light by TSM biomaterial and PLLA thin film cross-sections at different time points in the *in-vitro* experiment culturing BMSCs, which are stained with NUCLEAR-ID® Red DNA stain (λ_{abs} = 566 nm). This is quantitative indicator of BMSC proliferation on the thin films and reveals that there is no significant cytotoxicity of the thin films on BMSC proliferation. Error bars depict one measured standard deviation.

It was questioned whether the absence of BMSCs from the top smooth layer was a consequence of BMSC mechanobiology or if these results were applicable to different kinds of skeletal stem cells. Additionally, it was desirable to know if the side (i.e., bottom or top face) by which the skeletal stem cells were seeded onto the thin films made any impact in their proliferation on the TSM biomaterial construct. To address these questions, periodontal ligament stem cells (PDL-SCs) isolated from the periodontal tissues of mice were seeded either from the nanofibrous bottom side or the smooth top side of the TSM biomaterial constructs. They were also randomly seeded on the PLLA control thin film as the control. SEM analyses of the top and bottom faces of the TSM biomaterial thin film again revealed a dense cell population on the bottom nanofibrous face, but almost no cell populations on the top smooth face (**Figure 1.20A**). Moreover, the seeding side did not matter, indicating that the smooth-seeded TSM biomaterial thin films had their PDL-SC populations migrate around or through the TSM biomaterial thin film to the nanofibrous bottom side (**Figure 1.20A**). However, the PLLA control thin film was observed to have PDL-SCs on the nanofibrous bottom layer and in the cracks of the smooth thin top layer exposing the nanofibers directly underneath. Thus, the PLLA control thin films did not have as effective of a barrier as the TSM biomaterial thin films.

Cross-sections of the TSM biomaterial thin films again revealed that the PDL-SCs were locally concentrated in the nanofibrous bottom layer, regardless of cell-seeding (**Figure 1.20C**). Furthermore, comparison of the PDL-SC proliferation on the PLLA scaffolds and the TSM biomaterial scaffolds, regardless of cell-seeding side, was not measured to be statistically significant. Therefore, this was reasonable evidence to demonstrate that the trends observed in these *in-vitro* experiments were general to cell type and cell-seeding. The TSM biomaterial thin films were demonstrated to be as conducive as the PLLA thin films to skeletal stem cell proliferation and it was consistently demonstrated that the smooth top layer prevented cell adhesion and proliferation, but acted like a barrier for cells to migrate around. This result formed the basis of chapter 2.

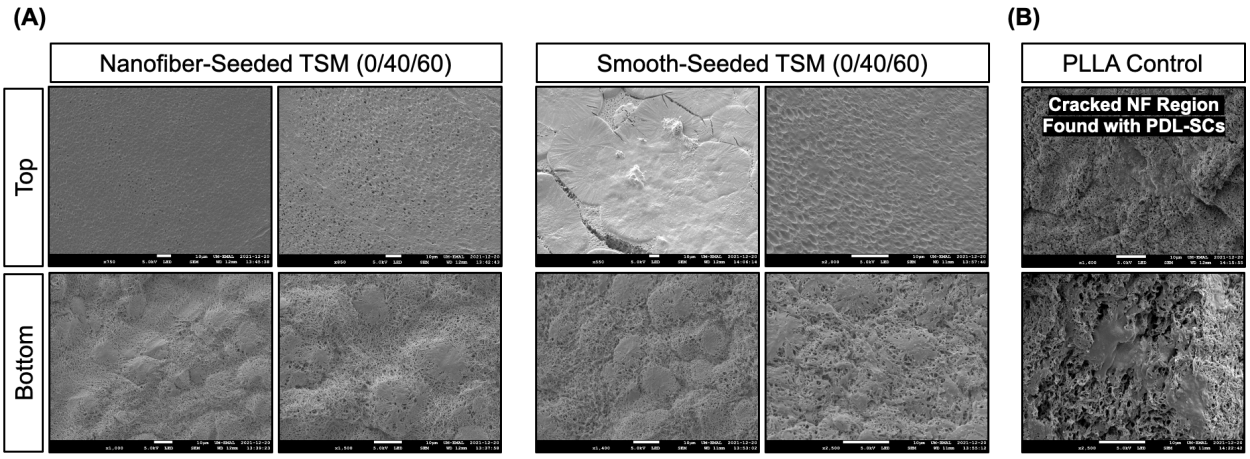

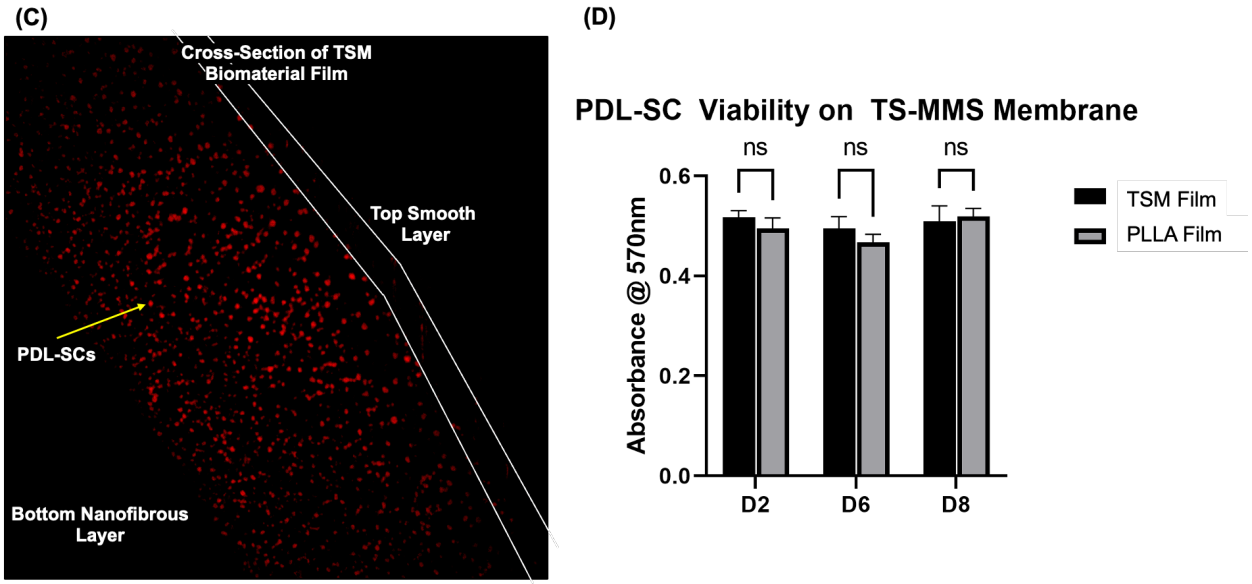

Figure 1.20: *In-vitro* experimental results from selectively-seeding periodontal ligament stem cells (PDL-SCs) on different faces of the TSM biomaterial and culturing them for different time periods with random side-seeded PLLA control thin films. (A) Representative scanning electron microscopy images of different magnification of the different face-seeded top and bottom faces of the TSM biomaterial after the 8-day *in-vitro* experiment observing PDL-SC adhesion and proliferation. BMSCs were predominately observed in the bottom nanofibrous layer for each thin film, even when seeded from the smooth side. (B) Representative scanning electron microscopy images of the top face and bottom face of the PLLA control thin films after the 8-day random side-seeding *in-vitro* experiment observing PDL-SC adhesion and proliferation. Note that there were several cracked, nanofibrous regions in the PLLA top face where PDL-SCs formed niches of proliferation, as shown in the top face SEM image above, opposed to proliferating directly on the thin smooth top layer. (C) Confocal microscopy with a 570 nm excitation laser of a representative nanofiber-seeded TSM biomaterial thin film cross-section after the *in-vitro* experiment showing the thin film penetration and distribution of PDL-SCs stained as red dots with NUCLEAR-ID® Red DNA stain. The top smooth layer is outlined by white borders and shows little fluorescence indicating that not many PDL-SCs are distributed in the top smooth layer. (D) Bar graph of the measured total mean absorbance of 570 nm light by TSM biomaterial and PLLA thin film cross-sections at different time points in the *in-vitro* experiment culturing PDL-SCs, which are stained with NUCLEAR-ID® Red DNA stain (λ_{abs} = 566 nm). Note that the smooth-seeded and nanofiber-seeded groups were combined because this bar graph was meant to measure if the TSM biomaterial itself was cytotoxic to PDL-SCs, and therefore cell-seeding was not a factor. This is a quantitative indicator of PDL-SC proliferation on the thin films and reveals that there is no significant cytotoxicity of the thin films on PDL-SC proliferation. Error bars depict one measured standard deviation for each group.

1.4 Conclusion

This chapter presented the fabricated the first known biomaterial construct capable of thermal shape memory and nanofiber formation via thermally induced phase-separation. This biomaterial was fabricated from a semi-interpenetrating network of PCL-DA in PLLA within a thin film construct and extensively optimized and characterized. It was discovered that this TSM biomaterial was thermosensitive at temperatures above 50C and achieved a rubbery state with better shaping properties or could recover its memorized shape via shape memory above this temperature. Additionally, the PCL-DA component was discovered to partially phase separate from PLLA to the top of the TSM biomaterial thin film, creating a biphasic morphology with a smooth top and nanofibrous bottom. Due to the differences in the hydrolytic degradation rates and hydrophilicity between PCL-DA and PLLA, the TSM biomaterial membrane was observed to have biphasic hydrolytic degradation whereby the nanofibrous bottom layer dominated by PLLA hydrolyzes before the top smooth layer dominated by PCL-DA.

Additionally, it was demonstrated that the incorporation of PLGA-DA into the PCL-DA semi-interpenetrating network within PLLA could increase the overall hydrophilicity of the TSM biomaterial thin for faster rates of hydrolytic degradation but without drastically altering the shape memory properties, biphasic morphology, or the biphasic hydrolytic degradation. Finally, these TSM biomaterial thin films were able to successfully proliferate BMSCs and PDL-SCs in their nanofibrous bottom layer at the same efficacy of PLLA thin films, but not in their smooth top layer. Future experiments should focus on applying the unique properties of the TSM biomaterial thin film to niche tissue engineering or drug delivery applications. Furthermore, the TSM biomaterial combinations should be investigated in a thick 3D scaffold construct to study if shape memory, biphasic morphology formation, or biphasic hydrolytic degradation still occur.

1.5 Materials and Methods

Materials and Reagents: Resomer 207S poly (L-lactic acid) was purchased from Evonik. All other reagents were purchased from Sigma Aldrich unless specifically mentioned in the below methods. Reagents were used as received unless otherwise specified.

Synthesis of Poly-ε-Caprolactone (PCL-diol): In the preparation of poly-ε-caprolactone (MW = ~10 kDa), 10 mL of ε-caprolactone monomer was added into a 50 mL round-bottom flask along with 89 µL of 1,4-butanediol (1 mol eq). Catalytic amounts (6.5 µL, 0.01 mol eq) of tin(II) 2-ethylhexanoate ($Sn(Oct)_2$) were added to a round-bottom flask with magnetic stir bar. The resulting solution was stirred at a low speed under vacuum, and heated to 120C and maintained for 12 hours resulting in a highly viscous solution. The reaction mixture was cooled to room temperature to form a white solid. A minimum volume of dichloromethane (DCM) was added to dissolve the white solid; the resulting solution was precipitated into 300 mL of methanol (~5x volume) at 0C yielding a white solid. This solution was then centrifuged (3,500 rpm x 10 min) to concentrate the solid and remove the supernatant. This precipitation procedure was repeated three times to remove unreacted monomer and catalyst. The solid, PCL-diol, was allowed to dry for two days in a vacuum chamber and stored at -20C before further use. Molecular weight was assessed by gel permeation chromatography (GPC) in tetrahydrofuran (THF) solvent. Molecular characterization is performed by nuclear magnetic resonance spectroscopy (NMR, CDCl3) and Fourier-transformed infrared spectroscopy (FTIR).

Synthesis of Poly-ε-Caprolactone Diacrylate (PCL-DA): PCL-diol was functionalized with terminal acrylate functional groups to impart cross-linking ability. 5 g of PCL (MWavg = 10.47 kDa by GPC) was added to a 50 mL round-bottom flask and dissolved in a minimum volume of anhydrous DCM. 135 µL of triethylamine (TEA, 2 mol eq) was added with stirring at moderate speed (~500 rpm). After 15 minutes, 78 µL of acryloyl chloride (AC) was added dropwise into the solution over the course of 10 minutes using a syringe. The reaction was left to proceed overnight under moderate stirring, warming to room temperature as the ice bath melted. The resulting reaction mixture was precipitated into 300 mL of methanol (~5x vol) at 0C in a beaker to precipitate a white solid. This solution was then centrifuged (3,500 rpm x 10 min) to concentrate the solid and remove the supernatant. This precipitation procedure was repeated three times to remove unreacted AC and remove TEA. The solid PCL-DA was allowed to dry for two days in a vacuum chamber and stored at -20C before further use. End group functionalization was confirmed by NMR (CDCl3) and FTIR.

Synthesis of Poly Lactic-co-Glycolic Acid (PLGA): In the preparation of poly lactic-co-glycolic acid (50:50 lactide-glycolide ratio, MW ~ 10,000 Da), *L*-lactide (7.6 mmol, 1.10 g, 1 mol eq) and ε-caprolactone (7.6 mmol, 0.88 g, 1 mol eq) were added to a round-bottom flask with benzyl alcohol (initiator, 0.2 mmol, 208 µL, 0.027 mol eq). The reaction was heated 120C under vacuum with moderate stirring then 100 µL of $Sn(Oct)_2$ (catalyst, 0.001 mol eq) was injected. After twelve hours, the reaction was opened to air and allowed to cool to room temperature resulting in a colorless solid. A minimum volume of DCM (approximately 20-30 mL) was used to completely dissolve this solid, and the resulting solution was precipitated into 300 mL of -20C methanol (10x vol eq) resulting in a white solid. The supernatant was poured off and the PLGA was dried for two

days in a vacuum chamber and stored at -20C before further use. This precipitation procedure was repeated three times. The solid PLGA was allowed to dry for two days in a vacuum chamber and stored at -20C before further use. Chemical identity and lactide-glycolide ratio was confirmed by NMR (CDCl3) and FTIR. Molecular weight was determined by GPC.

Synthesis of Poly Lactic-co-Glycolic Acid Diacrylate (PLGA-DA): PLGA was modified to obtain terminal acrylic functional groups for cross-linking. To synthesize poly lactide-co-glycolic acid diacrylate (PLGA-DA), PLGA (0.50 mmol, 5 g, MW ~ 10,000 Da) was transferred into a round-bottom flask in an ice bath and dissolved in 30 mL DCM. TEA (1 mmol, 80.1 µL, 2 mol eq) was added the resulting solution was stirred at moderate speed on ice. After 15 minutes, acryloyl chloride (1 mmol, 140 µL, 2 mol eq) was injected dropwise into the solution. The reaction was allowed to proceed overnight under moderate stirring, slowly warming to room temperature in the melting-ice bath. After this time elapsed, the reaction was precipitated into 300 mL of methanol at 0C, resulting in a white PLGA-DA solid. This solution was centrifuged to concentrate the PLGA-DA solid such that the supernatant could be removed. This precipitation procedure was repeated three times. PLGA-DA solid was allowed to dry for two days in a vacuum chamber and stored at -20C before further use. End group functionalization was confirmed by NMR (CDCl3) and FTIR.

Synthesis of Nile Blue-PLLA: Nile blue-PLLA was prepared according to our previous method. Briefly, acrylic-end functionalized PLLA was synthesized from hydroxyethyl methacrylate (HEMA) initiator (0.4 mmol, 100 µL) and *L*-lactide (34.7 mmol, 5.00 g), with $Sn(Oct)_2$ (120 µL) in a ring opening polymerization reaction (ROP) at 120°C, in an inert nitrogen environment. After

twelve hours, the resulting HEMA-PLLA polymer was exposed to air, cooled, then dissolved in 20 mL chloroform and precipitated in 100 mL cold methanol and the product was collected. End group functionalization was confirmed by NMR (CDCl3) and FTIR. HEMA-PLLA (1.40 g), nile blue acrylamide (0.012 mmol, 0.005 g), and freshly recrystallized AIBN (0.06 mmol, 0.0098 g, recrystallized from methanol) were dissolved in 10 mL dioxane at 70°C and allowed to react overnight. Solvent was removed by rotary evaporation, and the resulting residue was dissolved in a minimum amount of chloroform and precipitated into cold methanol, then collected by suction filtration.

Synthesis of Fluorescein isothiocyanate-PCL (FITC-PCL): FITC-PCL was prepared according to a modification of our previous method. Briefly, acrylic-end functionalized PCL was synthesized from hydroxyethyl methacrylate (HEMA) initiator (0.4 mmol, 100 μL) and ε-caprolactone (44 mmol, 5.00 g), with $Sn(Oct)_2$ (120 μL) in a ring opening polymerization reaction (ROP) at 120°C, in an inert nitrogen environment. After twelve hours, the resulting HEMA-PCL polymer was exposed to air, cooled, then dissolved in 20 mL chloroform and precipitated in 100 mL cold methanol and the product was collected. End group functionalization was confirmed by NMR (CDCl3) and FTIR. HEMA-PCL (1.40 g), FITC-o-acrylate (0.012 mmol, 0.005 g), and freshly recrystallized AIBN (0.06 mmol, 0.0098 g, recrystallized from methanol) were dissolved in 10 mL dioxane at 70°C and allowed to react overnight. Solvent was removed by rotary evaporation, and the resulting residue was dissolved in a minimum amount of chloroform and precipitated into cold methanol, then collected by suction filtration.

Film Template Design and Fabrication: TinkerCAD online software was used to design rectangular casting molds with an outline of 73 x 23 x 2 mm dimensions containing a central hollow rectangle of 60 x 10 x 2 mm dimensions for holding the polymer solution during casting and UV-induced crosslinking. An additional design was created for casting smaller films, which the same outline dimensions as the prior design, but partitioned the central hollow rectangle lengthwise into four 13 x 10 x 2 mm hollow sections, each walled off from the adjacent sections by a 1.5 x 10 x 4 mm solid barrier. All casting molds were 3D printed from PLLA using an Original Prusa i3 MK3S+ 3D Printer. The 3D printed mold outlines were glued to the charged side of ASi Supreme™ Plus Microscope Slides using Gorilla Glue Super Glue® and allowed to dry in a ventilated hood for two days prior to polymer casting.

Biphasic TSM Biomaterial Film Fabrication: In general, film molds for polymer casting were placed in a FisherScientific® UV Crosslinking Chamber (λ = 256 nm) powered at E = 10 J. A 3 mM stock solution of Irgacure® 2959 photoinitiator was prepared in methanol and stored at -20C. Separately, a 10% w/v polymer solution in tetrahydrofuran (THF) was prepared from varying w/w/w ratios of PLGA-DA, PCL-DA, and PLLA, respectively. The polymer solution was heated to 62C in a convection oven for at least two hours or until the polymers were completely dissolved. Once the polymer solution was dissolved, it was removed from the convection oven to be immediately injected with the photoinitiator stock solution (3.33% v/v), and mixed before being rapidly transferred into the film molds (approximately 2 - 2.5 mL of solution per film mold) with a transfer pipette. Once the UV crosslinking chamber was shut the films were allowed to crosslink for five minutes, unless otherwise specified. After the time has elapsed, the film molds were removed from the UV crosslinking chamber and rapidly transferred onto flat slabs of dry ice to

induce thermally induced phase separation (TIPS) of PLLA responsible for nanofiber formation. After 5-10 minutes, the films were transferred into a -80C freezer to continue TIPS, for 48 hours.

After 2 days at -80C, the films were removed from the freezer and placed into an ice bath. They soaked for approximately 3 hours while gradually warming to room temperature in the bath, turning bright white. Once at room temperature, the films were removed from the water and the polymer film construct was cut out of the film mold using a razor blade. The resulting films were dried flat for 4 days then stored at -20C until further use.

Sterilization of Biomaterial Constructs: Prior to all *in vitro* and *in vivo* work, PLLA scaffolds were sterilized by a dual-sterilization method. First, constructs were sterilized by ethylene oxide gas according to the manufacturer's protocol (Anpro). Secondly scaffolds were washed with 70% ethanol for 30 minutes, followed by washing with PBS then with cell culture media, immediately before cell seeding. The purpose of the ethanol wash is twofold – first, a secondary sterilization method, and second, to "wet" the surface of the hydrophobic PLLA scaffold prior to cell seeding.

Nuclear Magnetic Resonance (NMR) Spectroscopy: Synthesized polymers were characterized by nuclear magnetic resonance (NMR) spectroscopy to confirm their molecular identity and reaction efficiency. 1H spectra were recorded with a Varian MR400 spectrometer operating at 400 MHz and room temperature. Spectra were observed in deuterated chloroform ($CDCl_3$). Spectral analysis is carried out in VnmrJ (Version 4.2, Agilent) and MestReNova (Version 12.0.0-2000080, Metrelab Research).

Scanning Electron Microscopy: The surface morphology of all biomaterial constructs was observed by scanning electron microscopy (JEOL JSM-7800 FLM) with an accelerating voltage of 5 kV and working distance of 10-15 mm. Prior to observation, samples were coated with gold using a sputter coater (Desk II, Denton Vacuum Inc.).

Confocal Laser Microscopy: Fluorescently active probes were observed from substrates by confocal laser microscopy (Nikon Eclipse C1).

Statistical Methods: All data are reported as mean ± standard deviation and represent a minimum sample size of $n>3$. Statistical analysis was carried out in GraphPad Prism v8. Student's t-test was used to determine statistical significance of observed values between experimental groups where $p < 0.05$ was considered significant. Tukey's test was used to determine differences between group means as a single-step method to compare multiple means and determine statistical significance between. Statistical analyses were carried out under the guidance of the University of Michigan Consulting for Statistics, Computational and Analytical Research Center. In all graphics, significance is noted as: * $p<0.05$, ** $p<0.01$, *** $p<0.001$, **** $p<0.0001$.

Image Analysis: All image analysis was carried out in Fiji imaging software (Image J Image J, V 1.0.0-rc-69/1.52p). Images were imported as raw files (.TIF). Analyses were carried out using batch macros following optimized protocols.

X-ray Diffraction: A Rigaku Ultima IV Diffractometer was used to acquire small angle X-ray scattering spectra from solid phase polymer samples. X-ray generation occurs within a 2.2 kW Cu

K-alpha radiation long-fine focus tube (0.4 x 12 mm) with cross beam optics. Scans are performed with a Theta/Theta wide angle goniometer from -3deg to +154deg (2 theta) at 1 degree/minute. Signal is detected with a D/teX-ULTRA high-speed detector.

Thermogravimetric Analysis: To determine the degradation behavior of our materials, a TA Instruments Discovery TGA was used according to protocols developed by the manufacturer with a heating rate of 10degC/min in the range from 20degC to 250degC in nitrogen atmosphere with a purge rate of 25 mL/min. All analyses were carried out in triplicate.

Differential Scanning Calorimetry: To determine the thermal and melting properties of our materials, a TA Instruments Discovery DSC was used according to protocols developed by the manufacturer with a scanning rate of 5degC/min. Each material was kept in aluminum pans and an empty pan was used as the reference. All analyses were carried out in triplicate.

Histologic Assessment: Samples were harvested and fixed with 4% paraformaldehyde, and processed as described below.

Mechanical Testing: Mechanical properties of scaffolds were measured using an MTS Synergie 200 mechanical tester (MTS Systems, Inc.) Tensile modulus was defined as the initial linear modulus on the resulting stress-strain curve, with a strain rate of 1.0 mm/minute.

Shape-Memory Thermal Cycling: A digital ceramic hot plate with temperature probe was used to regulate the temperature of water baths. Scaffolds were placed in the water bath and held under

water for 30 seconds gently using forceps. After this time, the scaffolds were mechanically coiled by-hand around a 1 mm diameter metal rod (approximately 2-4 coils). This was immediately transferred into an ice bath to rapidly lock the new structure. To complete the thermal cycle and trigger shape-memory, the locked-structure film was transferred back into the 80 C water bath and rapidly found its flat, straight original shape with high integrity. This comprised one shape-memory thermal cycle and was repeated several times for some films.

Timed Recovery of Film Shape-Memory: Two beakers were filled with arbitrary levels of water and heated to 55 C and 80 C, respectively using a digital ceramic hot plate with temperature probe. Films underwent shape-memory thermal cycling in the 80 C water bath by the method previously described; the shape-memory activation step was digitally recorded using a digital camera and performed in the 80 C bath or the 55 C bath, as the temperature of recovery was an independent variable. The recorded videos were then analyzed with to measure the time of recovery. Films that did not possess thermosensitive components did not actively make significant progress to recover the original shape, especially at lower recovery temperatures, and thus no measurement as recorded.

Primary cell isolation: Primary bone marrow stromal cells (BMSCs) were isolated from femora and tibiae of 3-week-old mice and then cultured in Dulbecco's Modified Eagle Medium (DMEM) containing 10% FBS. All cells were used for experiments before passage 4. Their character as MSCs was characterized as described below as well as gene expression profile, shown in Fig 2, respectively. These procedures were performed following a protocol approved by the University of Michigan Institutional Animal Care and Use Committee (IACUC).

Cell culture of 3D Tissue Constructs: Membranes were soaked in 70% ethanol for 30 min and washed three times with PBS for 10 min each, then washed with cell culture media. Primary cells (0.5 x 105 cells/membrane) were seeded in 10 uL media. One hour later, culture media was gently added to cover the 3D constructs.

In vitro cell migration assay: Primary BMSCs were seeded to either the nanofibrous or smooth side of membrane constructs and cultured as described. At specified endpoints, constructs were fixed in 4% PFA for 24 hours at 4C and embedded in paraffin for sectioning in the transverse direction to observe migration into the construct. Constructs were deparaffinized and stained with AlexaFlor-Phalloidin and Hoesct. Sections were observed by confocal laser microscopy.

In vitro cell culture Primary BMSCs were seeded to both sides membrane constructs and cultured as described. At specified endpoints, films were fixed in 4% PFA at 4C for 24 hours. Cells were stained with AlexaFlor-Phalloidin and Hoesct. Whole films were observed by confocal laser microscopy.

Chapter 2

Fabrication of a Tissue Engineering Membrane with Unidirectional Drug Delivery from a Biphasic Thermosensitive Shape Memory Biomaterial

2.1 Abstract

Current periodontal tissue engineering membranes are designed to either emphasize regeneration or defect protection from the oral cavity while a separate material underneath is placed to facilitate regeneration. This chapter rectifies this problem by applying the partial phase separation of PCL-DA and PLLA within a thermosensitive shape memory (TSM) biomaterial thin film construct and its consequential biphasic morphology from chapter 1 to develop a novel tissue engineering membrane for periodontal regeneration capable of defect protection and regeneration. This tissue engineering membrane presents high sutureability and shapeability at clinically-feasible transition temperatures, but resists suture pull-out at physiological temperatures. Furthermore, a novel drug delivery system was installed into the nanofibrous bottom layer of these membranes by embedding PLGA nanoparticles encapsulating protein and small molecule therapeutics into the nanofibers. The nanoparticles were unidirectionally released due to the biphasic hydrolytic degradation of the membranes at an approximately linear rate measured for up to 81 days, allowing for sustained unidirectional therapeutic delivery. The drug delivery system was used to deliver platelet-derived growth factor (PDGF) *in-vivo* directly into a periodontal defect, resulting in significantly enhanced periodontal regeneration and bone mineralization in a critically-sized periodontal defect rat model that outperformed a clinical-standard commercial brand of FDA-approved periodontal membranes. Overall, this membrane technology presents a versatile strategy for facilitating tissue regeneration and sustained therapeutic delivery, while also

offering protection from the oral cavity and possessing convenient clinical-handling properties. It represents an important advance over current periodontal membranes.

2.2 Introduction

Periodontal disease is an infection of the gum and periodontal tissues that oftentimes progresses to infect and destroy teeth and parts of the jawbone.[22] According to the World Health Organization, it is a disease that affects more than 1 billion people worldwide;[5,22] there is a significant need for damaged periodontal and jawbone tissues to be regenerated with biomaterial and tissue engineering strategies since those tissues will not regenerate on their own. Tissue engineering membranes and regenerative biomaterials held in place by periodontal barrier membranes present are a promising strategy for periodontal regeneration, but their current limitations hinder their efficacy.[22] Namely, current tissue engineering membranes that focus on regenerating the periodontal tissue do not adequately protect the defect from the oral cavity, leading to suboptimal healing outcomes. On the other hand, periodontal barrier membranes serve almost solely to act as a protective layer from the oral cavity for an additional biomaterial underneath facilitating regeneration, but the periodontal barrier membrane is not very effective at contributing to the regeneration itself. In addition, this is a more costly and delicate procedure.[22] Several studies have demonstrated that simultaneous regeneration and protection are necessary for optimal healing, highlighting the need for advanced membranes that can achieve both objectives.

Moreover, the fields of dentistry and periodontics have identified protein growth factors like platelet-derived growth factor (PDGF) as significant positive contributors to periodontal and jawbone regeneration.[17,18] Thus, many clinicians use PDGF in their own practices, but the method they use to administer it is uncontrolled and inconsistent. Typically, this consists of wetting a

biomaterial in a PDGF solution one time directly before implantation, making it a one-time dose of an unknown amount of PDGF.[17,18,22] This demands a solution in the form of a sustained drug delivery system, ideally within or on a biomaterial construct such that implanting the biomaterial also implants a sustainable drug delivery system that requires no further intervention.

The aims of the research project presented in this chapter sought to utilize the biphasic TSM biomaterial thin film from chapter 1 as a periodontal membrane, where the smooth top layer acts as an impermeable, protective layer while the nanofibrous bottom layer facilitates periodontal and jawbone tissue regeneration underneath. Furthermore, this research project sought to install a drug delivery system within the nanofibers of the TSM biomaterial thin film such that its gradual hydrolytic degradation would sustainably release therapeutics such as PDGF into the defect to stimulate regeneration.

2.3 Results and Discussion

2.3.1 Clinically Relevant Properties of the Biomaterial Tissue Engineering Membrane

The unique physical properties of the TSM biomaterial thin films presented translational potential to a clinical setting as tissue engineering membrane. Specifically, the demonstrated thermosensitive properties of the TSM biomaterial thin film allowing it to achieve a rubbery state past the T_{M1} make it optimal for precision shaping and implantation into clinical defects by clinicians. Additionally, the biphasic morphology of the TSM biomaterial thin film was demonstrated to present different interactions with skeletal stem cells on different sides of the thin film. The nanofibrous bottom layer was conducive to skeletal stem cell adhesion, proliferation, and migration but the smooth top layer was not permeable to cell migration and it was not observed to promote adhesion or proliferation. This suggested that each side of the thin film could serve

different functions as a tissue engineering membrane. For example, the smooth layer could serve as a protective, impermeable barrier to an exposed cavity or separate tissue while the nanofibrous bottom layer promoted regeneration in the area of the defect underneath. This is ideal in the context of a periodontal tissue engineering membrane for periodontal regeneration because one surface of the membrane is exposed to the oral cavity while the other surface faces into the jawbone defect underneath that needs to be regenerated. Thus, it was hypothesized that the TSM biomaterial thin film could be applied as a periodontal tissue engineering membrane where the smooth layer faces the oral cavity to offer protection while the nanofibrous layer regenerates the bone underneath.

Commercial periodontal membranes are highly sutureable by design because they are exposed to many forces in the dynamic environment of the oral cavity and are often implanted into defects at angles or upside-down. They must be sutured tightly into the surrounding gum tissue to maintain stability over the defect, hence their sutureable design. It was necessary to investigate the suturability of the TSM biomaterial thin film to ensure it would be an appropriate periodontal tissue engineering membrane. To this end, the resistance towards suture pull out was measured for PLLA control thin films and 0/40/60 TSM biomaterial thin films to investigate if they could competently maintain a tight suture and sutureable they were. Thin films were sutured into at one end and clamped into the bottom portion of a mechanical testing machine while the suture was clamped into the top part of the mechanical testing machine (**Figure 2.1A**). The suture pull out tensile modulus was measured for the PLLA and TSM biomaterial thin films heated to 37C and 80C (**Figure 2.1B**).

If the thin film was stronger than the tensile stress exerted by the suture under tensile strain by the machine, then the thin film did not compromise and the tensile modulus of the suture material was measured. Thus, the thin film was determined to successfully resist the suture pull out for a

tight suture. There was no significant measured difference between the suture pull out tensile modulus of the TSM biomaterial thin film at 37C and the PLLA thin film at 37C and 80C. Furthermore, these measured tensile moduli were on the magnitude of ten kilopascals. Therefore, these measurements were attributed to the suture material tensile modulus because the PLLA and TSM biomaterial thin film tensile moduli were measured to be on the magnitude of 100 kilopascals in Chapter 1. This confirmed that the PLLA and TSM biomaterial thin films were able to resist suture pull out physiologic temperature, and that the PLLA thin film also resisted suture pull out at 80C. However, the TSM biomaterial thin film had a statistically lower measured suture pull out tensile modulus at 80C than at 37C, indicating that the material was softer and unable to resist the tensile stress exerted by the suture. This is because 80C exceeds the T_{M1} of the TSM biomaterial where it transitions to a rubbery state. However, this result implies that the TSM biomaterial thin film is easier to suture into at temperatures above its T_{M1} because it is softer; therefore, the TSM biomaterial is highly sutureable at temperatures that it would shaped and implanted at due to its rubbery state, but resists suture pull out once it cools below the T_{M1} to physiologic temperature and locks its shape. This is highly advantageous for clinical-handling and unique to the TSM biomaterial thin film, confirming that the favorable sutureable properties of periodontal tissue engineering membranes were met by the TSM biomaterial thin film.

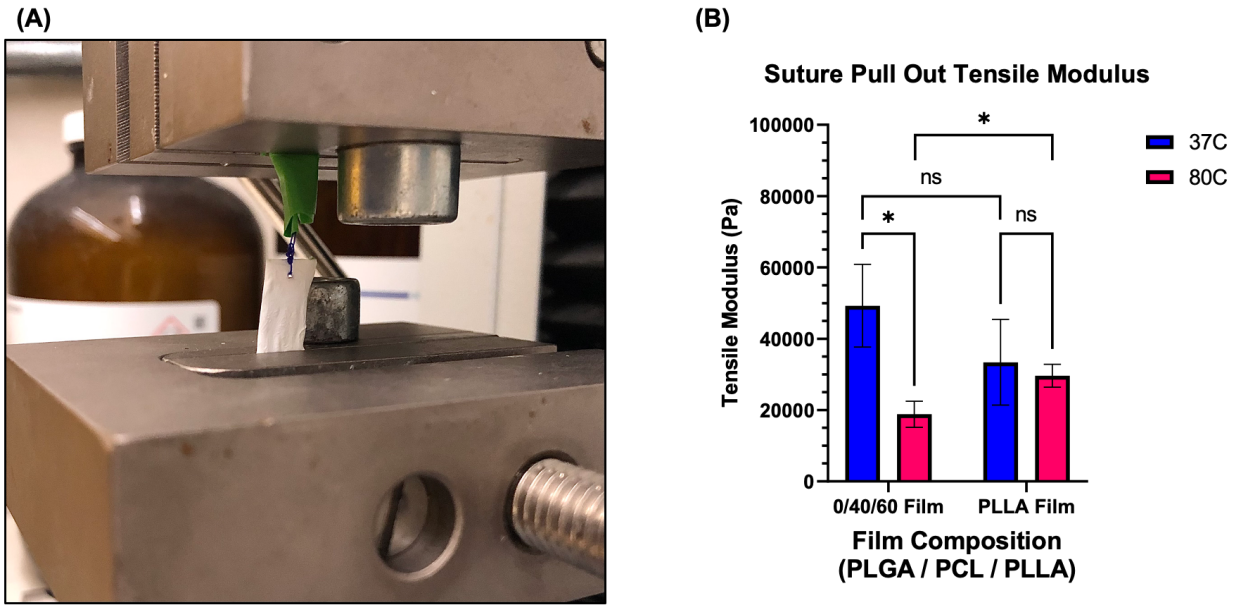

Figure 2.1: Schematic of the suture pull out experiment. (A) Experimental photograph of a sutured TSM biomaterial film composed of 40% PCL-DA and 60% PLLA (0/40/60) being measured in the mechanical tester for its suture pull out tensile modulus at 37C. (B) Bar graph of the measured mean suture pull out tensile moduli for the PLLA control thin film and the 0/40/60 TSM biomaterial thin film measured at 37C and 80C. Note that the error bars depict one measured standard deviation above or below mean for each group.

The PLLA and TSM biomaterial thin films were fabricated to be two millimeters in thickness up until this point because their molds were 3D-printed to have this dimension. Although this would be sufficiently thin for human patients, the TSM biomaterial thin films were to be demonstrated in rodent periodontal defect models where they would have to fabricated to be half of a millimeter in thickness to fit the size constraints of previously demonstrated rodent periodontal defect models.[22] There was concern that reducing the thickness of the TSM biomaterial thin films would destroy their intended biphasic morphology. This concern was investigated by fabricating TSM biomaterial thin films that were 0.5 mm in thickness and analyzing their top and bottom face surface topologies with SEM (**Figure 2.2A,B**). It was observed that the top face still maintained a smooth surface topology while the bottom face still maintained a nanofibrous surface topology. Thus, the fabrication thickness of the TSM biomaterial thin film did not significantly alter the

biphase formation at a 0.5 mm and 2 mm thickness. Ultimately, the TSM biomaterial thin film was demonstrated to meet the physical criteria necessary for implantation as a periodontal tissue engineering membrane while maintaining its unique biphasic morphology. Herein, the TSM biomaterial thin film is interchangeably referred to as a membrane, periodontal membrane, or tissue engineering membrane.

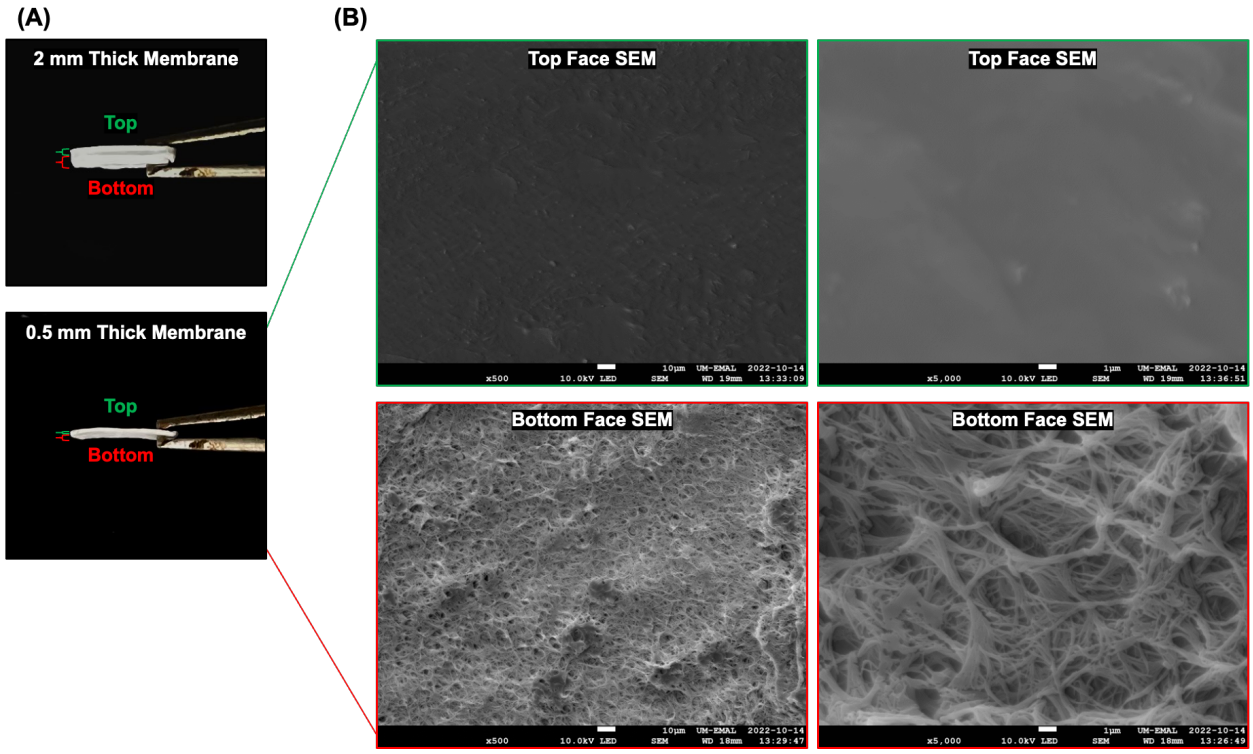

Figure 2.2: Comparison of the morphologies and surface topologies for TSM biomaterials composed of 20% PLGA-DA, 20% PCL-Da, and 60% PLLA (20/20/60) fabricated at different thicknesses. (A) Photographs of a 20/20/60 TSM biomaterial thin film fabricated at 2 mm thick and 0.5 mm thick, respectively. Note that the biphasic morphologies can be visually observed for both. (B) Representative scanning electron microscopy images of different magnifications of the top and bottom faces of the 0.5 mm thick 20/20/60 TSM biomaterial thin film. This confirms that the biphasic morphology and surface topology is still present in the thinner film. Herein, the 0.5 mm thick TSM biomaterial thin films are referred to as membranes.

2.3.2 Embedded Unidirectional Drug Delivery System using Nanoparticles

Biological tissues function and regenerate in response to combinations of physical and chemical cues in their microenvironment.[10] Tissue engineering repair and regeneration outcomes

can therefore be controlled with higher efficacy and predictability when both of these types of factors are accounted for. The TSM biomaterial membrane presents a flat, nanofibrous surface with a relatively high tensile modulus that is highly conducive to skeletal stem cell adhesion, proliferation, migration, and differentiation into osteogenic fates based on the preliminary *in-vitro* experiments from chapter 1 and the known mechanobiology of skeletal stem cells.[10] However, it was hypothesized that this physical microenvironment for periodontal regeneration could be further enhanced by incorporating biomolecular growth factors that promote favorable processes for bone formation. Platelet-derived growth factor (PDGF) is a growth factor known to promote angiogenesis, osteogenesis, chemotaxis, proliferation, and extracellular matrix remodeling conducive to bone formation and maturation that is well-demonstrated in dental regeneration applications. However, the current clinical standards for applying PDGF to a dental defect are crude and inconsiderate of dose or sustained release.

Nanoparticles encapsulating PDGF sought be embedded into the nanofibers of the TSM biomaterial membrane to controllably deliver PDGF over a sustained time-period through the gradual hydrolysis of the nanofibers and nanoparticles (**Figure 2.3**). Furthermore, this drug delivery system was hypothesized to directionally release therapeutics in the direction of nanofibrous bottom layer because of the demonstrated TSM biomaterial membrane biphasic hydrolytic degradation profile, whereby the hydrophilic, nanofibrous bottom layer hydrolyses before the hydrophobic and impermeable smooth top layer (**Figure 2.3**). Thus, the PDGF release from the nanofibrous bottom layer would be sustained and unidirectional into the periodontal defect, which maximizes the delivery, predictability, and control over the release.

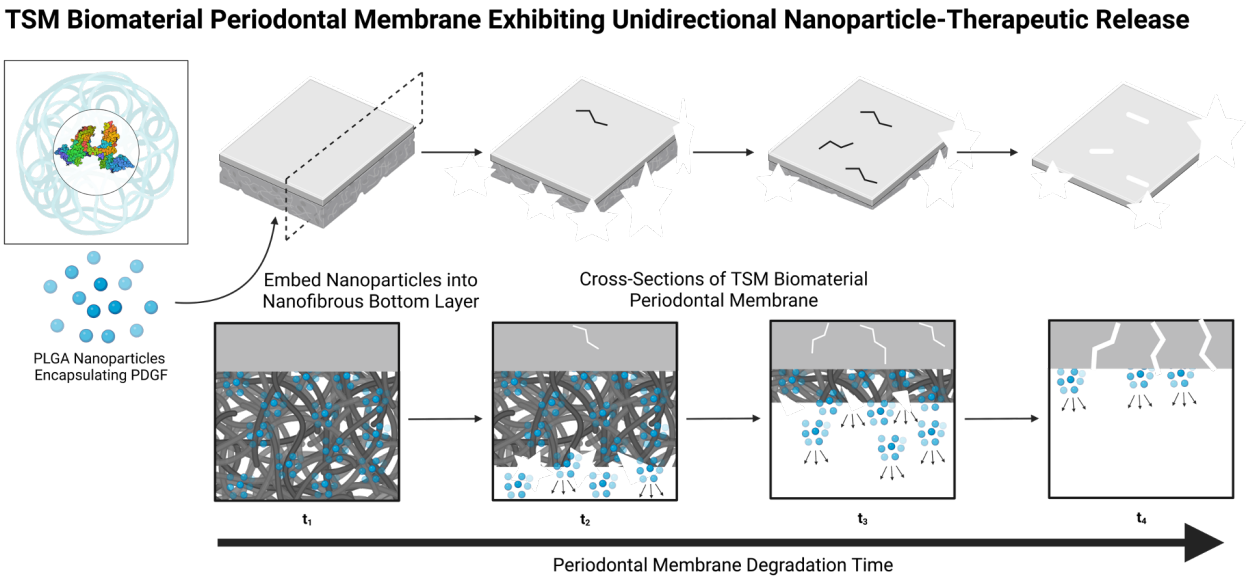

Figure 2.3: Visual schematic of the designed nanofiber-embedded drug delivery system for the TSM biomaterial membrane and its hypothesized unidirectional release mechanism through biphasic hydrolytic degradation. This drug delivery system utilizes PLGA nanoparticles encapsulating a therapeutic, such as platelet-derivered growth factor (PDGF) as shown in this figure.

Optimizing the installation of a nanofiber-embedded, nanoparticle drug delivery system and evaluating its release kinetics was planned to be executed with PLGA nanoparticles encapsulating fluorescent molecules because of their convenience for visual spatial-tracking and concentration quantification via fluorometric methods. PLGA nanoparticles encapsulating either rhodamine b or fluorescein isothiocyanate (FITC)-bovine serum albumin (BSA) were fabricated using a common double w/o/w emulsion procedure in the literature to demonstrate the incorporation of a small molecule and a macromolecule in the drug-delivery system, respectively (**Figure 2.4**).[4,11,24] The morphologies of the dried nanoparticle products were first investigated by SEM (**Figure 2.5B**). Homogenous, spherical nanoparticles were observed ranging in diameter from hundreds of nanometers to the micrometer scale for both groups of nanoparticles containing either FITC-BSA or rhodamine b, with most nanoparticles on the magnitude of hundreds of nanometers. This

confirmed that the w/o/w double emulsion procedure yielded stable PLGA nanoparticles, and that the encapsulated molecule did not affect nanoparticle formation or morphology.

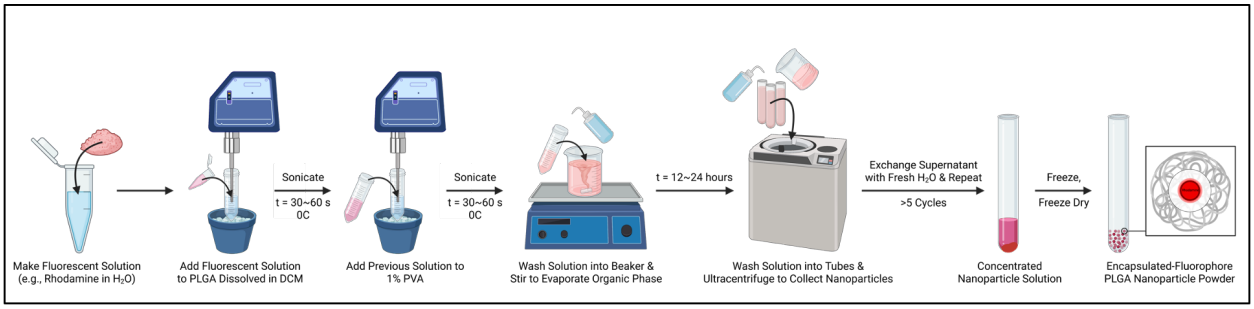

Figure 2.4: Visual schematic of the general w/o/w double emulsion procedure used to make PLGA nanoparticles encapsulating a molecule. This example utilizes rhodamine, but the method is general to small-molecules and macromolecules.

Transmission electron microscopy (TEM) was additionally performed on a prepared sample of PLGA nanoparticles encapsulating FITC-BSA to confidently ensure that the large FITC-BSA protein, similar in size to PDGF, was being encapsulated in the PLGA nanoparticles (**Figure 2.5C**). The TEM microscope required that the dried nanoparticle product be partially dissolved in methanol and drop-casted onto the TEM grid to obtain a fine enough sample for imaging (**Figure 2.5A**). During this process, the morphology of the nanoparticles was compromised such that upon drop casting and methanol evaporation the FITC-BSA aggregated and crystallized within the aggregated PLGA polymer for visual convenience during the TEM analysis. The FITC-BSA crystals could be observed as dark spots and patches in the TEM images, matching TEM images of proteins in the literature.[7] This experiment qualitatively concluded that there was FITC-BSA present in the PLGA nanoparticles.

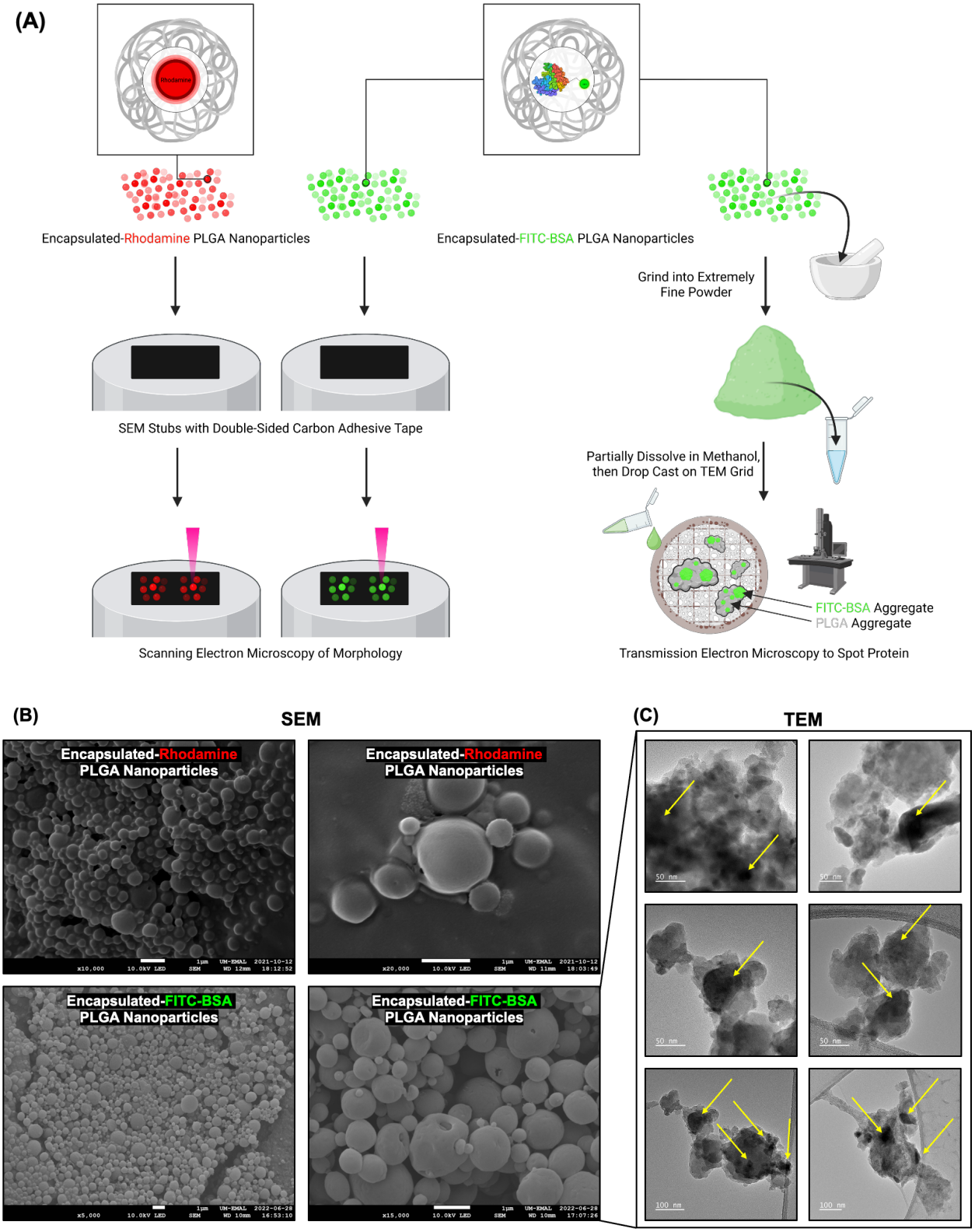

Figure 2.5: Characterization of PLGA nanoparticles encapsulating fluorescent molecules of drastically different molecular weights. (A) Visual schematic of the PLGA nanoparticles

encapsulating rhodamine b or FITC-BSA and their preparation for scanning electron microscopy and transmission electron microscopy. Note that the PLGA nanoparticles encapsulating FITC BSA are the only nanoparticles used for transmission electron microscopy. (B) Representative scanning electron microscopy images of the morphologies for PLGA nanoparticles encapsulating rhodamine b or FITC-BSA, respectively. (C) Representative transmission electron microscopy images revealing the presence of crystallized FITC-BSA proteins (yellow arrows and other dark spots) within the dissolved and drop-casted PLGA nanoparticles encapsulating FITC-BSA. Note that the morphology of the nanoparticles was compromised from the drop-casting step, and that the PLGA is aggregated with FITC-BSA crystals; this serves as a qualitative method to confirm that the nanoparticles contained encapsulated FITC-BSA prior to drop-casting.

After establishing confidence in the quality of the PLGA nanoparticles it was necessary to design a method to embed them in nanofibers the TSM biomaterial membranes. It was hypothesized that casting the dissolved TSM biomaterial onto a thin bed of dried nanoparticles in the film mold would lightly resuspend the nanoparticles such that they remained localized and embedded in the nanofibrous bottom layer during TIPS. To ensure that the nanoparticles were evenly spread out into a thin layer on the film mold prior to casting with the TSM biomaterial, they were vortex resuspended in various solvents and poured into the film molds for solvent evaporation (**Figure 2.6A**). Water and ethanol suspension solvents achieved the most homogenous resuspension of the PLGA nanoparticles, so both were casted into modified thin film molds for membrane fabrication (**Figure 2.6B**). After allowing the solvents to evaporate, the nanoparticles suspended in ethanol formed an evenly spread powder in the film mold whereas the nanoparticles suspended in water formed a solidified crust that was stuck to the bottom of the mold indicating that they at least partially dissolved in the water (**Figure 2.6B**). This was not ideal for resuspension during the dissolved TSM biomaterial casting and thus the dried nanoparticles from ethanol resuspension were chosen to be initially casted with the dissolved TSM biomaterial. The resulting membranes had visibly distinct top and bottom faces suggesting that the nanoparticles were localized to the bottom nanofibrous layer and face (**Figure 2.6B**). This qualitative observation

provided high initial confidence that this newly designed method successfully embedded nanoparticles into the bottom nanofibrous layer of the TSM biomaterial membrane.

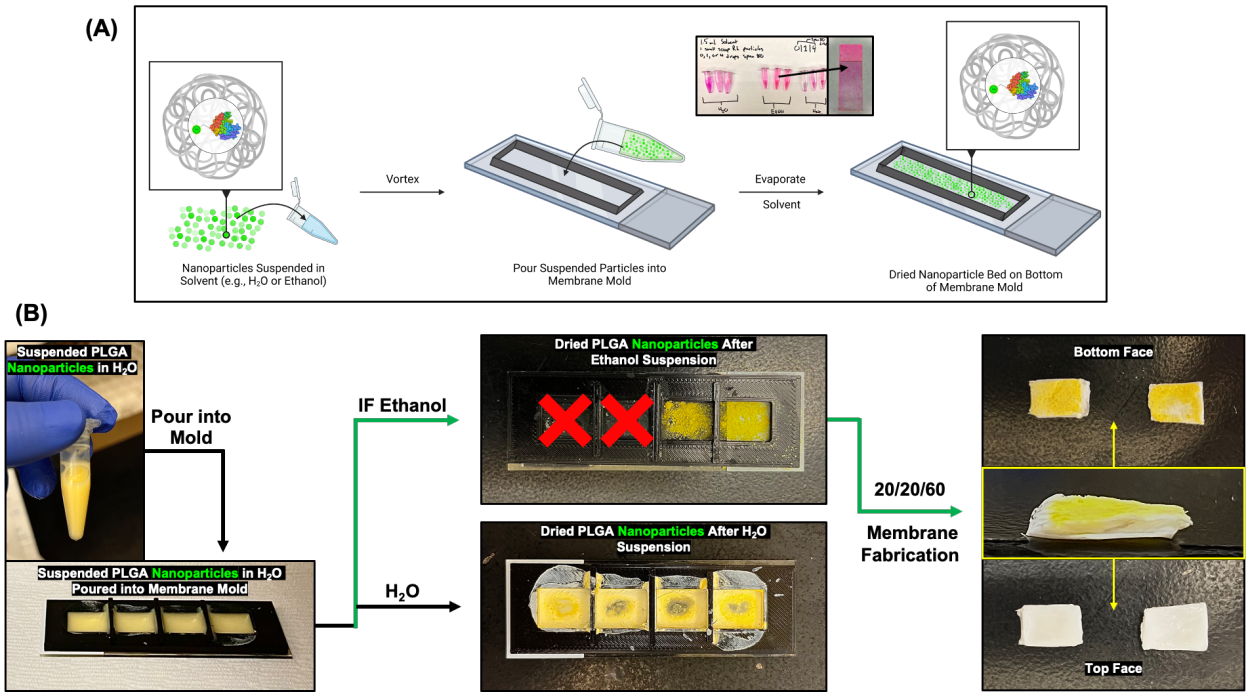

Figure 2.6: Nanoparticle resuspension and dispersion method for creating a thin bed of nanoparticles on the bottom of the film mold prior to membrane fabrication. This method allows nanoparticles to locally embed themselves within the bottom nanofibrous layer. (A) Visual schematic of the nanoparticle resuspension and dispersion procedure using PLGA nanoparticles encapsulating FITC-BSA as an example. Note that the photograph above the second arrow depicts the solvent optimization for resuspending PLGA nanoparticles encapsulating rhodamine b, where the ethanol solvent led to the most homogeneous resuspension and dispersion onto a glass slide. (B) Experimental photographs following the procedure of resuspending nanoparticles in water or ethanol and their resulting dispersions into a membrane mold after allowing the solvent to evaporate. The ethanol solvent left a better nanoparticle dispersion and thus TSM biomaterial membranes composed of 20% PLGA-DA, 20% PCL-DA, and 60% PLLA were fabricated on this membrane mold. The pictures of these fabricated membranes show that only the bottom nanofibrous side is colored, indicating that the PLGA nanoparticles encapsulating FITC-BSA are localized in this region.

Additional membranes were made by this method using the PLGA nanoparticles encapsulating rhodamine b. These films were cross-sectioned and analyzed by confocal microscopy to observe the nanoparticle distribution through the thickness of the membrane (**Figure 2.7B**). The confocal

microscopy of the cross-sections revealed that the nanoparticles were present throughout most of the membrane except for the top layer. The bottom faces of these membranes were additionally imaged with confocal microscopy and z-stacked (**Figure 2.7C,D**). There was fluorescent signal emitted from all regions of the bottom face, indicating that the nanoparticles were omnipresent in the bottom nanofibrous layer. Furthermore, the fluorescent signal intensity was spatially-consistent in the bottom face, indicating that the nanoparticles and fluorescent model-therapeutics (i.e., FITC-BSA and rhodamine b) were approximately homogenously distributed. This validated the ethanol resuspension method at distributing the nanoparticles evenly across the bottom of the film mold. Additionally, a z-stack of the confocal microscopy images of the bottom face revealed that the nanoparticles were penetrating into the bottom nanofibrous layer of the membrane, supporting the confocal microscopy image data from the cross-sections. Ultimately, these data suggested that this new, optimized method for installing a nanoparticle-based drug delivery system within a TSM biomaterial membrane had successfully embedded PLGA nanoparticles encapsulating model drugs in the nanofibrous bottom layer of the TSM biomaterial membrane, but not in the top smooth layer.

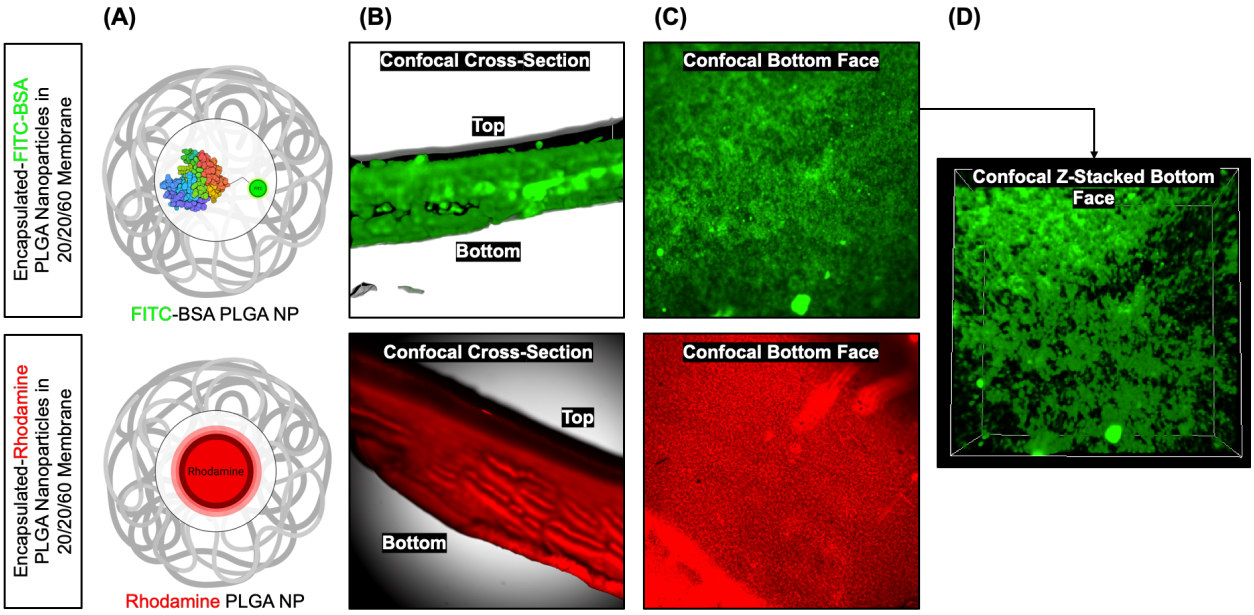

Figure 2.7: Characterization of nanoparticle distribution within the TSM biomaterial membranes using the ethanol solvent resuspension and dispersion method. (A) Visual depictions of the PLGA nanoparticles encapsulating FITC-BSA and rhodamine b, respectively, that were used in this experiment. (B) Confocal microscopy images of the cross-sections of the fabricated TSM biomaterial membranes with embedded nanoparticles encapsulating fluorescent molecules (i.e., FITC-BSA or rhodamine b) visualized with a 495 nm excitation laser or a 546 nm excitation laser, respectively. (C) Confocal microscopy images of the bottom face of the fabricated membranes with embedded nanoparticles visualized with a 495 nm excitation laser or a 546 nm excitation laser, respectively. (D) Z-stacked image of the confocal microscopy frame used in the top image of (C).

It was still possible that the nanoparticles were surface coating the nanofibers rather than embedding within them or that the nanoparticles were disrupting the nanofibrous surface topology of the bottom layer. SEM morphology analysis was first performed on the bottom face of the two groups of nanoparticle drug delivery TSM biomaterial membranes and were to the bottom face of a control TSM biomaterial membrane (**Figure 8A-C**). Several nanoparticles were observable directly on the surface of the nanofibers, but many nanoparticles were partially exposed on the surface of the nanofibers and partially embedded within the nanofibers. In general, the nanofibers of the drug delivery membranes were visibly more textured and bumpier than the smooth

nanofibers of the control membrane as a consequence of this. This observation also suggests that additional nanoparticles were completely embedded within the nanofibers of the drug delivery membrane, causing the nanofibrous biomaterial to bulge outwards around the contour of the nanoparticle to create the observed notches on the nanofibers. The SEM morphology analysis of the bottom face surface topology ultimately supported the claim that the nanoparticles were being physically embedded into the nanofibers of the membrane while not disrupting nanofiber formation through TIPS in the bottom layer.

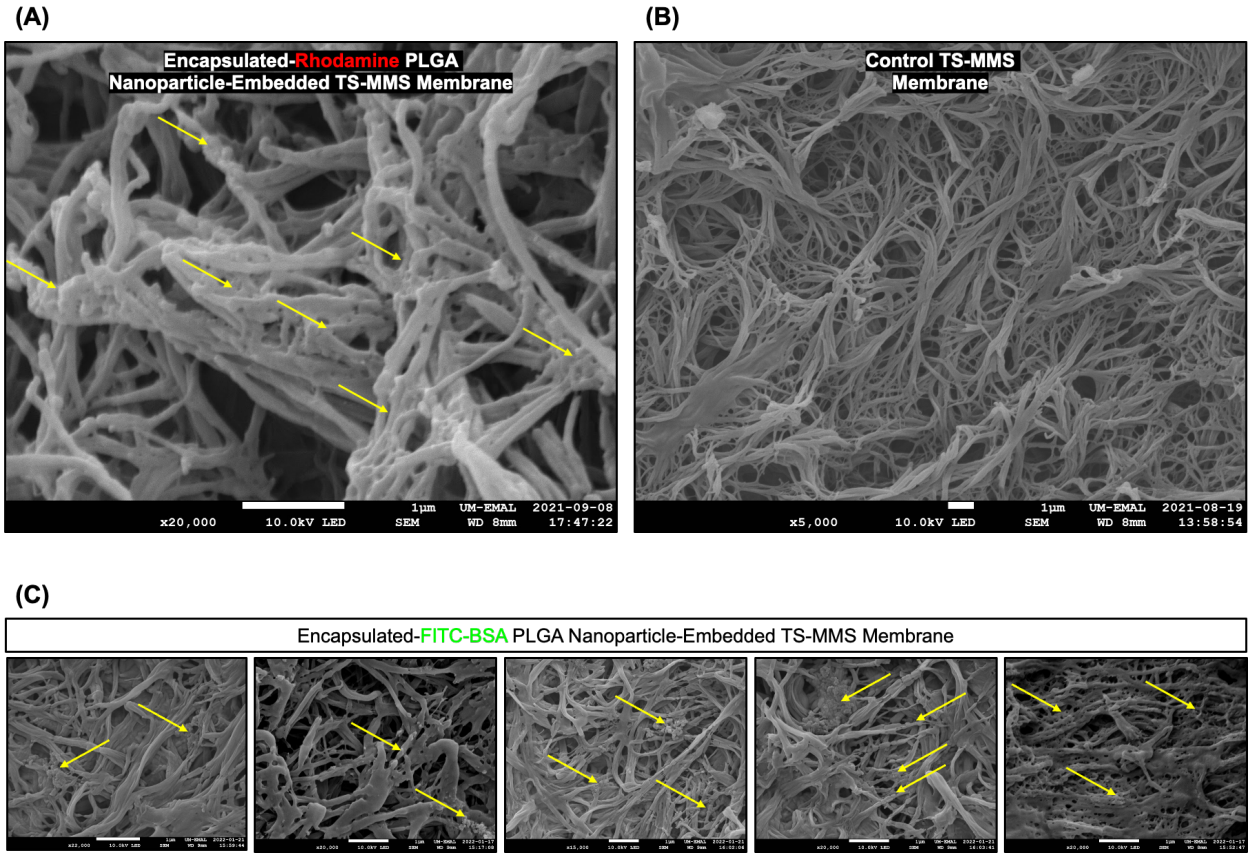

Figure 2.8: Nanofibrous bottom face surface topology characterization of membranes with embedded drug delivery systems and a control membrane. (A) Representative scanning electron microscopy image of the nanofibers for a TSM biomaterial membrane composed of 20% PLGA-DA, 20% PCL-DA, and 60% PLLA with an embedded nanoparticle drug delivery system for rhodamine b. The yellow arrows represent regions of irregular nanofiber surface topology resulting from embedded nanoparticles. (B) Representative scanning electron microscopy image of the nanofibers from a control TSM biomaterial membrane composed of 20% PLGA-DA, 20% PCL-

DA, and 60% PLLA with no embedded drug delivery. (C)) Representative scanning electron microscopy images of the nanofibers for a TSM biomaterial membrane composed of 20% PLGA-DA, 20% PCL-DA, and 60% PLLA with an embedded nanoparticle drug delivery system for FITC-BSA. The yellow arrows represent regions of irregular nanofiber surface topology resulting from embedded nanoparticles.

Additional SEM morphology analysis was performed on the top face of the drug delivery membrane containing PLGA nanoparticles encapsulating FITC-BSA for comparison to the bottom nanofibrous face with the confirmed nanofiber-embedded nanoparticles (**Figure 2.9**). The top face surface topology was still smooth and appeared to be unaffected by the drug delivery incorporation. It should be noted that a few small regions of the top face had bumpy surface textures resembling the outline of nanoparticles, but similar uneven surface textures were also occasionally present in the control TSM biomaterial membrane top face (**Figure 2.2B**). Thus, it was inconclusive if these bumpy surface regions were indeed nanoparticles or not, but the minimal presence of these textured regions coupled with the cross-section confocal analysis in **Figure 2.7B** suggested that the top layer was largely absent of nanoparticles.

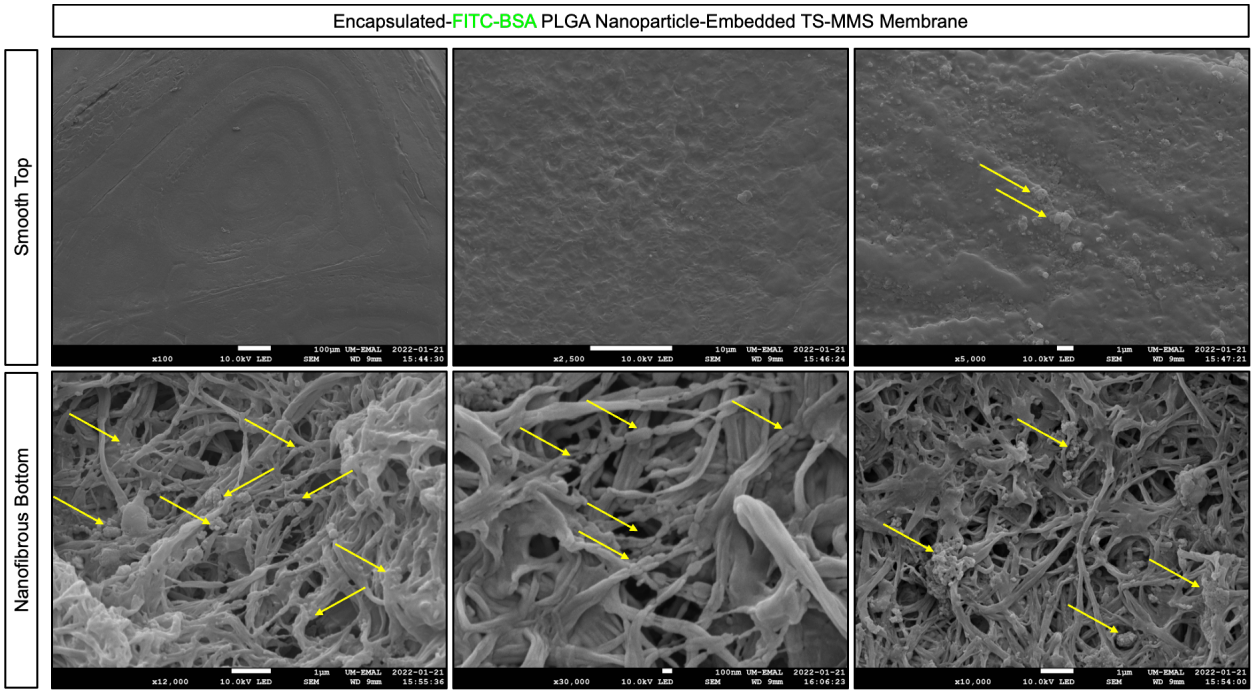

Figure 2.9: Top and bottom face surface topology characterization for TSM biomaterial

membranes composed of 20% PLGA-DA, 20% PCL-DA, and 60% PLLA with an embedded PLGA nanoparticle drug delivery system for FITC-BSA. Representative scanning electron microscopy images of the smooth top face reveal it to still be smooth, with two small regions possibly containing nanoparticles (yellow arrows). Representative scanning electron microscopy images of the bottom nanofibrous face reveal the nanofibers to have bumpy surface textures and notches corresponding to exposed and embedded nanoparticles (yellow arrows).

Ultimately, these experiments provided high confidence that a nanoparticle drug delivery was successfully installed into the TSM biomaterial membrane using the nanoparticle resuspension and dispersion method with ethanol to create a thin nanoparticle bed in the film mold prior to TSM biomaterial casting. Moreover, these experiments demonstrated that the nanoparticles were mostly localized to the nanofibrous bottom layer of the membrane, and were mostly absent from the top smooth layer. Finally, these experiments displayed a reasonably homogenous distribution of nanoparticles across the bottom nanofibrous layer and face, physically embedded into the nanofibers of TSM biomaterial membrane. This provided a potential mechanism of sustained, unidirectional therapeutic drug delivery from the TSM biomaterial membrane through the gradual hydrolysis of the nanofibers during the first stage of biphasic hydrolytic degradation.

The release kinetics of the drug delivery system sought to be investigated to quantify the duration of drug release and the dosing kinetics. To this end, 20/20/60 TSM biomaterial films were fabricated with an embedded drug delivery system installed by resuspending 15 mg of PLGA nanoparticles, encapsulating FITC-BSA at a concentration of 14.6 μg of FITC-BSA per mg of nanoparticles, in water or ethanol for dispersion in a film mold to create a thin nanoparticle bed for TSM biomaterial casting. The 20/20/60 TSM biomaterial was used because of its optimal balance between hydrophilicity and thermosensitive properties such that it maintained all the desirable properties of the optimized TSM biomaterial while having the capacity to hydrolyze faster for higher dose release kinetics. Additionally, the water and ethanol nanoparticle

resuspension methods were both used to quantitatively determine with a release test if there was a difference between how many nanoparticles were being embedded into the membranes by each method. Finally, FITC-BSA nanoparticles were utilized because their released concentrations could be precisely and accurately quantified with fluorometric and photometric methods to approximate the hypothetical dosing kinetics of PDGF.

A release test was performed for four separate membranes in each group (i.e., water particle resuspension/dispersion and ethanol particle resuspension/dispersion). Briefly, the release test consisted of suspending each individual membrane in 700 µL of phosphate buffered saline (PBS) in separate wells of a 48-well plate. The plate was allowed to orbit on an orbital shaker set to 45-60 rpm in a 37C incubation oven to simulate membrane hydrolytic release kinetics at physiological temperature. The entire PBS supernatant was collected at every sampling point and frozen at -80C before the wells were refilled with PBS. After 42 days, the experiment was terminated and the collected samples were thawed and quantified for their concentration by two absorption methods using a Nanodrop® 2000 spectrophotometer and an empirically-created FITC-BSA calibration curve.

The mean µg of FITC-BSA released by each group at each time was quantified alongside the standard deviation error. These means were cumulatively summed at each time point with the propagated standard deviation error to create a measure of the total FITC-BSA released at each time point, which constituted the final release kinetics of the membranes (**Figure 2.10A,B**). The release kinetics of FITC-BSA were observed to be approximately linear for both groups of membranes during the 42-day experiment. Furthermore, there was sustained release over the entire duration of the experiment, even on the last day of sample collection, suggesting that the membranes could keep releasing FITC-BSA beyond 42 days. These results also demonstrated that

the TSM biomaterial membranes with drug delivery had well-controlled dosing over a biologically significant time period. The dose of FITC-BSA released per day was on the one-microgram scale for both membranes, with the ethanol particle dispersion group exhibiting a slightly higher average release (**Figure 2.10B**). This implied that the ethanol solvent was superior to the water solvent at resuspending and dispersing nanoparticles on the film mold because more nanoparticles were in the membrane contributing to a higher dose release of FITC-BSA. Thus, all future experiments used ethanol over water for dispersing nanoparticles onto the film molds.

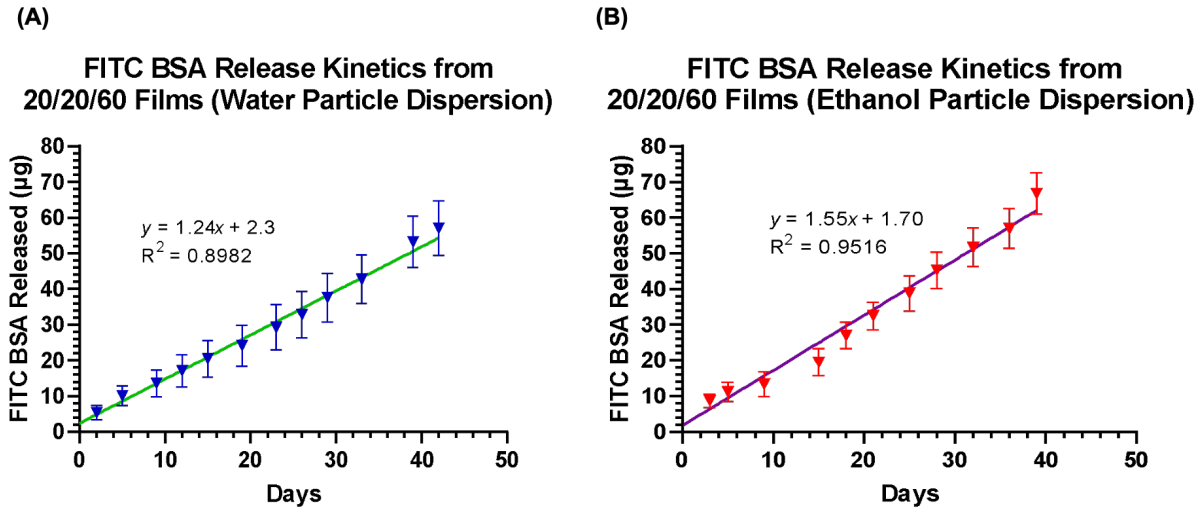

Figure 2.10: FITC-BSA release kinetics from TSM biomaterial thin films composed of 20% PLGA-DA, 20% PCL-DA, and 60% PLLA with embedded PLGA nanoparticle drug delivery systems installed via the solvent resuspension and dispersion method into the film molds using (A) water as a solvent and (B) ethanol as a solvent. Each point is the cumulative mean FITC-BSA released at that time point with error bars representing the propagated standard deviation. The linear regressions for the lines of best fit are plotted on each graph along with their corresponding equations and R-squared values. Theoretically, there are 15 mg of PLGA nanoparticles containing 14.6 µg of FITC-BSA per mg in each membrane.

These data were successful preliminary results to suggest that the TSM biomaterial membranes with embedded nanoparticles were sustainably releasing the model FITC-BSA protein therapeutic, implying that the same could occur for PDGF at roughly the same dose, given the same fabrication conditions. However, it was still unclear whether the release was unidirectional or if the

composition of the TSM biomaterial membrane mattered. These questions were addressed by preparing two release test experiments using 0/40/60 TSM biomaterial membranes and 20/20/60 TSM biomaterial membranes, each containing nanoparticle drug delivery systems fabricated from 15 mg of PLGA nanoparticles containing rhodamine b at a concentration of 60 μg per mg of nanoparticles. The first release test compared the free-floating membrane release kinetics of the 0/40/60 TSM biomaterial membranes and 20/20/60 TSM biomaterial membranes (**Figure 2.11B**). Quantification of this release was done by fluorescence spectroscopy using a plate reader. The 20/20/60 TSM biomaterial membrane was measured to release rhodamine b faster than the 0/40/60 membrane as given by the slope of the release kinetics for each group. This confirmed that the 20/20/60 film was hydrolyzing at a more rapid rate and therefore releasing rhodamine b at a higher dose due to the hydrophilic PLGA incorporation, as hypothesized. Once this result was apparent, the release test experiment for the 0/40/60 membrane group was truncated since it was irrelevant to the second experiment.

The second release test experiment investigated the question of unidirectional release in the 20/20/60 TSM biomaterial membrane because it was the optimal combination for combining high release kinetics and faster hydrolytic degradation with thermosensitive clinical-handling properties and the favorable biphasic morphology. The free floating 20/20/60 TSM biomaterial membranes in the prior experiment served as the control group in this experiment as other 20/20/60 TSM biomaterial membranes were divided into two groups and isolated to expose only one layer (i.e., smooth top or nanofibrous bottom) to the aqueous surroundings (**Figure 2.11A**). The layer isolation was performed by gluing the other face down into a 3D-printed mold, and filling the mold with glue until the face-down layer was completely submerged. This left only the face-up layer exposed to the aqueous environment, which would be subjected to hydrolyze under physiological

temperature. This release test experiment was allowed to proceed for 81 days with n = 6 membranes in each group. The fluorescent intensities were measured at the wavelength for rhodamine b excitation and the cumulative fluorescent intensity corresponding to the rhodamine b release was plotted for the control group, nanofibrous side-up group, and smooth side-up group (**Figure 2.11C**). The free-floating control membranes and nanofiber exposed membranes had no statistical difference in their cumulative release profiles and were both observed to be approximately linear. On the contrary, the smooth exposed layer was not measured to have any significant release over the entire duration of the experiment until a small trend of release toward the last ten days. These results demonstrated that the release was highly unidirectional due to the increased hydrophilicity and hydrolytic degradation rate of the nanofibers, which released the nanoparticles and therapeutics much more rapidly than the smooth layer. Additionally, it agrees previous experiments concluding that the nanoparticles are localized to the bottom nanofibrous layer of the membrane.

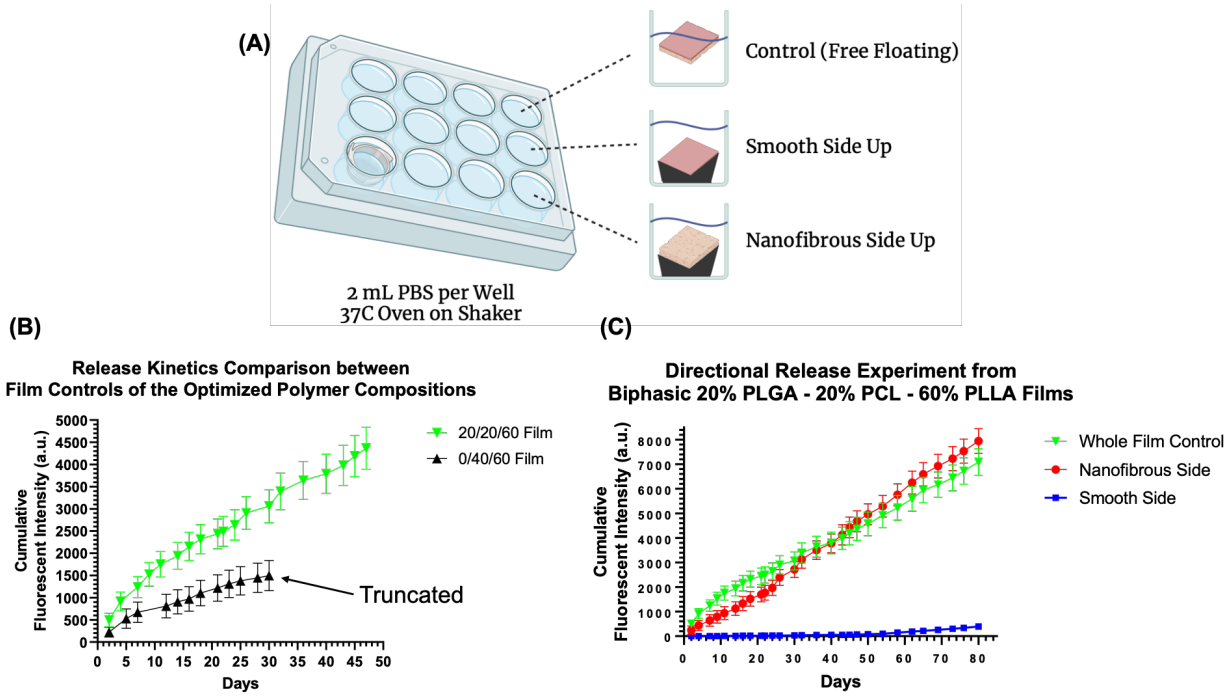

Figure 2.11: Release test experiments of rhodamine b from membranes with embedded nanoparticle drug delivery systems to evaluate unidirectional release and the rate of release between different membrane polymer compositions. (A) Schematic of the unidirectional release test experiment setup. The top smooth side or nanofibrous bottom side was glued down in a 3D-printed mold and the molds were glued into the wells of an assay plate. A control group was allowed to free-float in phosphate-buffered saline. (B) Plotted cumulative mean fluorescent intensities at each measurement time point for TSM biomaterial membranes composed of 20% PLGA-DA, 20% PCL-DA, and 60% PLLA (20/20/60) and TSM biomaterial membranes composed of 40% PCL-DA and 60% PLLA (0/40/60). Error bars represented the propagated standard deviation for each cumulative measurement. (C) Plotted cumulative mean fluorescent intensities at each measurement time point for the unidirectional release experiment depicted in (A) using TSM biomaterial membranes composed of 20% PLGA-DA, 20% PCL-DA, and 60% PLLA. The nanofibrous side represents the nanofibrous side-up and the smooth side represents the smooth side-up groups. Error bars represented the propagated standard deviation for each cumulative measurement. Theoretically, 15 mg of PLGA nanoparticles were loaded into each individual membrane at 60 μg of rhodamine b per mg of nanoparticles.

This experiment also measured directional and linear dose release for 81 days, which is a significant advancement in sustained drug delivery. The experiment was truncated at 81 days when the release still appeared to be increasing at a linear rate, suggesting the membranes could keep delivering small molecules at a linear rate beyond this time point. The exposed smooth side group was measured to have a minor increase in release at the end of the experiment, likely because the smooth top layer was beginning to hydrolyze completely in certain regions to expose the nanofibers underneath containing the nanoparticles (**Figure 2.12A**). Morphology analysis was performed on these membranes after they were allowed to hydrolyze for an additional three days in PBS to investigate if the biphasic degradation could confidentially explain the unidirectional drug release. Indeed, the SEM morphology analysis of the top faces of the smooth layer exposed membranes revealed only subtle hydrolytic degradation with a few porous regions and microtears forming which exposed a microporous surface underneath (**Figure 2.12A**). The lack of hydrolytic degradation in the smooth layer and its impermeable surface prevented the nanoparticles and therapeutics from escaping the TSM biomaterial that they are embedded into, thus proving the

importance of membrane degradation for dictating the release of therapeutics using this drug delivery system approach.

On the contrary, the bottom layer of the nanofiber exposed group revealed significant hydrolytic degradation of the nanofibers, often to the point where the nanofibers were nearly unrecognizable (**Figure 2.12B**). The bottom layer had degraded almost completely up to the border between the biphasic morphology, as the exposed smooth layer was observable in some SEM images. This confirmed that the embedded nanoparticles were being released from the membranes through the gradual hydrolytic degradation of the membrane. Because the nanofibrous bottom layer hydrolytically degraded much more on an 81-day time scale than the smooth top layer, the nanoparticles and rhodamine b consequently released from this side of the exposed membrane.

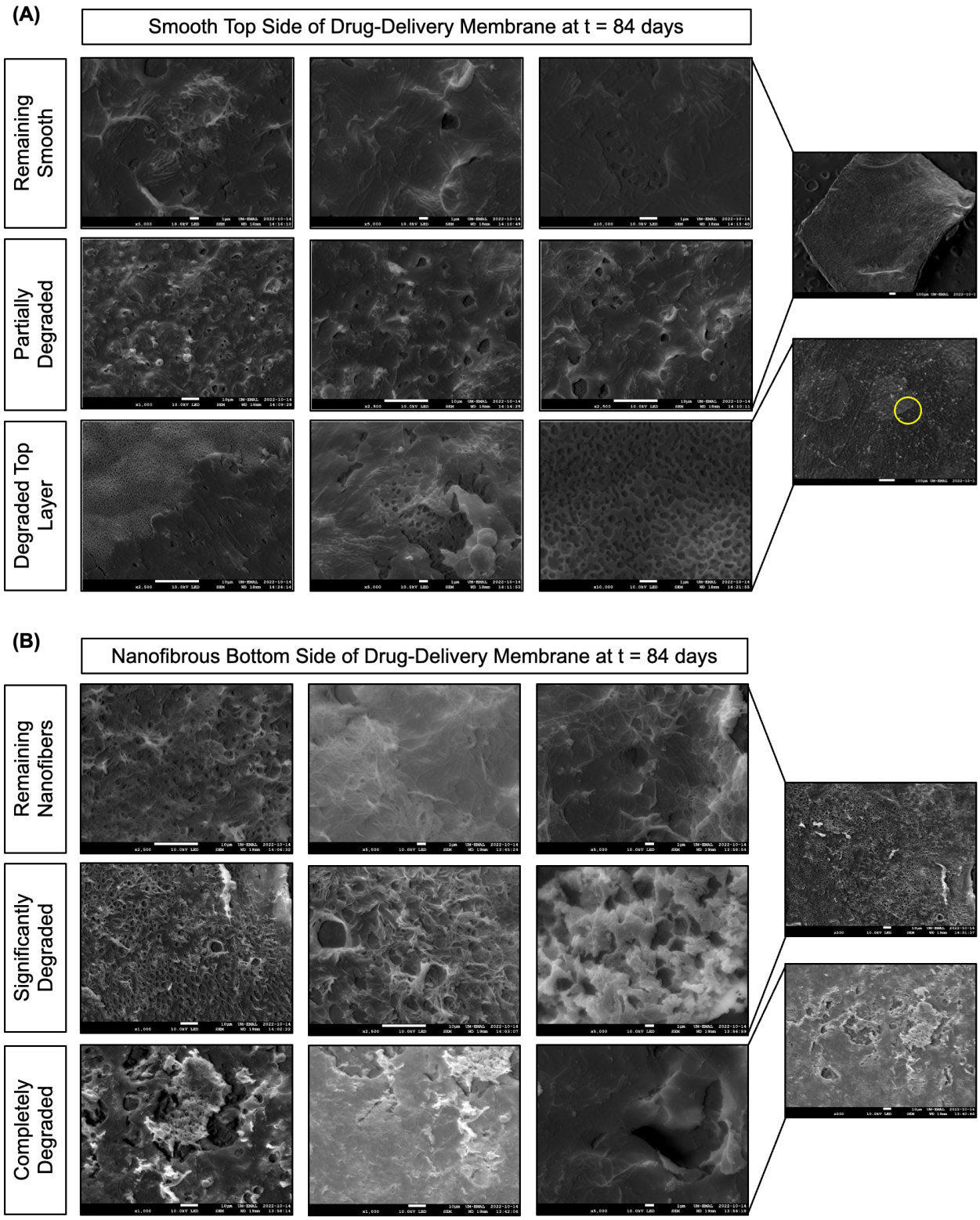

Figure 2.12: Degraded surface topology analyses of the control free-floating TSM biomaterial membranes composed of 20% PLGA-Da, 20% PCL-DA, and 60% PLLA from the unidirectional release experiment in **Figure 2.11**. These membranes were allowed to remain in PBS an additional

three days after their last release measurement such that their total time in PBS at 37C was 84 days. (A) Representative scanning electron microscopy images of the top face of the membranes portraying different regions and degrees of hydrolytic degradation. Overall, the smooth top face was not significantly hydrolyzed. (B) Representative scanning electron microscopy images of the bottom face of the membranes portraying different regions and degrees of hydrolytic degradation. Overall, the nanofibrous bottom face was significantly hydrolyzed and the nanofibers were almost completely gone.

2.3.3 Periodontal Regeneration Application

The TSM biomaterial membrane with drug delivery presented many favorable properties that would allow it to command the physicochemical microenvironment toward periodontal regeneration. Thus, it was to be evaluated for its regenerative efficacy *in-vivo* using a previously demonstrated periodontal defect model for rats. Briefly, the model consisted of drilling a periodontal defect into the molars of an anesthetized rat to create a significant distance between the alveolar bone crest and the cementoenamel junction (CEJ) prior to suturing the defect closed (**Figure 2.13A**). This is an effective model because the bone in this defect will not regenerate on its own and the defect will be replaced with epithelial tissue at best if there is no intervention.[5,22] Prior to implanting the TSM biomaterial membranes, a sham surgery was performed to practice creating the defect and to refine the surgeon's drilling technique. Micro-computed tomography (μCT) was performed on the sham defect rats two weeks after surgery to ensure that the proper periodontal defect was drilled into the molar of the rat (**Figure 2.13B,C**). Two-dimension slices and a three-dimensional reconstruction of the sham rat jawbones revealed that a significant bone defect was established in the periodontal tissue by the molars, given by the distance large between the bone crest and the CEJ. This established confidence with the surgical procedure in forming the periodontal defect model, allowing for the *in-vivo* experiments to proceed.

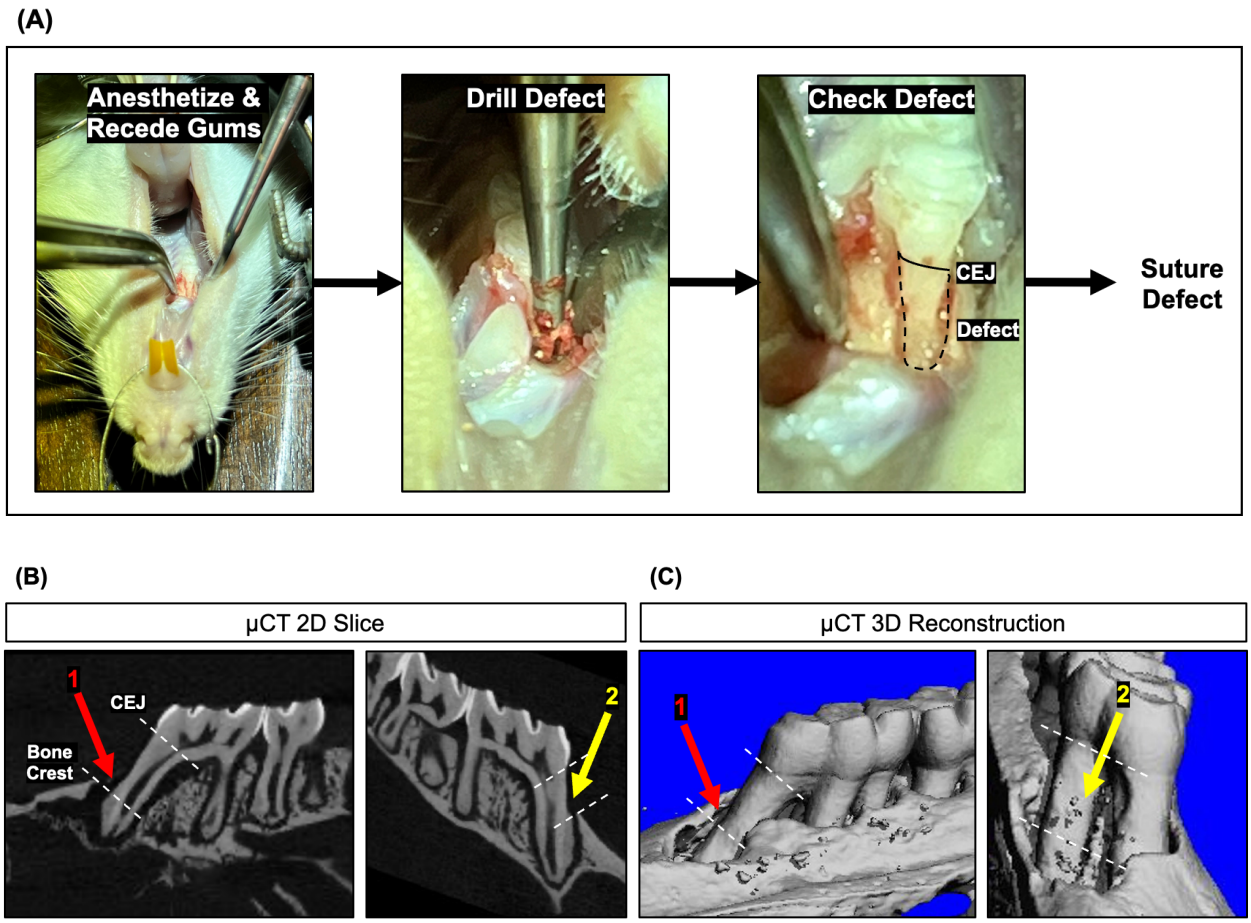

Figure 2.13: Periodontal defect surgery and validating the defect model. (A) Photographs from the surgery showing the steps of creating the periodontal defect, the outline of the defect, and the cementoenamel junction. (B) Representative micro-computed tomography 2D image slices with the bone crests and cementoenamel junctions labeled as the dashed white lines. The defects from two separate rats are identified with the red and yellow arrows. (C) The corresponding micro-computed tomography 3D reconstructions from the two rats in (B) with the bone crests and cementoenamel junctions labeled as the dashed white lines.

A healthy group of rats did not undergo surgery and were preserved for the time point durations of the *in-vivo* experiments to serve as a control group for comparison. The rest of the rats underwent surgery where they had periodontal defects drilled into both molars based on the optimized procedure from **2.13A**. These rats either received no treatment and were a sham group that was immediately sutured up for recovery, or they received an implanted membrane treatment. Rats receiving an implanted membrane treatment received either an optimized 20/20/60 TSM

biomaterial membrane (TSM), an optimized 20/20/60 TSM biomaterial membrane with an embedded nanoparticle drug delivery system encapsulating PDGF at 10 µg of PDGF per mg of nanoparticles dosed to release 125 ng of PDGF per day (TSM + PDGF), or an FDA-approved commercial periodontal membrane (GuideOR) (**Figure 2.14A**). It should be noted that the TSM biomaterial membranes were implanted with the nanofibers facing down into the defect. The rats were sutured up and allowed to recover for either four or eight weeks. The GuideOR treatment group only had an eight-week time point due its limited availability.

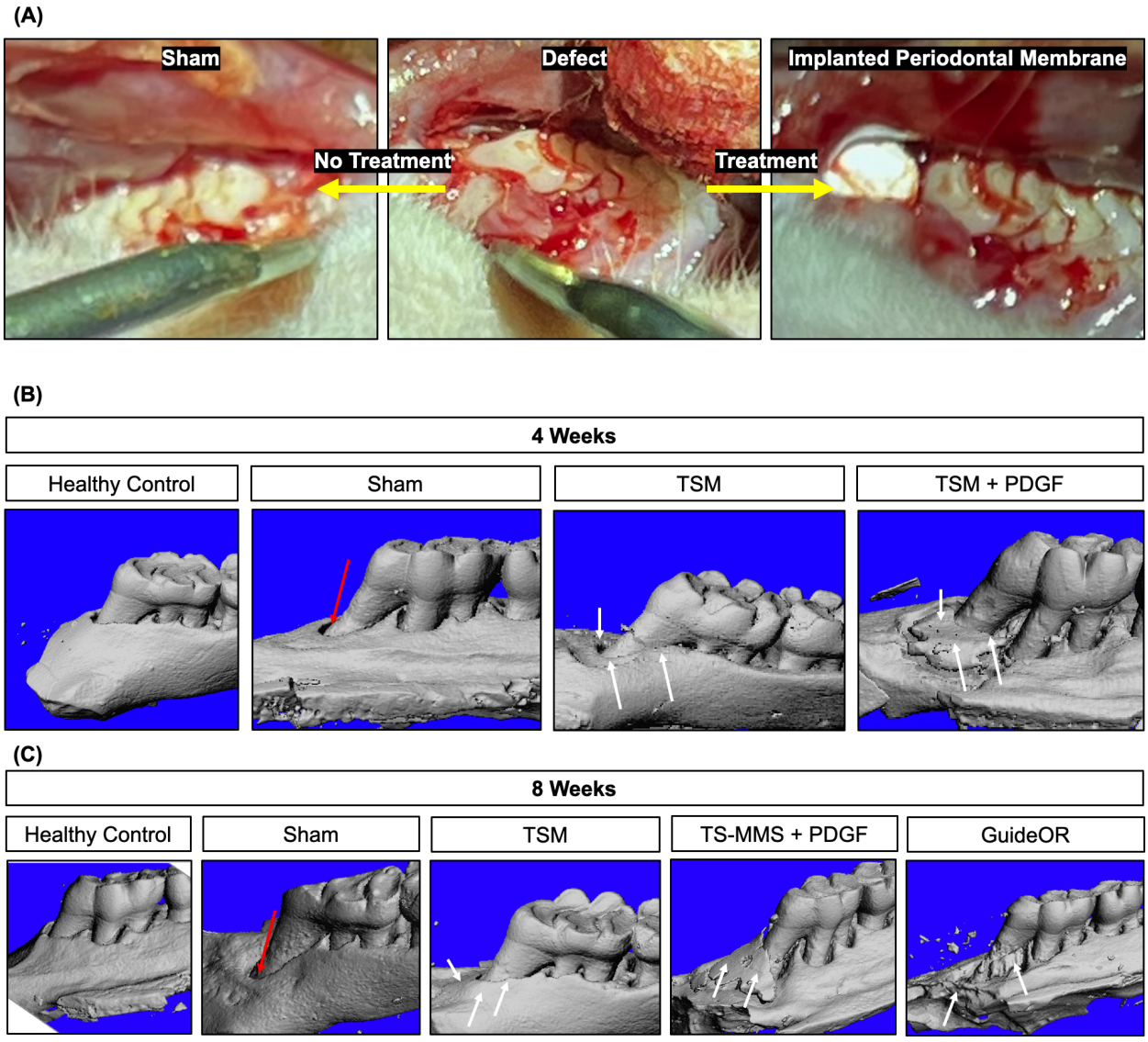

Figure 2.14: *In-vivo* experiments for the regeneration of periodontal tissue in the periodontal defect model demonstrated in **Figure 2.13**. All TSM biomaterial membranes care composed of 20% PLGA-DA, 20% PCL-DA, and 60% PLLA. (A) Photographs from the surgery of the established defect, which either received no treatment (left image) or received a tissue engineering membrane (right image). The tissue engineering membrane in the right image was a TSM biomaterial membrane. (B) Representative micro-computed tomography scans of the groups of rats euthanized after 4 weeks of recovery. The images are in the order of the healthy control group, the rats who received the surgery but no treatment (sham), the rats who received the TSM biomaterial membrane treatment (TSM), and the rats who received the TSM biomaterial treatment with an embedded nanoparticle drug delivery system encapsulating PDGF (TSM + PDGF). The white arrows point to regions of new bone formation while the red arrow points to the defect in the sham group. (C) Representative micro-computed tomography scans of the groups of rats euthanized after 8 weeks of recovery. The images are in the order of the healthy control group, the rats who received the surgery but no treatment (sham), the rats who received the TSM biomaterial membrane treatment (TSM), the rats who received the TSM biomaterial treatment with an embedded nanoparticle drug delivery system encapsulating PDGF (TSM + PDGF), and the rats that received a commercial, FDA-approved periodontal barrier membrane (GuideOR). The white arrows point to regions of new bone formation while the red arrow points to the defect in the sham group.

At their respective time points, the rats were euthanized and scanned by a μCT machine to develop 3D reconstructions of their jawbones and site of the periodontal defect. At four weeks the healthy control group, the sham, the TSM, and the TSM + PDGF groups of rats were compared by μCT (**Figure 2.14B**). The sham was observed to have no signs of bone regeneration or repair, as expected, while both the TSM and TSM + PDGF membranes produced mineralized bone formation in several regions within and around the periodontal defect. This was evident from their reduced distance between the bone crest the CEJ compared to the sham control, indicating that they had successfully regenerated mineralized bone at four weeks.

At eight weeks the healthy control group, the sham, the TSM, the TSM + PDGF, and the GuideOR groups of rats were compared by μCT (**Figure 2.14C**). Again, there was no sign of any bone regeneration in the sham group which demonstrated that the periodontal defect model was successful. The TSM and TSM + PDGF membranes both demonstrated remarkably more

mineralized bone formation than the GuideOR commercial membrane. Furthermore, the rats who received the TSM + PDGF membrane treatment showed nearly full vertical bone recovery as evident by the shortened distance between the CEJ and the bone crest. These results ultimately demonstrated that the TSM biomaterial membrane was capable of promoting periodontal tissue regeneration and bone mineralization due to its nanofibrous bottom layer being conducive to skeletal stem cell proliferation, migration, and differentiation. Furthermore, it was demonstrated that the TSM biomaterial membrane could successfully release protein therapeutics directly into the periodontal defect to further enhance regeneration significantly better than the commercial barrier periodontal membranes, which lack a balance between promoting regeneration and acting as a protective barrier.

2.4 Conclusion

The partial phase separation of PCL-DA and PLLA within a TSM biomaterial thin film construct in Chapter 1 resulted in a biphasic morphology that presented different potential functions and interactions with biological stem cells on either side of the thin film. The experiments of this chapter developed this unexpected result into a novel tissue engineering membrane and applied it to periodontal regeneration. The TSM biomaterial membrane demonstrates the favorable handling properties of a periodontal barrier membrane, as it possesses high sutureability and shapeability at clinically-feasible transition temperatures, but resists suture pull out at physiological temperature. Additionally, the TSM biomaterial membrane promotes bone mineralization and periodontal regeneration *in-vivo* at an efficacy exceeding a clinical-standard brand of commercial periodontal membranes.

Furthermore, a novel method was invented to embed PLGA nanoparticles encapsulating protein and small molecule therapeutics into the nanofibers of the TSM biomaterial membrane. These nanoparticles were shown to be localized in the bottom nanofibrous layer of the TSM biomaterial membrane and unidirectionally released at an approximately linear rate measured for up to 81 days. Small molecules and large protein macromolecules were able to be encapsulated into the nanoparticles and embedded into the membrane, proving it to be a versatile strategy. This drug delivery system was specifically used to deliver PDGF *in-vivo* directly into a periodontal defect, which significantly enhanced bone regeneration and mineralization in a critically-sized periodontal defect rat model.

Ultimately, this membrane technology presents advances over current periodontal membranes by facilitating tissue regeneration, sustained unidirectional therapeutic delivery, and protection from the oral cavity while also possessing convenient clinical-handling properties. Future investigations need to rigorously characterize the regenerated periodontal tissue to characterize its quality. Additionally, the membrane drug delivery *in-vivo* should be measured to further understand the dosing kinetics. Finally, optimal combinations of several therapeutics should be embedded into the membrane to achieve simultaneous delivery to further control and enhance tissue regeneration.

2.5 Materials and Methods

Materials and Reagents: Resomer 207S poly (L-lactic acid) was purchased from Evonik. All other reagents were purchased from Sigma Aldrich unless specifically mentioned in the below methods. Reagents were used as received unless otherwise specified.

Synthesis of Poly-ε-Caprolactone (PCL-diol): In the preparation of poly-ε-caprolactone (MW = ~10 kDa), 10 mL of ε-caprolactone monomer was added into a 50 mL round-bottom flask along with 89 µL of 1,4-butanediol (1 mol eq). Catalytic amounts (6.5 µL, 0.01 mol eq) of tin(II) 2-ethylhexanoate ($Sn(Oct)_2$) were added to a round-bottom flask with magnetic stir bar. The resulting solution was stirred at a low speed under vacuum, and heated to 120C and maintained for 12 hours resulting in a highly viscous solution. The reaction mixture was cooled to room temperature to form a white solid. A minimum volume of dichloromethane (DCM) was added to dissolve the white solid; the resulting solution was precipitated into 300 mL of methanol (~5x volume) at 0C yielding a white solid. This solution was then centrifuged (3,500 rpm x 10 min) to concentrate the solid and remove the supernatant. This precipitation procedure was repeated three times to remove unreacted monomer and catalyst. The solid, PCL-diol, was allowed to dry for two days in a vacuum chamber and stored at -20C before further use. Molecular weight was assessed by gel permeation chromatography (GPC) in tetrahydrofuran (THF) solvent. Molecular characterization is performed by nuclear magnetic resonance spectroscopy (NMR, CDCl3) and Fourier-transformed infrared spectroscopy (FTIR).

Synthesis of Poly-ε-Caprolactone Diacrylate (PCL-DA): PCL-diol was functionalized with terminal acrylate functional groups to impart cross-linking ability. 5 g of PCL (MWavg = 10.47 kDa by GPC) was added to a 50 mL round-bottom flask and dissolved in a minimum volume of anhydrous DCM. 135 µL of triethylamine (TEA, 2 mol eq) was added with stirring at moderate speed (~500 rpm). After 15 minutes, 78 µL of acryloyl chloride (AC) was added dropwise into the solution over the course of 10 minutes using a syringe. The reaction was left to proceed overnight under moderate stirring, warming to room temperature as the ice bath melted. The resulting

reaction mixture was precipitated into 300 mL of methanol (~5x vol) at 0C in a beaker to precipitate a white solid. This solution was then centrifuged (3,500 rpm x 10 min) to concentrate the solid and remove the supernatant. This precipitation procedure was repeated three times to remove unreacted AC and remove TEA. The solid PCL-DA was allowed to dry for two days in a vacuum chamber and stored at -20C before further use. End group functionalization was confirmed by NMR (CDCl3) and FTIR.

Synthesis of Poly Lactic-co-Glycolic Acid (PLGA): In the preparation of poly lactic-co-glycolic acid (50:50 lactide-glycolide ratio, MW ~ 10,000 Da), *L*-lactide (7.6 mmol, 1.10 g, 1 mol eq) and ε-caprolactone (7.6 mmol, 0.88 g, 1 mol eq) were added to a round-bottom flask with benzyl alcohol (initiator, 0.2 mmol, 208 μL, 0.027 mol eq). The reaction was heated 120C under vacuum with moderate stirring then 100 μL of $Sn(Oct)_2$ (catalyst, 0.001 mol eq) was injected. After twelve hours, the reaction was opened to air and allowed to cool to room temperature resulting in a colorless solid. A minimum volume of DCM (approximately 20-30 mL) was used to completely dissolve this solid, and the resulting solution was precipitated into 300 mL of -20C methanol (10x vol eq) resulting in a white solid. The supernatant was poured off and the PLGA was dried for two days in a vacuum chamber and stored at -20C before further use. This precipitation procedure was repeated three times. The solid PLGA was allowed to dry for two days in a vacuum chamber and stored at -20C before further use. Chemical identity and lactide-glycolide ratio was confirmed by NMR (CDCl3) and FTIR. Molecular weight was determined by GPC.

Synthesis of Poly Lactic-co-Glycolic Acid Diacrylate (PLGA-DA): PLGA was modified to obtain terminal acrylic functional groups for cross-linking. To synthesize poly lactide-co-glycolic

acid diacrylate (PLGA-DA), PLGA (0.50 mmol, 5 g, MW ~ 10,000 Da) was transferred into a round-bottom flask in an ice bath and dissolved in 30 mL DCM. TEA (1 mmol, 80.1 µL, 2 mol eq) was added the resulting solution was stirred at moderate speed on ice. After 15 minutes, acryloyl chloride (1 mmol, 140 µL, 2 mol eq) was injected dropwise into the solution. The reaction was allowed to proceed overnight under moderate stirring, slowly warming to room temperature in the melting-ice bath. After this time elapsed, the reaction was precipitated into 300 mL of methanol at 0C, resulting in a white PLGA-DA solid. This solution was centrifuged to concentrate the PLGA-DA solid such that the supernatant could be removed. This precipitation procedure was repeated three times. PLGA-DA solid was allowed to dry for two days in a vacuum chamber and stored at -20C before further use. End group functionalization was confirmed by NMR (CDCl3) and FTIR.

Film Template Design and Fabrication: TinkerCAD online software was used to design rectangular casting molds with an outline of 73 x 23 x 2 mm dimensions containing a central hollow rectangle of 60 x 10 x 2 mm dimensions for holding the polymer solution during casting and UV-induced crosslinking. An additional design was created for casting smaller films, which the same outline dimensions as the prior design, but partitioned the central hollow rectangle lengthwise into four 13 x 10 x 2 mm hollow sections, each walled off from the adjacent sections by a 1.5 x 10 x 4 mm solid barrier. All casting molds were 3D printed from PLLA using an Original Prusa i3 MK3S+ 3D Printer. The 3D printed mold outlines were glued to the charged side of ASi Supreme™ Plus Microscope Slides using Gorilla Glue Super Glue® and allowed to dry in a ventilated hood for two days prior to polymer casting.

Biphasic Film Fabrication: In general, film molds for polymer casting were placed in a FisherScientific® UV Crosslinking Chamber (λ = 256 nm) powered at E = 10 J. A 3 mM stock solution of Irgacure® 2959 photoinitiator was prepared in methanol and stored at -20C. Separately, a 10% w/v polymer solution in tetrahydrofuran (THF) was prepared from varying w/w/w ratios of PLGA-DA, PCL-DA, and PLLA, respectively. The polymer solution was heated to 62C in a convection oven for at least two hours or until the polymers were completely dissolved. Once the polymer solution was dissolved, it was removed from the convection oven to be immediately injected with the photoinitiator stock solution (3.33% v/v), and mixed before being rapidly transferred into the film molds (approximately 2 - 2.5 mL of solution per film mold) with a transfer pipette. Once the UV crosslinking chamber was shut the films were allowed to crosslink for five minutes, unless otherwise specified. After the time has elapsed, the film molds were removed from the UV crosslinking chamber and rapidly transferred onto flat slabs of dry ice to induce thermally induced phase separation (TIPS) of PLLA responsible for nanofiber formation. After 5-10 minutes, the films were transferred into a -80C freezer to continue TIPS, for 48 hours.

After 2 days at -80C, the films were removed from the freezer and placed into an ice bath. They soaked for approximately 3 hours while gradually warming to room temperature in the bath, turning bright white. Once at room temperature, the films were removed from the water and the polymer film construct was cut out of the film mold using a razor blade. The resulting films were dried flat for 4 days then stored at -20C until further use.

Mechanical Testing: Mechanical properties of thin films were measured using an MTS Synergie 200 mechanical tester (MTS Systems, Inc.). Tensile modulus was defined as the initial linear modulus on the resulting stress-strain curve, with a strain rate of 1.0 mm/minute. Thin films were

bathed in water heated to 37C or 80C for 5 minutes directly prior to making the measurement for a given film.

Encapsulated-Drug PLGA Nanoparticle Fabrication: Nanoparticles were prepared by a w/o/w double emulsion method with rhodamine b as a model small-molecule drug. Briefly, 15 mg of rhodamine b was dissolved in 500 µL (X mM) of distilled water (ddH_2O). Separately 250 mg of PLGA (50:50, MW = 7-17kDa, Sigma #) was dissolved in 1.50 mL of DCM (X mg/mL) in a 50 mL Falcon Tube. Both solutions were kept on ice once fully dissolved. 160 µL of the drug solution was added to the PLGA solution and sonicated by a probe sonicator for 35 s on ice to create a w/o emulsion (X kV power). Immediately after, the w/o solution was poured into 5 mL of 1% w/v polyvinyl alcohol in distilled water on ice and the resulting solution was sonicated by the probe sonicator for 35 s on ice, resulting in the w/o/w emulsion. The w/o/w emulsion was transferred into to a 20 mL glass vial, washing the Falcon Tube with distilled water (diH_2O) to maximize particle yield. The w/o/w emulsion was stirred at 1300 rpm overnight in a fume hood to allow for organic solvent evaporation. The nanoparticles were concentrated and washed of the PVA and excess drug by 6 rounds of centrifugation at 9000 rpm for 20 min at 5 C, each, refreshing diH_2O between rounds. Particles were reconstituted in ddH2O and lyophilized and stored at -20 C until further use.

Encapsulated-Protein PLGA Nanoparticle Fabrication: Nanoparticles were prepared by a w/o/w double emulsion method. Briefly, a specified-concentration protein solution (1% w/v FITC-BSA, 2 mg PDGF/mL) in PBS was prepared while 225 mg of commercial PLGA (50:50, MW = 7-17kDa or MW = 24-38kDa) was dissolved in 1.80 mL of DCM in a 50 mL Falcon Tube. Both

solutions were kept on ice once fully dissolved, then 320 µL of the protein solution was added to the PLGA solution and sonicated by a probe sonicator for 35 s on ice to create a w/o emulsion. Immediately after, 5 mL of 1% w/v polyvinyl alcohol in distilled water on ice (PVA) (MW = 89-98kDa) was poured into the Falcon Tube, and the resulting solution was sonicated by the probe sonicator for 35 s on ice, resulting in the w/o/w emulsion. The w/o/w emulsion was transferred into to a 20 mL glass vial, washing the Falcon Tube with distilled water (diH_2O) and pouring into the glass vial (approximately three washes with 2-2.5 mL of diH_2O) to maximize particle yield. The w/o/w emulsion was stirred at 1300 rpm overnight in a ventilated hood with the vial top open to allow for organic solvent evaporation. After this time elapsed, the nanoparticles were concentrated and washed of the PVA and unreacted reagents. This was accomplished by transferring the w/o/w solution into ultracentrifuge tubes and carrying out 6-7 rounds of ultracentrifugation at 9000 rpm for 20 min at 5 C, dumping the supernatant and refilling the tubes with diH_2O between rounds. After ultracentrifugation, the tubes containing the nanoparticle pellets were filled halfway with diH_2O, lyophilized for 2-4 days, and the resulting encapsulated nanoparticles were a fine grainy powder that was stored at -20 C until further use.

Biphasic Film Fabrication with Encapsulated Nanoparticles Fabrication: Membrane molds were 3D printed and glued to glass microscope slides. Slides were placed on a flat surface in a ventilated hood. The desired mass of fabricated nanoparticles (usually 15 mg) was loaded into a 1.5 mL Eppendorf® microtube, and suspended in 500 µL water or ethanol, aided by a vortex mixer. The solution was quickly transferred into the center of the film mold to coat the glass surface nanoparticles. The solvent was allowed to completely evaporate, leaving behind a nanoparticle-coated substrate in the film mold. Once this process was complete and the nanoparticle surface-

coated film molds were dry, the rest of the fabrication method was followed identically to that described above, starting from the first step.

Evaluation of Drug-Release Kinetics from Film: Films containing PLGA nanoparticles were cut into 13x10x2 mm rectangular cuboids. Each film slice was subject to physiologic conditions and allowed to slowly degrade, releasing fluorescent model drug into free solution, which was quantified using a plate reader. Membranes were then individually placed into the wells of a 48-well cell culture plate. Each well containing a film received 400 μL of PBS and maintained at 37 C on a microplate shaker set to approximately 110 rpm. At each time point, the plate was removed from the oven and PBS solution containing released drug was removed and stored at -80C for subsequent analysis. 400 μL of fresh PBS was added, then the plate was covered and placed back on the microplate shaker at 37 C. This process was repeated for the sample collection at every time point for the duration of the experiment. At the end of the experiment, all samples were thawed from the -80 C freezer and fluorescence measured in a 96 well plate using a plate reader (Thermo Scientific™ Varioskan™ LUX Multimode Microplate Reader, $\lambda_{excitation}$ = 546 nm, $\lambda_{emission}$ = 568 nm, bandwidth = 5 nm). These data were exported and analyzed in Prism.

Evaluation of Directional Drug-Release Kinetics from Membrane: Films containing PLGA nanoparticles were cut into 13x10x2 mm rectangular cuboids. Super glue was used to either cover the nanofibrous film side or the smooth film side to prevent its exposure and subsequent drug release, isolating the degradation and release to only the non-glued part of the film. Carefully, Gorilla® Super Glue was thickly painted onto the nanofibrous parts of the film slices, which included the bottom face and four lateral sides. Other samples received the same super glue

treatment, but only to the top, smooth face of the film. The final group of films served as the control as they were untreated with super glue, leaving all surfaces exposed, and placed individually into wells of a 48-well cell culture plate. The 48-well plate was placed in a ventilated hood for 48 hours to allow the super glue to dry. After this time elapsed, the experiment was carried out identically to the previous method for evaluating general drug-release kinetics from the films.

Sterilization of Biomaterial Constructs: Prior to all *in vitro* and *in vivo* work, PLLA scaffolds were sterilized by a dual-sterilization method. First, constructs were sterilized by ethylene oxide gas according to the manufacturer's protocol (Anpro). Secondly scaffolds were washed with 70% ethanol for 30 minutes, followed by washing with PBS then with cell culture media, immediately before cell seeding. The purpose of the ethanol wash is twofold – first, a secondary sterilization method, and second, to "wet" the surface of the hydrophobic PLLA scaffold prior to cell seeding.

UV-VIS Spectroscopy: Simvastatin was dissolved as describe and its absorbance was measured using a Hitatchi U-2910 spectrophotometer in a quartz cuvette. Concentration was determined using a standard curve.

Nuclear Magnetic Resonance (NMR) Spectroscopy: Synthesized polymers were characterized by nuclear magnetic resonance (NMR) spectroscopy to confirm their molecular identity and reaction efficiency. 1H spectra were recorded with a Varian MR400 spectrometer operating at 400 MHz and room temperature. Spectra were observed in deuterated chloroform ($CDCl_3$). Spectral analysis is carried out in VnmrJ (Version 4.2, Agilent) and MestReNova (Version 12.0.0-2000080, Metrelab Research).

Scanning Electron Microscopy: The surface morphology of all biomaterial constructs was observed by scanning electron microscopy (JEOL JSM-7800 FLM) with an accelerating voltage of 5 kV and working distance of 10-15 mm. Prior to observation, samples were coated with gold using a sputter coater (Desk II, Denton Vacuum Inc.).

Transmission Electron Microscopy: 5 μL of BSA-loaded nanoparticle suspension was deposited on a copper TEM grid, and negatively stained with 2% uranyl acetate. Observation was done at an accelerating voltage of 80 kV in a transmission electron microscope at the Michigan Center for Materials Characterization (MC^2, JEOL 3100R05).

Confocal Laser Microscopy: Fluorescently active probes were observed from substrates by confocal laser microscopy (Nikon Eclipse C1).

Statistical Methods: All data are reported as mean ± standard deviation and represent a minimum sample size of n>3. Statistical analysis was carried out in GraphPad Prism v8. Student's t-test was used to determine statistical significance of observed values between experimental groups where $p < 0.05$ was considered significant. Tukey's test was used to determine differences between group means as a single-step method to compare multiple means and determine statistical significance between. Statistical analyses were carried out under the guidance of the University of Michigan Consulting for Statistics, Computational and Analytical Research Center. In all graphics, significance is noted as: * $p<0.05$, ** $p<0.01$, ***$p<0.001$, ****$p<0.0001$.

Image Analysis: All image analysis was carried out in Fiji imaging software (Image J Image J, V 1.0.0-rc-69/1.52p). Images were imported as raw files (.TIF). Analyses were carried out using batch macros following optimized protocols.

Periodontal Defect Formation and Membrane Implantation Surgical Procedure: *In-vivo* functionality of TS-MMS membranes to facilitate periodontal regeneration was evaluated in a periodontal defect model in rats. Virgin male and female Sprague-Dawley rats (3 months old) were used for testing membranes *in-vivo* under an approved animal protocol. Animals were anesthetized by ketamine-xylazine and prepared with a preoperative scrub and prophylactic carprofen administration. A full thickness mucoperiosteal flap was elevated from a midcrestal incision to uncover alveolar bone adjacent to the maxillary first molars, under a microscope. A #2 carbide round bur and slow speed handpiece, with copious irrigation, was used to remove the alveolar bone covering the tooth's mesial root surface. After the defect was created (1.5 mm x 3 mm x 1 mm), a membrane was implanted into the defect location and in contact with the periosteum at the margins of the defect. The flap was repositioned and incision was closed with cyanoacrylate; animals were able to recover. After 4 and 8 weeks, rats were sacrificed and the recovered bone at the defect site is evaluated by microcomputed tomography analysis.

Micro-computed Tomography: Samples were harvested and fixed with 4% paraformaldehyde. The samples were placed in a 19 mm diameter specimen holder and scanned over their entire length using a micro-CT system (μCT100 Scanco Medical, Bassersdorf, Switzerland) with voxel size 10 μm, 70 kVp, 114 μA, 0.5 mm AL filter, and integration time 500 ms.

Chapter 3

Fabrication of a Nanofibrous Tissue Engineering Biomaterial Scaffold with Thermosensitive Macropore Shape Memory and Embedded Drug Delivery

3.1 Abstract

Macropores are a crucial structural component of biomaterial constructs that dictate host-integration, vasculature formation, cell migration and proliferation, cell differentiation, and other factors with respect to implanted biomaterial constructs like scaffolds. This chapter reports on the development of a novel thermosensitive, memorized-microstructure (TS-MMS) scaffold that was created by from the thermosensitive shape memory biomaterial introduced in chapter 1. The TS-MMS scaffold showed a homogenous, nanofibrous morphology with thermosensitive shaping and macropore shape memory. The scaffold was characterized for its physical and thermal properties to be optimized for its ability to be shaped to irregular defects and to recover its spherical macropores via thermal shape memory. Additionally, a nanofiber-embedded nanoparticle drug delivery system was incorporated into the TS-MMS scaffold using a newly designed sugar-particle adhesion method. The release from the drug delivery system was measured for up to 40 days but projected to extended as far out as 90 days. *In-vivo* experiments using TS-MMS scaffolds and TS-MMS scaffolds with simvastatin showed that the scaffolds promoted cell migration, adhesion, microvascular formation, and osteogenesis. The TS-MMS scaffolds with simvastatin release showed the most significant advances in these areas, resulting in highly mature tissue and extracellular matrix formation within those scaffolds.

3.2 Introduction

Macropores are one of the most important structural components of scaffolds because they influence cell behaviors such as differentiation and migration, allow for vasculature penetration, and they assist with host-integration.[10,12,13,15,20,21] However, macropores can be easily compromised in scaffolds during implantation procedures that require the scaffold to be fitted a clinical defect. Crushing these macropores prevents cells from migrating into the scaffold from the host and around the scaffold to regenerate heathy, new tissue. This is a problem that has perplexed the field of biomaterials and tissue engineering but has not resulted in much progression or any solutions. [12,20,21]

Instead, many biomaterial scaffolds are implanted into pre-made defects that do not require scaffold manipulation or fitting to the defect.[10,12,13,15,20,21] Rather, the defect is created to fit the scaffold for *in-vivo* experimentation. This is not clinically realistic, as real clinical defects come in many shapes and sizes, which require a biomaterial that can be contoured to fit that defect by the clinician. Thus, the aim of this project was to develop the thermosensitive shape memory biomaterial from chapter 1 into a three-dimensional (3D) macroporous scaffold construct exhibiting nanofibers induced by TIPS and thermosensitive properties for advanced clinical shaping and macropore recovery.

Additionally, there is highly limited research on drug delivery systems within scaffold constructs. However, combining the strong mechanobiology cues that the scaffolds provide to stem cells with sustained, chemical signals could further enhance regenerative outcomes and offer higher predictability over tissue engineering. Therefore, the other overarching aim of the project presented in this chapter was to design a novel method to embed a drug delivery system within the biomaterial of a scaffold for sustained therapeutic release, similar to chapter 2.

3.3 Results

3.3.1 Scaffold Characterization and Macropore Shape Memory

Clinically-relevant skeletal tissue defects come in many unpredictable shapes and sizes (**Figure 3.1**). Thus, it is important for any suitable biomaterial construct for skeletal regeneration to be shapeable on-demand to unpredictable, irregular defects without compromising the advantageous properties of the biomaterial construct for tissue regeneration. Macroporosity is a paramount property to control in a biomaterial scaffold because it influences how skeletal stem cells from the host integrate, migrate, and differentiate within the scaffold to regenerate bone tissue.[10,12,13,15,20,21] However, this is one of the easiest properties to be lost or damaged during clinical implantation because compressing and shaping the scaffold to a defect will compress and misshape the macropores (**Figure 3.1**). Thus, the goal of this research was to fabricate a macroporous scaffold that could memorize and recover its porous microstructure after implantation upon receiving a thermal stimulus (**Figure 3.1**).

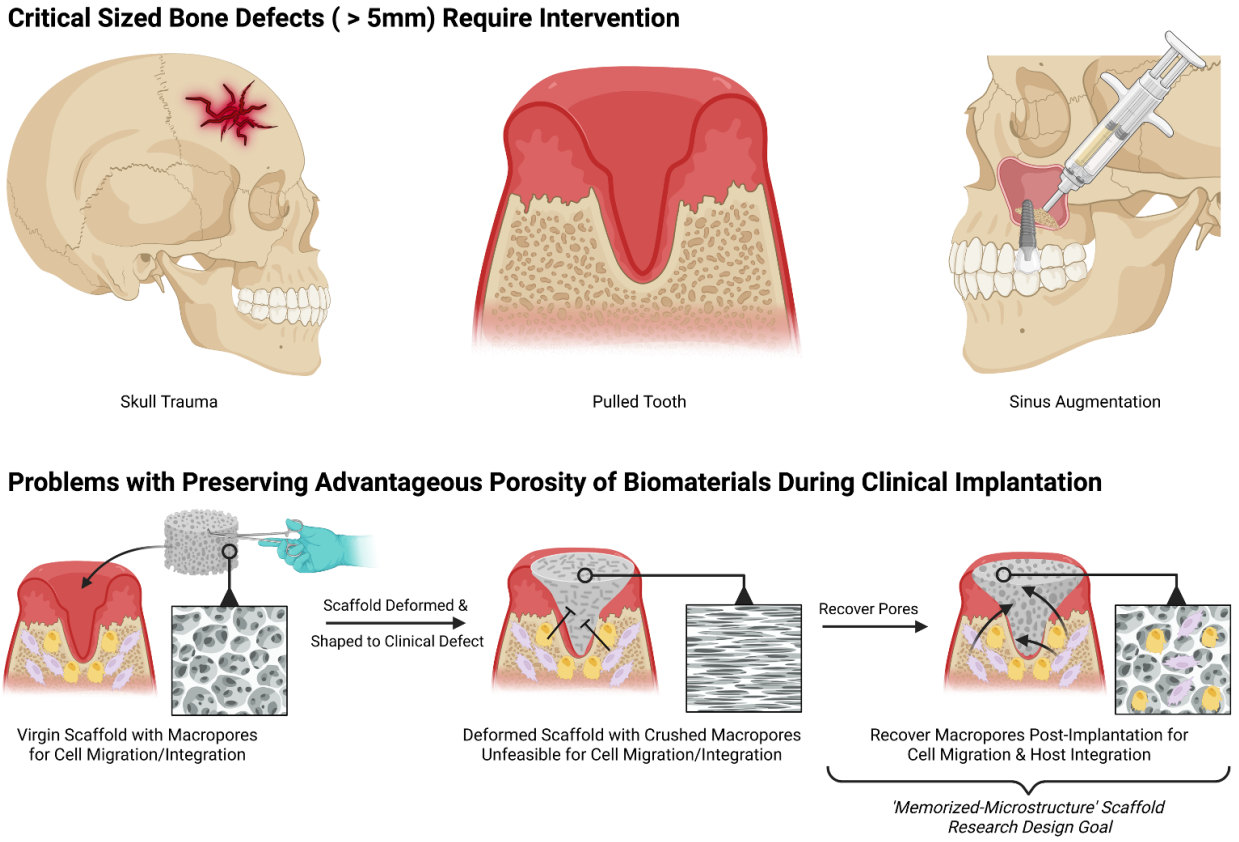

Figure 3.1: Visual schematic depicting examples of critically sized craniofacial bone defects that require regeneration and the problem with current biomaterials and scaffolds losing their porosity during implantation along with the research goal to recover these macropores *in-vivo*.

Additionally, it was desirable to impart a nanofibrous surface topology into this biomaterial scaffold due to the relevance of nanofibers in tissue engineering and regeneration. Moreover, a biomaterial exhibiting a nanofibrous surface topology with shape-memory has not been fabricated to date, especially in a macroporous scaffold construct. It was hypothesized that the TSM biomaterial from chapter 1 could satisfy these requirements in a three-dimensional macroporous scaffold since it exhibits a nanofibrous surface topology induced by TIPS and is capable of TSM at clinically-relevant temperatures (i.e., T > 50C).

Specifically, it was hypothesized that crosslinking the TSM biomaterial around the scaffold macropores would memorize the microstructure of the scaffold, which could be recovered by

TSM. Hence, this scaffold was designed to have a thermosensitive, memorized microstructure (TS-MMS) of the macropores using the TSM biomaterial and a modified fabrication technique, based on the fabrication of macroporous, nanofibrous PLLA scaffolds,[20,21] that additionally accounts for photocrosslinking and purification. The optimized procedure is detailed in **Figure 3.2**. It is noteworthy to mention that the sugar porogen-leaching method is a widely used in scaffold fabrication because it allows for the size of the pores to be highly controlled, and that it ultimately leads to an annealed, dried sugar-sphere template that can be casted by any dissolved biomaterial polymer. The TS-MMS scaffold biomaterial is irradiated and crosslinked around these sugar spheres after it is casted to memorize the microstructure of the scaffolds (i.e., macropores). The TS-MMS scaffolds are then held at -80C for at least 48 hours to induce nanofiber formation through TIPS. Finally, the TS-MMS scaffolds are purified in hexanes to dissolve unreacted monomers and photoinitator before their sugar-sphere template is leached in water to leave behind the TS-MMS scaffold (**Figure 3.2**). The PLLA and TS-MMS scaffolds are casted with an excess of polymer solution, which forms a non-porous cap at the top of the scaffold that is subsequently cut off by a razor blade since implantable biomaterials with high host-integration rates typically require an interconnected, porous network for host stem cells to migrate through (**Figures 3.2 & 3.3C**).

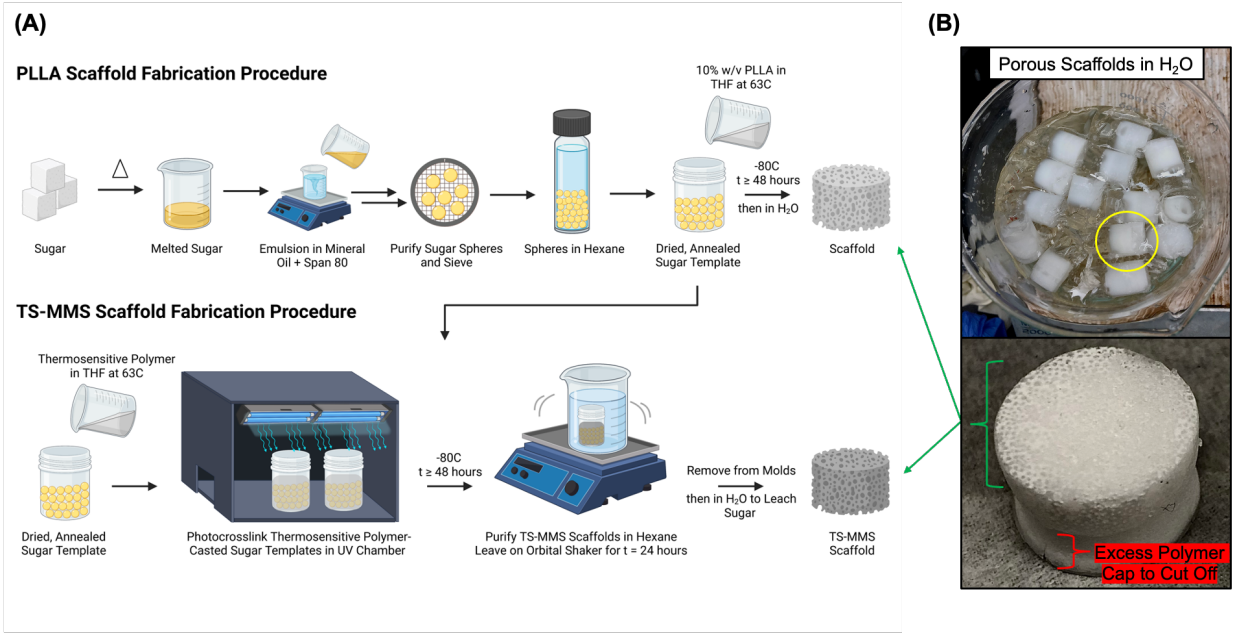

Figure 3.2: Overview of experimental procedures for scaffold fabrication. (A) Schematic of the methodology for making nanofibrous, porous PLLA scaffolds using the sugar porogen-leaching method and this modified methodology invented to fabricate thermosensitive, memorized-microstructure (TS-MMS) scaffolds using the TSM biomaterial. (B) Photograph of TS-MMS scaffolds in water after the sugar sphere leaching step and a magnified photograph of a TS-MMS scaffold taken out of the water from this cohort. Note that all scaffolds have an excess polymer cap that does not contain macropores; thus, it is cut off with a razor blade and discarded.

The optimized 40/60 TSM biomaterial from chapter 1 was dissolved and utilized as the polymer solution for the TS-MMS scaffold because it displayed nanofibrous morphology from TIPS, optimal clinically-relevant thermosensitive shaping properties, and optimal TSM. However, it was necessary to confirm that this biomaterial was still nanofibrous in a three-dimensional, macroporous scaffold. In addition, there was a concern that the TSM biomaterial components could phase separate in the scaffold to create a surface texture bilayer or cause the PCL-DA to migrate into the top excess polymer cap that was cut off, just as it did in the thin films. To these ends, XRD was performed on the TS-MMS scaffold, the PLLA control scaffold, and the bulk PLLA and PCL-DA polymers (**Figure 3.3B**). The XRD spectra for the PLLA bulk polymer and PLLA scaffold were nearly identical with the same characteristic X-ray diffraction angles,

confirming that the porous scaffold construct of the biomaterial did not significantly impact the XRD analysis. The TS-MMS scaffold XRD spectrum revealed that it diffracted X-rays at the same angles present in the PLLA bulk polymer and PLLA scaffold spectra in addition to diffracting X-rays at the same angles present in the PCL-DA bulk polymer.

This first demonstrated that both PLLA and PCL-DA were present in the final TS-MMS scaffold construct, proving that PCL-DA did not completely phase separate vertically into the top excess polymer cap that was cut off of the scaffolds. However, this still confirmed that the TSM biomaterial partially phase separated into its respective PLLA and PCL-DA semi-crystalline components. This result implied that there were nanofibers present in the TS-MMS scaffold because the PLLA was in the same crystalline state as the nanofibrous PLLA bulk polymer and nanofibrous PLLA scaffold. Still, it remained unknown if there was a non-homogenous macroscopic polymer distribution (e.g., bilayer) or an additional smooth surface topology present due to the PCL-DA phase separated, amorphous state that was observed in the thin films.

SEM morphology analysis was performed on cross-sections of the TS-MMS scaffold and the PLLA control scaffold to investigate if there was any macroscopic heterogeneity in the polymer distribution (**Figure 3.3C**). A uniformly distributed, nanofibrous network surrounding interconnected macropores was observed in both the PLLA control scaffold and the TS-MMS scaffold, indicating that no there was no obvious macroscopic phase separation of the PLLA and PCL-DA like in the TSM biomaterial thin films. This suggests that the PLLA and PCL-DA phase separated on a nanoscopic or molecular level, yielding an overall homogenous biomaterial. It is likely that the polymers were more restricted to migrate for macroscopic phase separation in the TS-MMS scaffold during the irradiation step of fabrication because of the sugar sphere confinement of the polymeric network. Additionally, the thickness of the scaffold construct with

respect to the thin film construct likely minimized the effects of the THF solvent evaporation at the air-exposed top and the reduced the UV penetration intensity for a slower, more controlled photocrosslinking reactions throughout the scaffold to minimize the PCL-DA macroscopic phase separation during the irradiation step of fabrication.

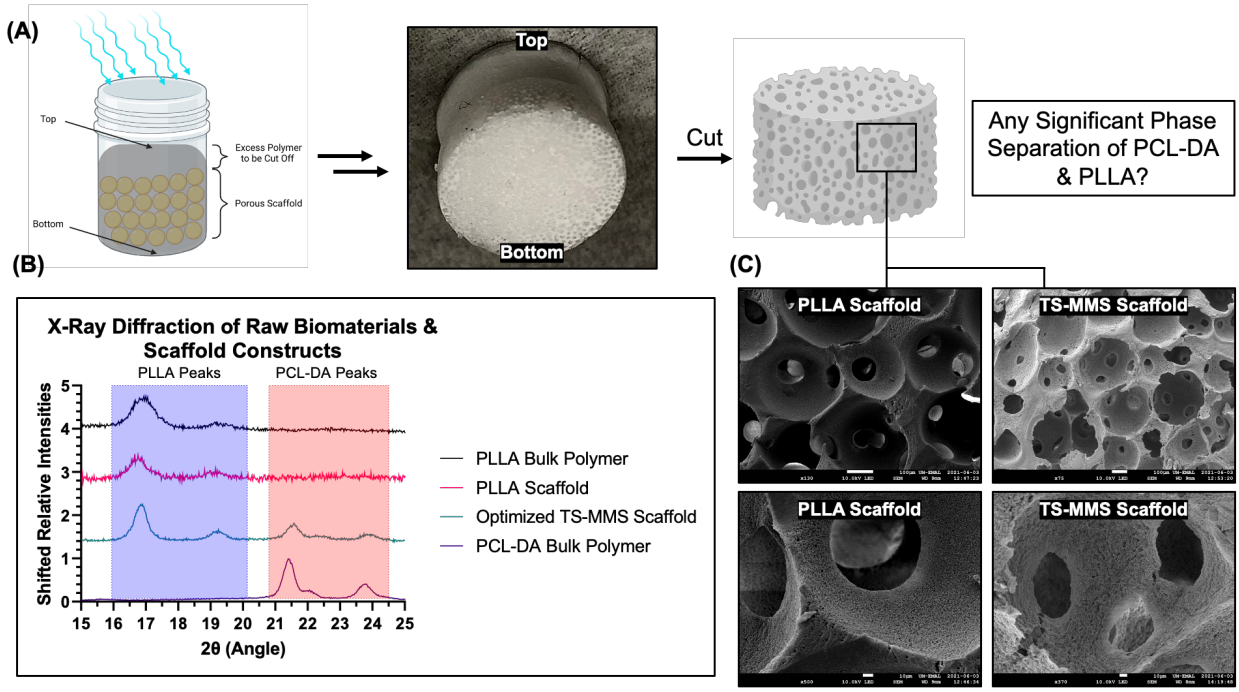

Figure 3.3: Morphology characterization of the scaffolds. (A) Visual schematic of TS-MMS scaffold irradiation step and the excess polymer cap formation that is cut-off in the final porous TS-MMS scaffold construct. This presents the concern that the PCL-DA phase separates into the excess polymer cap that gets cut-off due to the biphasic morphology formation of the TSM biomaterial thin films and membranes presented in Chapters 1 and 2. Additionally, there is a similar concern of a biphasic morphology in the TS-MMS scaffold due to PCL-DA and PLLA phase separation during TIPS. (B) Overlaid x-ray diffraction spectra of the PLLA bulk polymer, the PLLA scaffold, the cut TS-MMS scaffold, and PCL-DA bulk polymer. The blue rectangle represents the region of the spectrum where PLLA x-ray diffraction peaks are observed, and the red region represents the region of the spectrum where PCL-DA x-ray diffraction peaks are observed. The TS-MMS scaffold x-ray diffraction spectrum contains characteristic peaks of PLLA and PCL-DA, suggesting that there is PCL-DA in the final cut scaffold product but that it is phase separated from PLLA. Additionally, the x-ray diffraction peaks of PLLA suggest the scaffold is nanofibrous. (C) Representative scanning electron microscopy images of the PLLA scaffold and the TS-MMS scaffold demonstrating that both scaffolds have interconnected, homogenous macropores and that there is not biphasic morphology formation in the TS-MMS scaffold.

To confirm with higher confidence that the PCL-DA was still present in the TS-MMS scaffold after cutting the excess polymer cap off, TGA was performed on the TS-MMS scaffold and the raw PCL-DA biomaterial (**Figure 3.4A,B**). The TS-MMS scaffold exhibited two distinct peaks in the derivative of the weight percentage with respect to temperature (dW/dT) and the PCL-DA bulk biomaterial exhibited one peak in the dW/dT. These peaks represent the unique combustion temperatures of each polymer, indicating that the TS-MMS scaffold had two thermal combustion temperatures corresponding to the separate PLLA and PCL-DA biomaterials infused into the TS-MMS scaffold. This claim was strengthened by the observation that the second dW/dT peak in the TGA of the TS-MMS scaffold overlapped with the bulk PCL-DA biomaterial dW/dT peak, indicating that this peak was unique to PCL-DA in both experiments. Thus, the first dW/dT peak in the TS-MMS scaffold was attributed to PLLA, and the TS-MMS scaffold was confirmed to have both polymers present.

The presence of two dW/dT peaks in the TGA of the TS-MMS scaffold provided additional evidence to confirm that the PLLA and PCL-DA were chemically separate and phase-separated in the final scaffold product. This indicated that the PCL-DA was not reacting with PLLA during photocrosslinking, as expected and intended in their polymeric design. Furthermore, the presence of two thermal combustion rates in the TS-MMS scaffold indicates different reactivities of PLLA and PCL-DA. This reasonably implies that would be two different rates of hydrolysis during the TS-MMS scaffold degradation, or biphasic degradation as observed in the TSM biomaterial thin film (**Figure 3.4C**). However, because the TS-MMS scaffold was observed to be macroscopically homogenous in **Figure 3.3C**, the biphasic degradation was not assumed to be highly relevant since the scaffold would not degrade in structural parts as observed in the thin films; rather, it was assumed that the PLLA would degrade faster than the PCL-DA since PLLA is more hydrophilic,

but that the TS-MMS scaffold structure would remain in-tact during this degradation and thus the structural degradation of the scaffold would be limited by the rate of hydrolysis for PCL-DA (**Figure 3.4**).

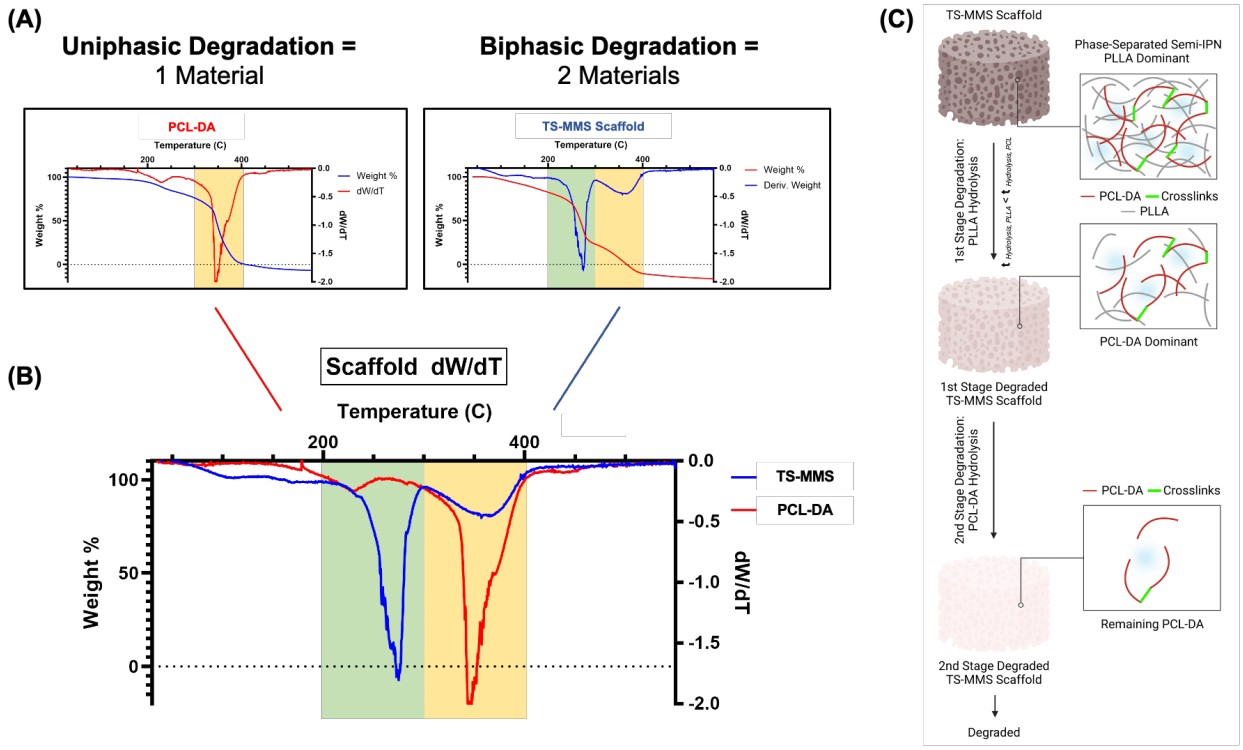

Figure 3.4: Degradation characterization of the TS-MMS scaffold and confirmation of PCL-DA presence in the final, cut TS-MMS scaffold product. (A) Thermogravimetric analyses of PCL-DA bulk polymer and a cut TS-MMS scaffold. The green rectangle highlights the region of PLLA thermal combustion degradation and the yellow rectangle highlights the region of PCL-DA thermal combustion degradation. (B) Overlaid weight derivatives with respect to temperature (dW/dT) from the PCL-DA bulk polymer and TS-MMS scaffold TGA plots in (A). The green rectangle highlights the region of PLLA thermal combustion degradation and the yellow rectangle highlights the region of PCL-DA thermal combustion degradation. (C) Visual schematic of the hypothesized biphasic hydrolytic degradation of a TS-MMS scaffold. The biphasic hydrolytic degradation is implied from the TGA biphasic thermal combustion of the TS-MMS scaffold.

One clinical limitation of porous scaffolds is that their overall structures are often brittle and fragile due to the porosity, which hinders the degree to which they can be compressed and shaped to clinical defects without running the risk of compromising the material and collapsing the

macropores. Thus, it was desirable to maximize the durability and mechanical properties of the TS-MMS scaffolds to combat this problem. It was hypothesized that this could be achieved by increasing the total w/v percentage of TSM biomaterial dissolved in THF prior to the polymer casting on the sugar template, which was held constant at 10% w/v until this point. Additionally, it was hypothesized that this would increase the PCL-DA spatial crosslinking density within the scaffold because there would be proportionally more TSM biomaterial in the TS-MMS scaffold. This would result in a better memorized microstructure for macropore shape recovery.

TS-MMS scaffolds were fabricated from 40/60 TSM biomaterial at four different w/v percentages in THF alongside a PLLA control scaffold made from 10% w/v PLLA in THF. Their compressive moduli were investigated at 25C and 80C by soaking the scaffolds in a water bath of the desired temperature for five minutes before doing a compression analysis (**Figure 3.5A**). Increasing the total w/v material percentage in the TS-MMS scaffold resulted in higher compressive moduli at both temperatures, but the PLLA control scaffold was measured to have the highest compressive modulus. The TS-MMS scaffolds were measured to have a statistically significant decrease in their compressive moduli upon being heated to 80C, but the PLLA scaffolds had no statistically significant decrease in their compressive modulus between 25C and 80C. This was an indication that the TS-MMS scaffolds had clinically-relevant thermosensitive properties due to the presence of PCL-DA, which achieves a viscous, rubber-like state upon being heated to its first melting point above 50C. Thus, the TS-MMS scaffolds could achieve a more flexible, rubbery state upon heating for easier deformation and enhanced shaping.

Increasing the TSM biomaterial w/v percentage in the TS-MMS scaffolds raised a concern about destroying the advantageous nanofibrosity of the scaffold because the TSM biomaterial needs to have a sufficiently low density in THF such that it can spatially phase separate through

TIPS to create the amorphous PLLA nanofibers separated from PCL-DA. SEM morphology analysis was performed on the cross-sections of the TS-MMS scaffold at different material w/v percentages to investigate the presence and quality of the nanofibers (**Figure 3.5B**). Well-defined, homogenous nanofibers that strongly resemble those of PLLA scaffolds were observed in TS-MMS scaffolds composed of up to 15% w/v material in THF. It was debatable whether the 20% w/v material in THF TS-MMS scaffold exhibited nanofibers of sufficient quality for cell adhesion, but it was cautiously decided to proceed with the 15% w/v material in THF TS-MMS scaffolds since they exhibited had optimal strength with quality nanofiber formation.

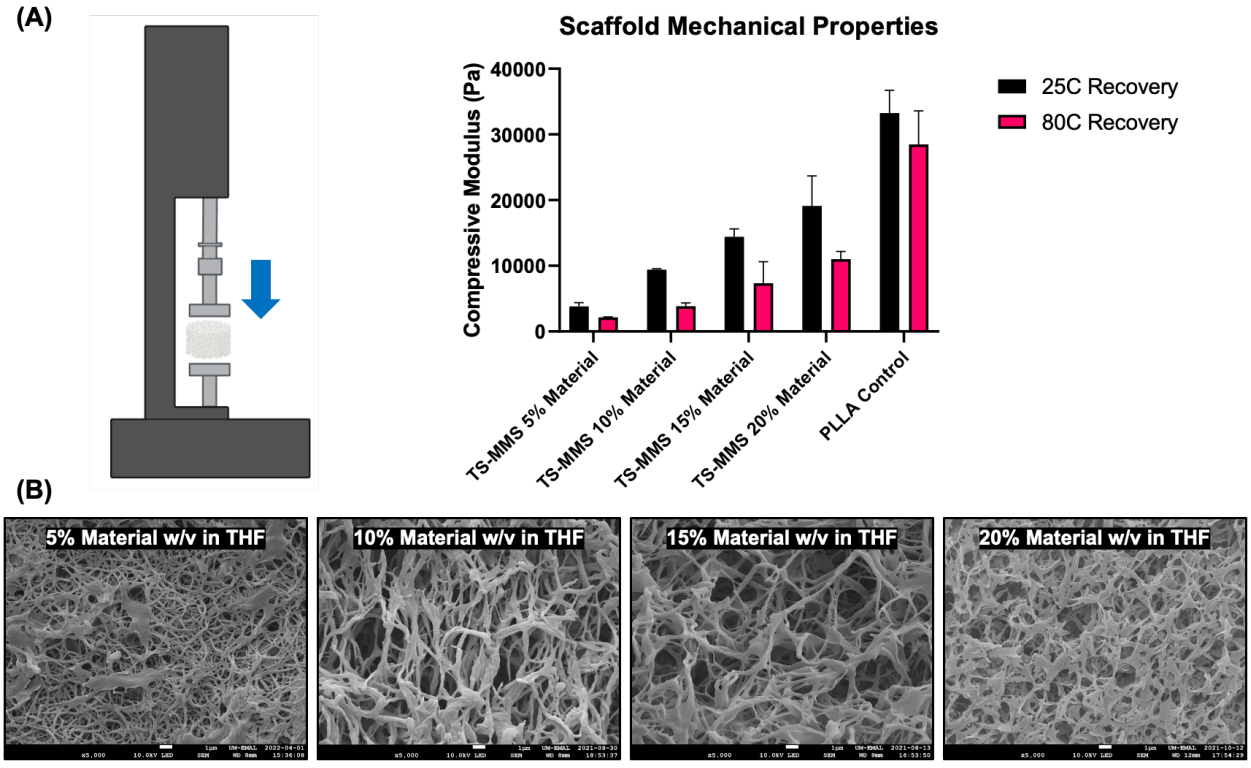

Figure 3.5: Mechanical properties and nanofiber characterization of TS-MMS scaffolds fabricated under different total TSM biomaterial w/v in THF. (A) Visual of compressive procedure by mechanical testing machine with the measured mean compressive moduli for TS-MMS scaffolds at different temperatures fabricated from different w/v concentrations of TSM biomaterial in THF. For example, 10% material represents 1 g of the optimized TSM biomaterial composed of 40% PCL-DA and 60% PLLA (i.e., 0.4 g of PCL-DA and 0.6 g of PLLA) dissolved in 10 ml of THF. Error bars represent one standard deviation. (B) Representative scanning electron microscopy

images of the nanofibers present in each TS-MMS scaffold fabricated at a different TSM biomaterial w/v in THF.

It was further hypothesized that the TS-MMS scaffolds could increase their compressive moduli and be made more durable through a heat-treatment process above the transition temperature of the crosslinked PCL-DA network, as is common with other synthetic material networks. By allowing the TS-MMS scaffold to achieve a rubbery state above its first transition temperature, corresponding to the melting point of PCL-DA (**Figure 3.7A**), it was predicted that the crosslinked PCL-DA polymeric chains would be kinetically enabled to have limited movement in the semi-interpenetrating network. This allows them to adopt a lower energy geometric conformation from minor physical rearrangement to reduce the internal stress of the TS-MMS scaffold, resulting in a stronger biomaterial with a higher compressive modulus. To this end, TS-MMS scaffolds were heat-treated at 75C for 60 minutes, which were both chosen arbitrarily under the condition that the temperature had to be above the transition temperature of PCL-DA (**Figure 3.6A**). Upon removal from the 75C oven, the heat-treated scaffolds were allowed to slowly cool to room temperature.

The heat-treated TS-MMS scaffolds were measured to have a higher compressive modulus than the control, non-heat-treated TS-MMS scaffolds (**Figure 3.6C**). Furthermore, the heat-treated TS-MMS scaffold retained its thermosensitive properties as its compressive modulus was measured to be lower at 80C indicating that it was still achieving a rubbery transition state. In comparison, the PLLA control scaffold compressive moduli at both temperatures were not significantly affected by the same heat-treatment process. This supports the mechanistic hypothesis that the heat-treatment is influencing the PCL-DA conformation in the TS-MMS scaffold. To ensure that the heat-treatment was not destroying the favorable nanofibrous topology or homogeneity of the TS-MMS scaffold, SEM morphology analysis was performed on cross-

sections of the heat-treated and non-heat-treated TS-MMS scaffolds (**Figure 3.6B**). No significant differences were observed in the morphologies between the two groups as nanofibers and a macroscopically homogenous morphology were observed in all TS-MMS scaffolds. This suggests that the PCL-DA conformation rearrangement during heat-treatment happens on a nanoscopic or molecular level in the backbone of the PCL-DA chains, and that the PCL-DA is not significantly migrating in space within the scaffold to compromise or alter the memorized microstructure of the semi-interpenetrating polymeric network. Ultimately, it was determined that heat-treating the TS-MMS scaffold further optimized its strength without compromising the thermosensitive properties or the homogenous, nanofibrous morphology of the scaffold. Thus, all further experiments used heat-treated TS-MMS scaffolds, unless otherwise stated.

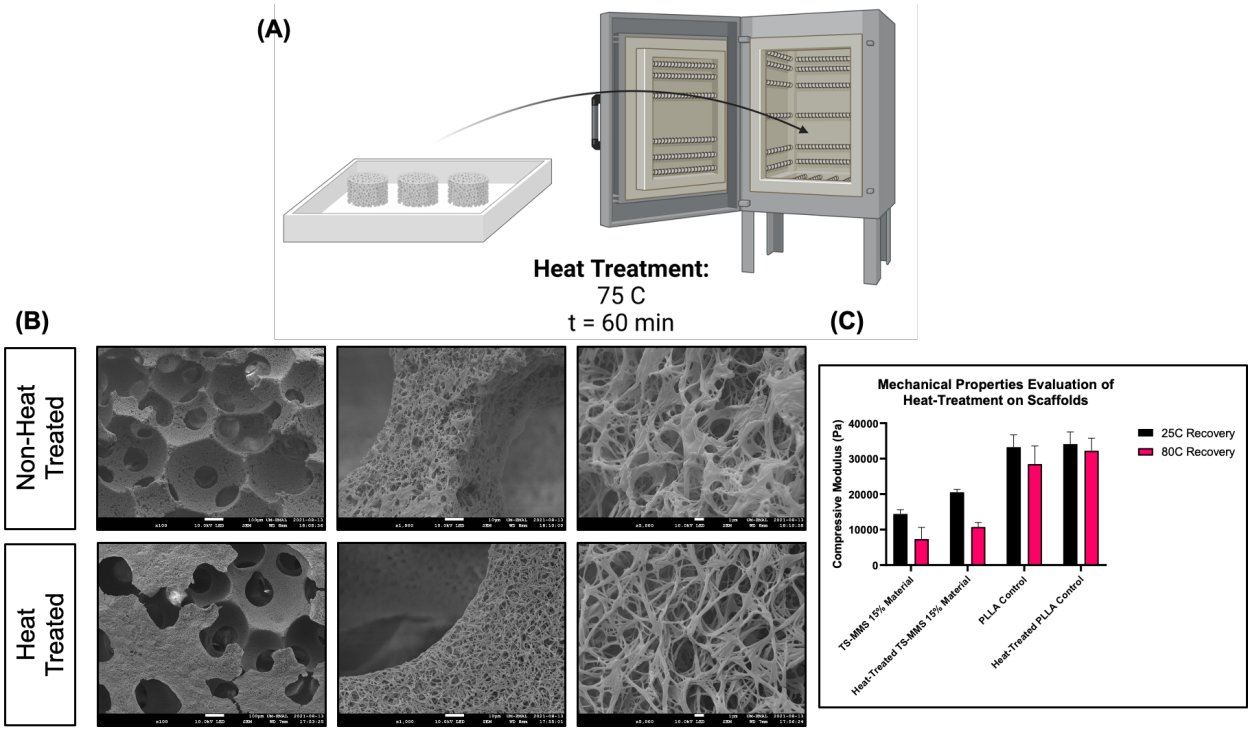

Figure 3.6: Mechanical properties and nanofiber characterization of TS-MMS and PLLA scaffolds fabricated with an additional heat-treatment step compared to the control scaffolds that do not receive heat treatment. (A) Visual schematic of the heat-treatment procedure, which consists of heating scaffolds at 75C for 60 minutes in a convection oven. (B) Representative scanning electron microscopy images of TS-MMS scaffolds fabricated from 15% material that were either

the control (non-heat treated) or heat-treated (heat treated). Magnification progressively increases from left to right. (C) Measured mean compressive moduli for heat-treated and non-heat-treated TS-MMS and PLLA scaffolds at 25C and 80C. Error bars represent one measured standard deviation.

The optimized TS-MMS and PLLA scaffolds were analyzed by DSC to compare their physical properties over different temperatures (**Figure 3.7A**). Both the TS-MMS scaffold and PLLA scaffold had an endothermic double between 155-185C corresponding to the melting point of PLLA. Additionally, TS-MMS scaffold was measured to have an endothermic peak between 50-60C that was not present in the PLLA scaffold, indicating that this peak corresponded to the melting point of PCL-DA. The T_{M1} of the PLLA scaffold and the TS-MMS scaffold was calculated from these DSC data (**Figure 3.7A**). This calculated to be about 50C for the optimized TS-MMS scaffold and about 168C for the PLLA scaffold, indicating that the PCL-DA was imparting clinically-relevant thermosensitive properties into the TS-MMS scaffold. This indicated that the physical properties of the TS-MMS changed at temperatures above 50C, explaining the difference in the compressive moduli between 25C and 80C temperatures measured in **Figures 3.5B & 3.6C**. Similarly, this implied that the TS-MMS scaffold would theoretically trigger TSM of the macropores at temperatures above 50C.

The nanofibrous surface topology and macropore structure morphologies of the TS-MMS scaffolds were qualitatively investigated during every stage of a thermosensitive cycle (**Figure 3.7D**). To this end, cross-sections were taken from the TS-MMS scaffolds at the virgin, deformed, and recovered stage of a thermosensitive cycle and imaged by SEM (**Figure 3.7C**). The nanofibrous surface topology was present in the TS-MMS scaffolds at every stage of a thermosensitive cycle, indicating that they were unaffected by the heating cycles and deformation of the scaffold. This is to be expected because the nanofibers are mostly PLLA, which is not thermosensitive at the temperatures used in this experiment. On the contrary, it was observed that

the macropores were deformed by a 50% compression of the overall scaffold at the deformed stage; many macropores were crushed shut completely or severely misshapen. However, the recovered TS-MMS scaffold cross-sections revealed reopened, spherical macropores that resembled the virgin cross-sections. PLLA control scaffolds and additional TS-MMS scaffolds were then subject to one full thermosensitive cycle so that their macroscopic recovered structures could be investigated with light microscopy (**Figure 3.7E**). The recovered TS-MMS scaffold was again observed to have open, spherical macropores, replicating the findings in the SEM cross-section of the recovered TS-MMS scaffold, but the PLLA scaffold macropores appeared to still be longitudinally stretched and compressed transverse to the mechanical deformation. Additionally, less visible light was qualitatively observed to pass through recovered PLLA scaffold in comparison to the recovered TS-MMS scaffold, indicating that the PLLA scaffold pores were more compressed. These results qualitatively suggested that the TS-MMS scaffold was capable of TSM after a compression deformation, and that the PLLA control scaffold did not possess TSM, as expected.

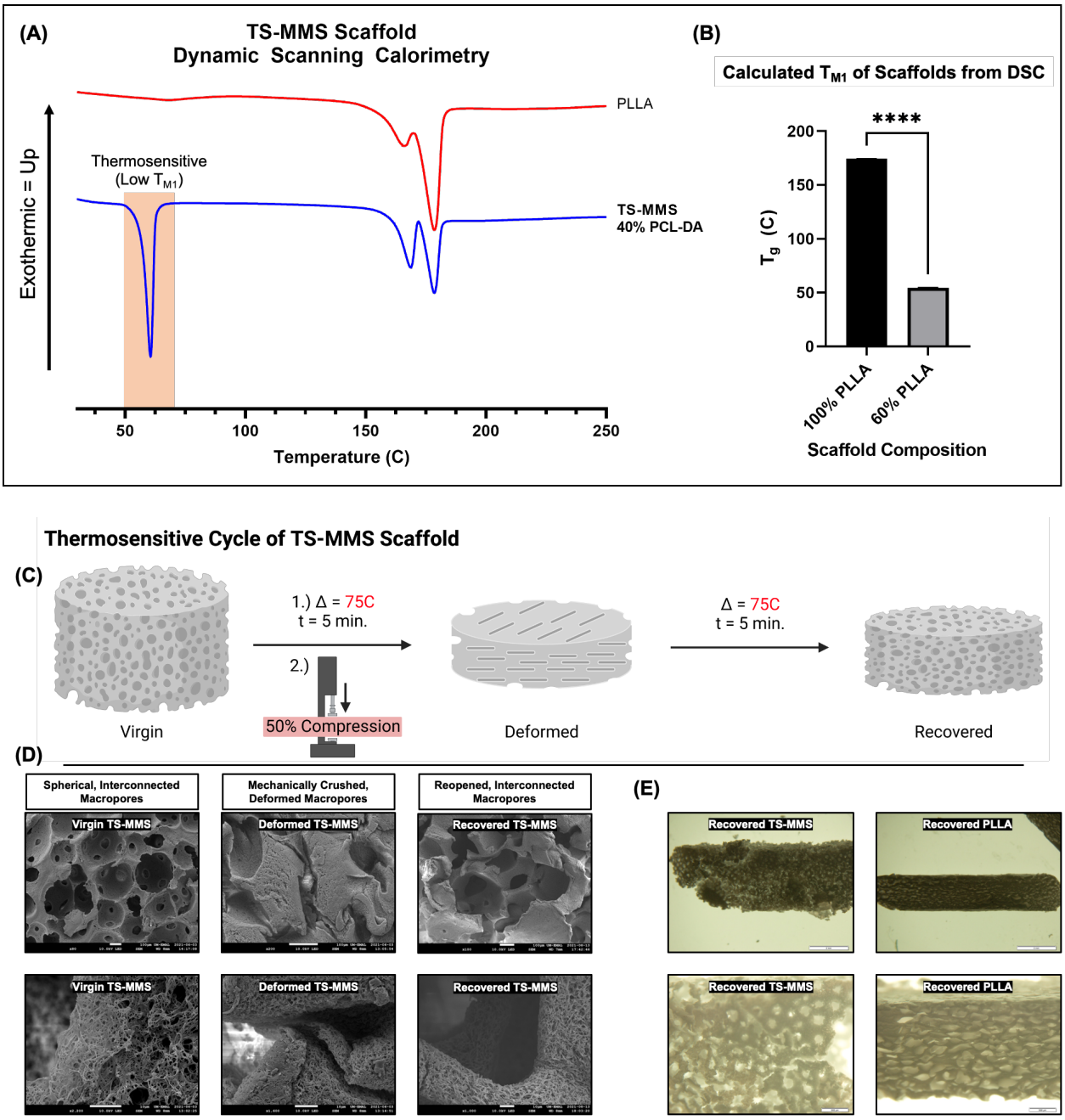

Figure 3.7: Thermal properties characterization of the TS-MMS scaffolds compared with PLLA scaffolds and an experiment investigating macropore shape memory. (A) Overlaid dynamic scanning calorimetry spectra for a PLLA scaffold and a TS-MMS scaffold, where exothermic is designated by the upward direction. The orange rectangle highlights the first melting point in the TS-MMS scaffold, corresponding to the melting point of PCL-DA which gives the TS-MMS scaffold its clinically relevant thermosensitive properties. (B) The calculated first melting point (T_{M1}) of the PLLA scaffold and the TS-MMS scaffold. (C) Visual schematic of the experimental procedure performed for mechanically deforming the scaffold macropores and recovering them in the TS-MMS scaffold. (D) Representative scanning electron microscopy images of the macropores

and nanofibers, respectively, of TS-MMS scaffolds stopped each stage of the experiment outlined in (C) (e.g., the deformed scaffold received the mechanical compression but was not reheated to recover the macropores). (E) Representative bright field microscopy images with two magnifications of the recovered TS-MMS scaffolds and the recovered PLLA scaffolds from the experiment performed in (C). The macropores of the recovered TS-MMS scaffold are open and spherical whereas the macropores of the recovered PLLA scaffold are crushed, which is expected because the PLLA scaffold has no thermosensitive polymer or mechanism of shape-memory.

Clinical defects are often irregularly shaped and require a biomaterial to be sculpted and compressed non-uniformly to be fitted to the defect during implantation. Additionally, it is typically unfeasible or non-ideal to remove a biomaterial after implantation to manipulate or recover its properties lost during this sculpting and shaping process (e.g., recover macropores via heating in hot water). Thus, a clinical-shaping implantation procedure was devised to simulate how a TS-MMS scaffold could be deformed and shaped to a patient defect, and how its macropores could be recovered *in-vivo* directly after implantation (**Figure 3.8A**). It should be noted that the temperature of the water used to recover the macropores of the TS-MMS scaffold *in-vivo* was chosen to be 55C because this is a temperature that is above the T_{M1} of the scaffold that is not harmful to human tissue.

This implantation procedure was performed with TS-MMS scaffolds in two sets of experiments. The first experiment qualitatively investigated the ability for the TS-MMS scaffolds to be shaped to irregularly-shaped defects cut into a hydrogel (**Figure 3.8B**). The water-heated TS-MMS scaffolds were able to be shaped by-hand to the four different defects that were cut into the hydrogel. Furthermore, the 55C water that was dripped over five minutes onto these implanted TS-MMS scaffolds appeared to slightly expand the TS-MMS scaffold macroscopic shape to fill in any extra void space that was unaccounted for during implantation such that the TS-MMS scaffold contoured the irregular shape with high precision. This was a qualitative indication that the

deformed macropores were reopening and recovering their macroscopic shape, causing the TS-MMS scaffold to expand slightly.

A second experiment was conducted to simulate a jawbone regeneration scenario with the TS-MMS scaffold for a patient with a pulled molar (**Figure 3.8C**). The TS-MMS scaffold was heated and shaped to the molar defect and recovered *in-vivo* with the hot water droplet method. The TS-MMS scaffold was then removed and cross-sectioned for SEM morphological analysis (**Figure 3.8C**). This recovered scaffold demonstrated open, spherical macropores and a nanofibrous surface topology, indicating that hot water droplet method for TS-MMS scaffold recovery was capable of triggering TSM of the macropores *in-vivo*.

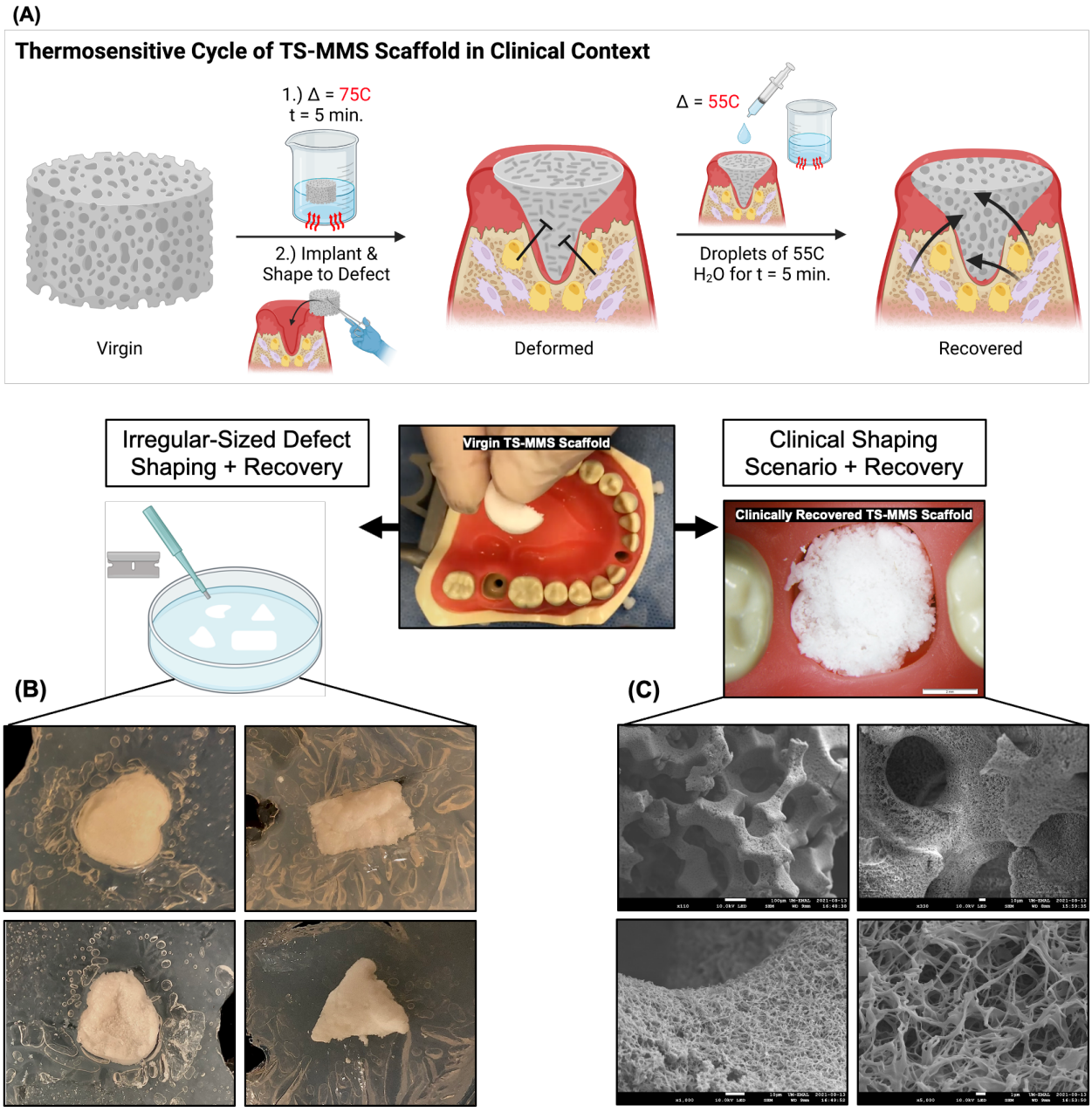

Figure 3.8: Clinical shaping and simulated *in-vivo* macropore recovery experiments demonstrating the TS-MMS scaffold translatability. (A) Designed procedure for shaping and implanting a TS-MMS scaffold into an extracted-tooth socket with a warm-droplet method to recover the TS-MMS scaffold macropores *in-vivo* after implantation. Virgin TS-MMS scaffolds were taken and first shaped to four irregularly-shaped defects cut into a hydrogel and allowed to recover their macropores, following the entire procedure of (A). (B) Photographed images of the recovered TS-MMS scaffolds shaped to the irregularly-shaped defects cut in the hydrogels. Then, a virgin TS-MMS scaffold was taken and implanted into a model extracted-tooth socket using the shaping and macropore recovery procedure designed in (A). (C) Representative scanning electron

microscopy images of different magnifications investigating the morphology and surface topology of the recovered TS-MMS scaffold implanted into the extracted-tooth socket.

These preliminary, qualitative experiments suggested that the TS-MMS scaffolds were recovering their macropores through TSM. An experiment was designed to investigate the statistical significance of these claims by quantitively examining histology slices of cross-sectioned TS-MMS and PLLA scaffolds after each stage of a thermosensitive cycle (**Figure 3.9A**). Light microscopy images of histology slices provided two-dimensional information about the macropore shapes throughout the thick scaffold cross-sections at each stage in the thermosensitive cycle (**Figure 3.9B**). These images were processed in ImageJ where each macropore was individually traced such that its circularity could be measured using ImageJ. This calculation was performed for all the macropores in the histology slices for the TS-MMS and PLLA scaffolds at the different thermosensitive cycle stages and the results were plotted (**Figure 3.9C**).

The TS-MMS scaffold had a significant decrease in macropore circularity between the virgin scaffold and 50% deformed scaffold, indicating that a sufficient compression was imposed on the TS-MMS scaffold to cause macropore deformation. Furthermore, a significant increase in macropore circularity was measured between the 50% deformed scaffold and the recovered TS-MMS scaffold, indicating that the macropores successfully underwent TSM to re-open to their memorized, spherical structure. It is also noteworthy that there was no significant difference between the macropore circularity of the virgin TS-MMS scaffold and the recovered TS-MMS scaffold, suggesting that the macropores were not damaged during the thermosensitive cycle and that the TSM macropore recovery was highly effective. On the contrary, the PLLA scaffold was measured to have a significant decrease in macropore circularity between the virgin and deformed stages, followed by no significant change in macropore circularity between the deformed and recovered stages. This implies that there was no TSM of the macropores in the PLLA scaffold, as

expected because PLLA is not thermosensitive across the temperatures of deformation or recovery used in this experiment, nor is it crosslinked as a mechanism for microstructure memorization. Finally, it should be noted that the PLLA scaffold sustained more damage to its macropores during a 50% compressive deformation at 75C than the TS-MMS scaffold receiving the same deformation under the same conditions (**Figure 3.9C**). This is likely because PLLA is brittle and cracks under stress, whereas the TS-MMS scaffold achieves a rubbery state above the T_{M1} and therefore can elongate outward better in response to compressive stress, rather than cracking and failing like PLLA.

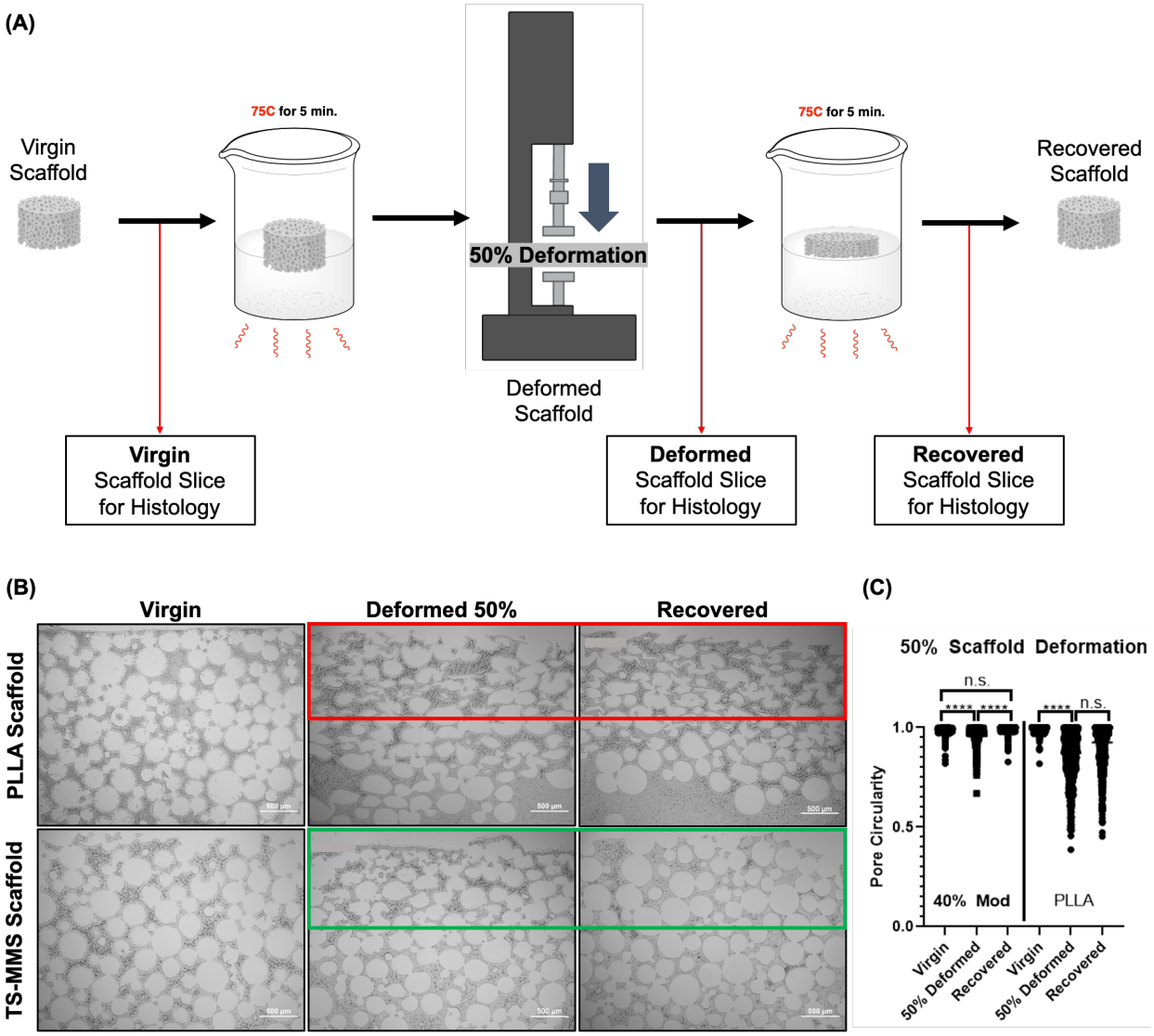

Figure 3.9: Quantitative macropore recovery experiment for TS-MMS scaffolds and PLLA scaffolds. (A) Schematic of the experimental procedure used to controllably deform and recover the scaffolds, and the stages at which cross-section slices of the scaffolds were taken for histology. (B) Representative bright field microscopy images of the TS-MMS and PLLA scaffold histology slices taken at each point of the procedure outlined in (A). (C) Violin plots of the measured macropore circularities from the image analyses of the histology slices at different points of the thermal deformation and recovery cycle for the TS-MMS and PLLA scaffolds, respectively.

3.3.2 Scaffold Nanofiber-Embedded Nanoparticle Drug Delivery System

Cell behaviors in biological tissues are influenced by combinations of chemical and physical factors in their local microenvironment.[10] This also applies to repair and regenerative processes.

Thus, it is important that an effective tissue engineering strategy should utilize both chemical and physical factors to predictably guide cell fate towards the desired outcome. The TS-MMS scaffolds were optimized to create a favorable physical microenvironment intended for skeletal stem cell adhesion, migration, and differentiation; however, they lacked a noteworthy chemical component, drug-delivery system, or surface coating to aid this process via molecular factors.

Previous methods in the literature have demonstrated the incorporation of a nanoparticle drug-delivery system within the nanofibers of PLLA scaffold via a solvent wetting method (**Figure 3.10B**).[21] Nanoparticle drug-delivery systems are advantageous because they are extremely versatile with the molecular therapeutics that they can deliver, as nanoparticles have been fabricated encapsulating biomolecules, macromolecules, and small molecules.[4] However, the solvent wetting method for incorporating a nanoparticle drug-delivery system within a scaffold is highly limited by the fact that the nanoparticles cannot be homogenously distributed throughout the scaffold or within the scaffold material for sustained release over time. Rather, the nanoparticles are only coated on the surface of the scaffold nanofibers where the droplets are applied, leading to a rapid burst of therapeutic release in a highly specific region of the scaffold. This is ultimately an inefficient and uncontrolled method to deliver molecular therapeutics using a scaffold construct.

To rectify this, a novel sugar-particle adhesion method was designed to homogenously embed PLGA nanoparticles encapsulating molecular therapeutics into the nanofibers of a TS-MMS scaffold (**Figure 3.10A**). This method sought to take advantage of the sugar-porogen leaching method used to fabricate general porous scaffolds. It was hypothesized that the PLGA nanoparticles would adhere to the sugar spheres in hexane solution due to the high hydrophilicity of PLGA and fructose in combination with the high hydrophobicity of hexane that would enhance

this aggregation to maximize entropy. Furthermore, it was hypothesized that casting the TSM biomaterial, or any general biomaterial, on the dried sugar template surface coated with nanoparticles would partially dissolve or remove the nanoparticles off of the surfaces of the sugar spheres such that they became embedded in the TSM biomaterial and would phase separate into the nanofibers of the biomaterial during TIPS.

PLGA nanoparticles encapsulating Rhodamine 6G (R6G) as a red fluorescent dye were synthesized for convenient visual tracking of the nanoparticles during the scaffold fabrication process. The nanoparticles were added to a vial of hexane solution containing sugar spheres that were 250-500 μm in diameter (**Figure 3.10D**). The solution was thoroughly mixed to ensure homogenous nanoparticle distribution and adhesion to the sugar spheres. A sugar template was constructed in a Teflon mold from the sugar spheres coated with nanoparticles, where the spheres were lightly annealed and the hexane was allowed to completely evaporate (**Figure 3.10D**). Light microscopy images revealed that this sugar template was tinted red, which was confirmed with z-stacked confocal microscopy images to demonstrate that the PLGA nanoparticles encapsulating R6G were uniformly adhered to the surfaces of the sugar spheres throughout the entire sugar template (**Figure 3.10C**). Additionally, SEM was performed on the sugar sphere template that revealed textured surfaces attributed to the adhered nanoparticle surface coating (**Figure 3.10E**). These surfaces were notably more textured than SEM imaged control sugar sphere templates without nanoparticles, which were extremely glossy and smooth (**Figure 3.10F**).

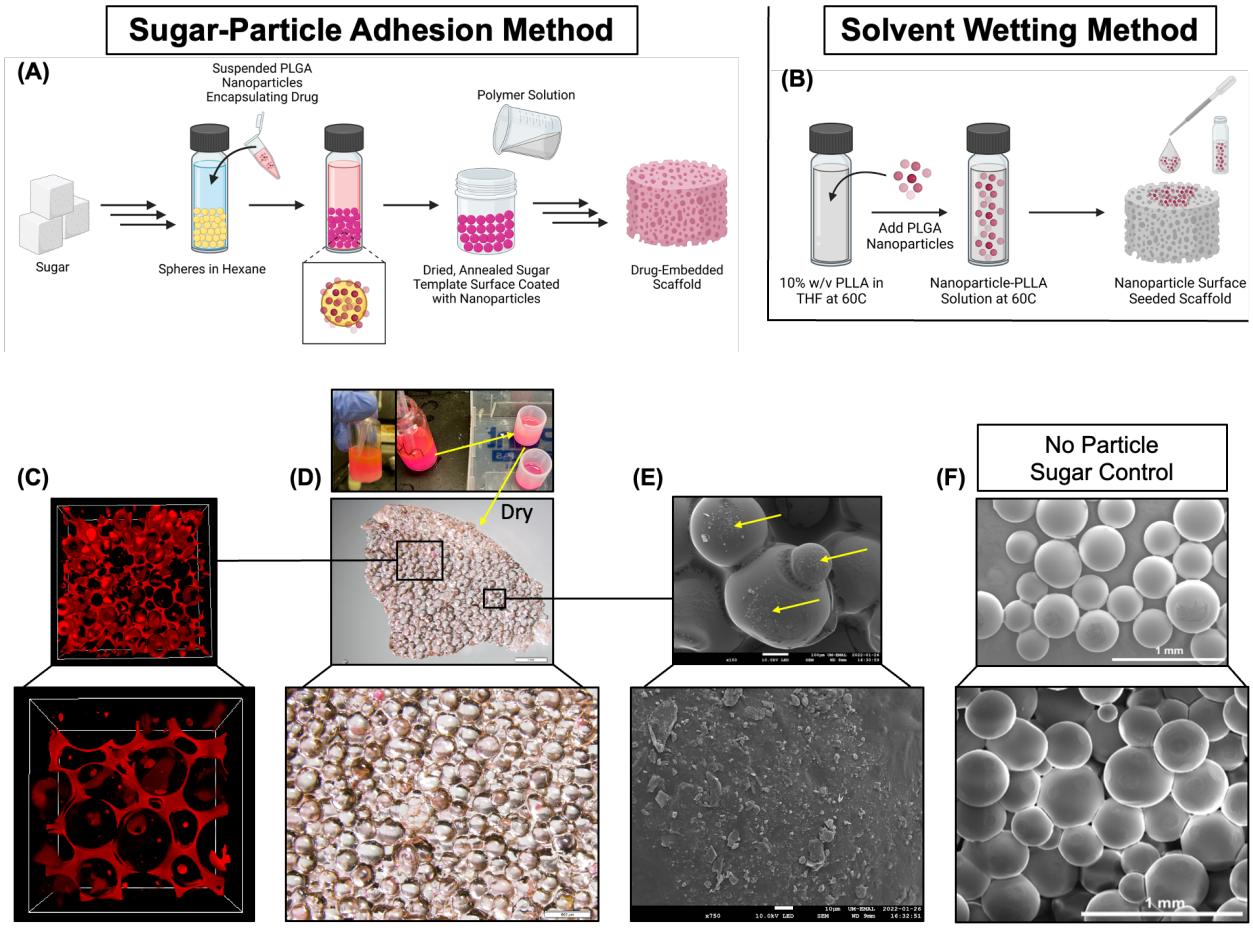

Figure 3.10: Characterization of the sugar spheres and the sugar template using the new sugar-particle adhesion method to embed nanoparticles encapsulating therapeutics into scaffolds. (A) Visual schematic of the designed sugar-particle adhesion method to embedded nanoparticles into a scaffold. Nanoparticles are depicted as red. (B) Visual schematic of the solvent wetting method procedure previously used in the literature to install nanoparticles into scaffolds. (C) Representative confocal microscopy z-stacked images of different magnifications of the annealed sugar-nanoparticle adhesion template shown in (D). Note that the nanoparticles are encapsulating rhodamine b and the confocal microscopy is visualized with an excitation laser of 546 nm directed at the sample to fluoresce the encapsulated rhodamine b. (D) The PLGA nanoparticles encapsulating rhodamine b adhering to the sugar spheres in hexane, the creation of the sugar sphere template with the adhered nanoparticles, and the final dried, annealed sugar sphere template for scaffold casting with the nanoparticles adhered to the surface of the sugar spheres, giving them a red color. The sugar sphere template was imaged under bright field microscopy. (E) Representative scanning electron microscopy images of annealed sugar spheres with adhered nanoparticles on the surface. The yellow arrows point to the textured, uneven surface of the sugar spheres corresponding to the adhered nanoparticles. (F) Representative scanning electron microscopy images of the control sugar spheres that do not have adhered nanoparticles on their surface. They are completely smooth due to the emulsion fabrication process of the sugar spheres.

With evidence to confirm that the nanoparticles were homogenously adhering to the sugar sphere template, these templates were replicated and cast with the TSM biomaterial. Additionally, a control sugar template without nanoparticles was constructed and cast with the TSM biomaterial such that the resulting scaffold product could have a nanoparticle drug-delivery system installed via the solvent wetting method for direct comparison between the two methods. The final TS-MMS scaffold products with the nanoparticle drug-delivery systems installed by the two different methods were qualitatively compared for nanoparticle distribution (**Figure 3.11A**). Light and fluorescent microscopy images of each nanoparticle-embedded TS-MMS scaffold confirmed the solvent wetting method limitation of concentrating the nanoparticles only on the surface of the scaffold where the droplets of nanoparticle-PLLA solution were applied (**Figure 3.11B**). In contrast, the sugar-particle adhesion method resulted in a homogenous distribution of the nanoparticles throughout the TS-MMS scaffold surface.

Cross-sections of each scaffold were then taken and imaged by confocal microscopy (**Figure 3.11C**). Similarly, the solvent wetting method revealed limited nanoparticle penetration into the scaffold construct because it is restricted to manually applying nanoparticles to the exposed surfaces of the scaffold construct. The sugar-particle adhesion method again resulted in an approximately homogenous distribution of nanoparticles that penetrated the entire scaffold. Z-stacked confocal images were acquired from the cross-section of the sugar-particle adhesion method TS-MMS scaffold to reveal nanoparticles outlining the contour of the macropores in the scaffold and penetrating within the material (**Figure 3.11D**). This suggests that the nanoparticles are not limited to just the macropore surfaces of the TS-MMS scaffold, but that they are embedded within the TS-MMS scaffold material which was hypothesized to yield time-sustained release kinetics. Ultimately, it was demonstrated that this novel sugar-particle adhesion method for

installing nanoparticle drug-delivery systems within scaffold constructs was highly effective at homogenously distributing and embedding the nanoparticles in the scaffold.

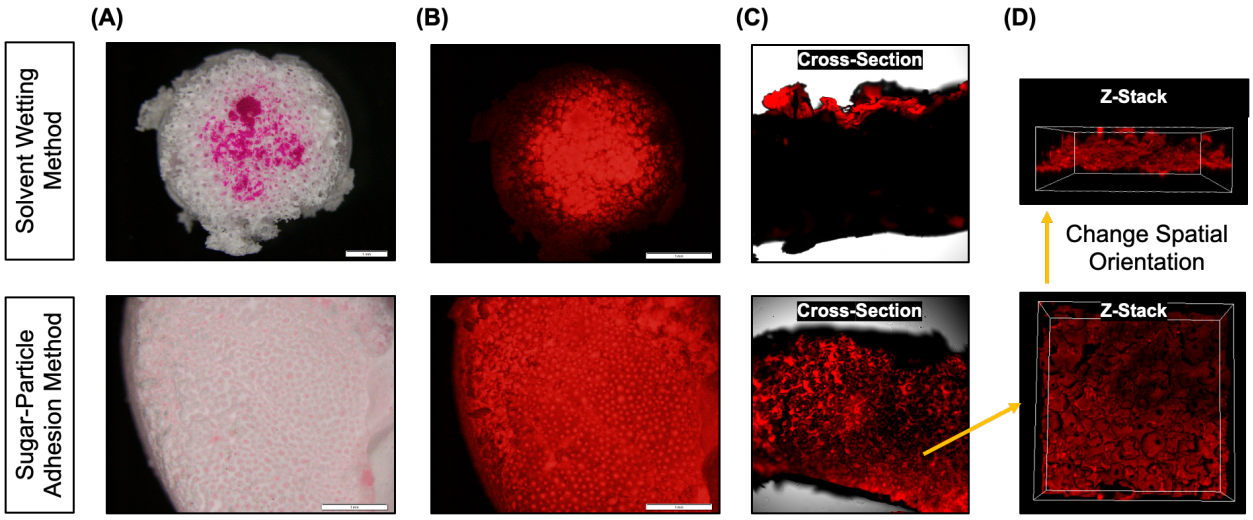

Figure 3.11: Solvent wetting method and sugar-particle adhesion method distribution of PLGA nanoparticles encapsulating rhodamine b within TS-MMS scaffolds, respectively. (A) Bright field microscopy images of TS-MMS scaffolds with nanoparticle drug delivery systems encapsulating rhodamine b installed via the solvent wetting method and sugar-particle adhesion method, respectively. (B) Fluorescence microscopy images of TS-MMS scaffolds with nanoparticle drug delivery systems encapsulating rhodamine b installed via the solvent wetting method and sugar-particle adhesion method, respectively. A 546 nm excitation laser was directed onto the samples to enable rhodamine b fluorescence. (C) Confocal microscopy images of TS-MMS scaffold cross-sections with nanoparticle drug delivery systems encapsulating rhodamine b installed via the solvent wetting method and sugar-particle adhesion method, respectively. A 546 nm excitation laser was directed onto the samples to enable rhodamine b fluorescence. (D) Confocal microscopy z-stacked images of the TS-MMS scaffold cross-section with a nanoparticle drug delivery system encapsulating rhodamine b installed via the sugar-particle adhesion method.

To demonstrate the versatility of the sugar-particle adhesion method to install nanoparticles encapsulating other types of molecules for therapeutic delivery, PLGA nanoparticles encapsulating a large fluorescent-tagged protein, fluorescein isothiocyanate (FITC)-bovine serum albumin (BSA), were fabricated. A sugar sphere template made from the sugar-particle adhesion method with the PLGA nanoparticles encapsulating FITC-BSA was fabricated and z-stack imaged by confocal microscopy (**Figure 3.12A**). This revealed the presence and roughly homogenous

distribution of the PLGA nanoparticles encapsulating FITC-BSA around the macropores. However, it should be noted that the fluorescent signal did not appear as homogenous as the R6G fluorescent signal in **Figure 3.11B**, likely because the FITC-BSA is a significantly larger molecule than R6G and therefore could not be encapsulated into PLGA nanoparticles as densely, causing less fluorescent signal to be emitted. Furthermore, it is possible that the protein was aggregated in the PLGA nanoparticles, also causing a spatially non-uniform fluorescent signal.

TS-MMS scaffolds were made from the sugar-particle adhesion method with the PLGA nanoparticles encapsulating FITC-BSA and thinly sliced into cross-sections for confocal microscopy (**Figure 3.12A**). Similar to the sugar template, the TS-MMS scaffold with embedded nanoparticles encapsulating FITC-BSA demonstrated the presence of nanoparticles and fluorescent signal all around the macropores of the scaffold thin cross-section, but the fluorescent signal intensity randomly varied. More specifically, the fluorescent signal often appeared in bright dots and speckles, which suggests that the FITC-BSA was aggregating in some of the nanoparticles to produce intense fluorescent signal dots at the aggregates in the nanoparticles. This was considered to be insignificant because the nanoparticles encapsulating FITC-BSA were still distributed throughout the TS-MMS scaffold, and thus this experiment qualitatively proved that nanoparticles encapsulating proteins could be embedded into the TS-MMS scaffold.

It was additionally hypothesized that the fabrication procedure for the nanoparticle-sugar templates could lend itself to custom designing unique therapeutic spatial-distributions within a scaffold by spatially depositing different sugar spheres adhered to nanoparticles encapsulating different therapeutics. For example, a vertical sugar template with a nanoparticle-bilayer fabricated from a bottom sugar sphere layer adhered to PLGA nanoparticles encapsulating FITC-BSA and a top sugar sphere layer adhered to PLGA nanoparticles encapsulating R6G was designed to create

a spatial gradient bilayer of FITC-BSA and R6G (**Figure 3.12D**). The fabricated sugar template from this designed example and procedure was cross-sectioned and imaged by fluorescent microscopy and confocal microscopy (**Figure 3.12E**). Although the FITC-BSA green fluorescent signal was significantly weaker than the R6G red fluorescent signal, there was a visual gradient and bilayer in the color distribution of the fluorescent microscope image indicating that the PLGA nanoparticles encapsulating FITC-BSA were spatially separated from the PLGA nanoparticles encapsulating R6G. Confocal microscopy at the middle border of the sugar-nanoparticle bilayer confirmed this observation by identifying a distinct region where the FITC-BSA fluorescent signal ends and the R6G fluorescent signal begins with respect to moving vertically upward in the sugar template.

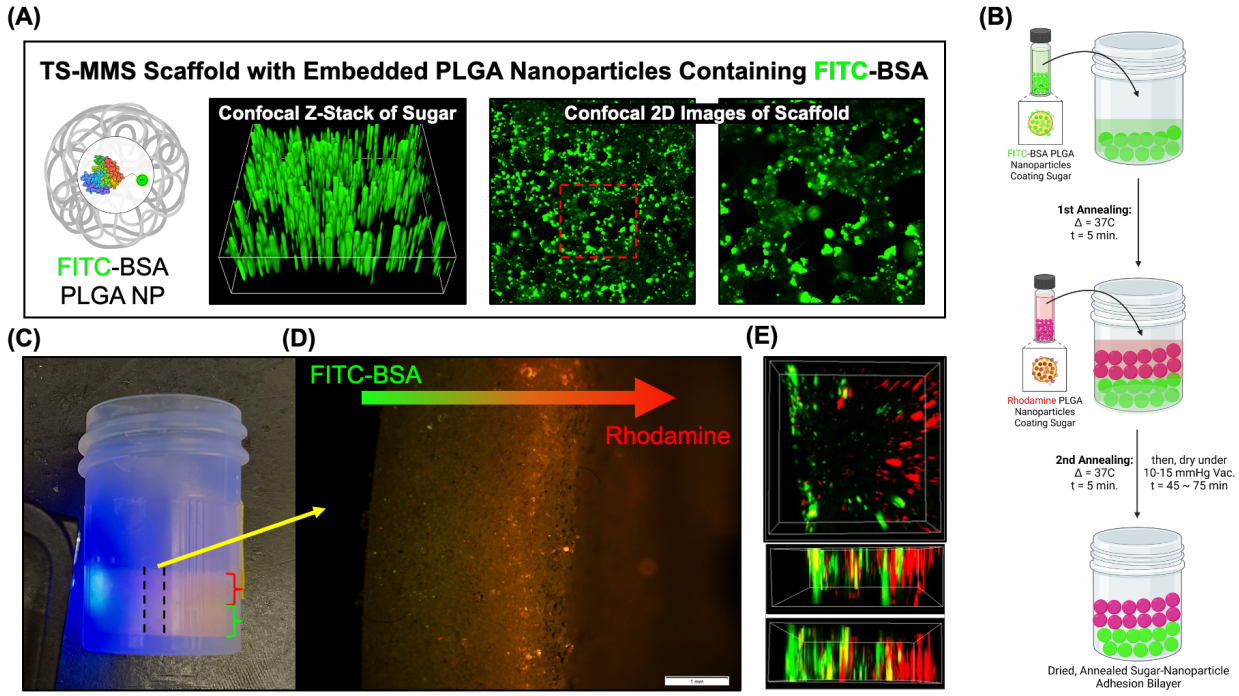

Figure 3.12: Scaffold and sugar fabrication with the sugar-particle adhesion method using PLGA nanoparticles encapsulating FITC-BSA and a bilayer sugar design for dual therapeutic release in spatially different parts of a scaffold. (A) A representative confocal z-stacked image of a sugar sphere template with adhered PLGA nanoparticles encapsulating FITC-BSA and confocal images of the TS-MMS scaffold fabricated from this sugar template. (B) Visual schematic for the design and procedure of a fabricating a sugar sphere template with a vertical biphasic distribution of

PLGA nanoparticles encapsulating rhodamine b and FITC-BSA. (C) Photograph of a dried, annealed sugar template with the biphasic nanoparticle distribution depicted in (B). (D) Fluorescent microscopy image of a cross-section of the sugar template from (C) displaying a left-to-right gradient of fluorescent signal from green to red corresponding to PLGA nanoparticles encapsulating FITC-BSA and rhodamine b nanoparticles, respectively. (E) Different rotations of a confocal microscopy z-stack image of the biphasic sugar sphere cross-section utilized in (D). Note that excitation lasers of 546 nm and 495 nm were directed onto the samples for (D) and (E).

It was important to confirm that the sugar-particle adhesion method was not affecting the nanofiber formation in the TS-MMS scaffolds, and furthermore, if the nanoparticles were physically encapsulated by nanofibers. To this end, TS-MMS scaffolds were fabricated with embedded PLGA nanoparticles encapsulating R6G using the sugar-particle adhesion method. These scaffolds were cross-sectioned, analyzed by SEM, and compared to a control group of TS-MMS scaffolds that did not contain a nanoparticle drug-delivery system (**Figure 3.13A,B**). The nanoparticle-embedded TS-MMS scaffold was observed to have homogenous nanofiber formation, but they were more textured and bumpier in comparison to the control TS-MMS scaffold nanofibers. The added texture was attributed to the embedded PLGA nanoparticles within the nanofibers of the TS-MMS scaffold fabricated using the sugar-particle adhesion method. In support of this, some of these nanoparticles could even be visualized during SEM if they were protruding through the surface of the nanofiber and not completely embedded within it.

Confirming that the nanoparticles were embedded within and on the surface of the nanofibers homogenously throughout the TS-MMS scaffold provided preliminary insight into the possible mechanism and kinetics of drug-delivery from the scaffold (**Figure 3.13C**). It was hypothesized that the nanoparticles would slowly be released as the nanofibers of the TS-MMS scaffold hydrolyzed, and that nanoparticles would be released in the order of how close they are to the surface of the degrading nanofiber. After a nanoparticle was released or exposed to the aqueous surrounding, it would rapidly degrade to release the therapeutic agent since PLGA hydrolyzes on

the timescale of days. This mechanism of scaffold therapeutic delivery predicts a sustained release of therapeutics over time on both the order of an individual nanofiber and the order of an entire scaffold as the immediate surface of the scaffold macropores will degrade before the material underneath.

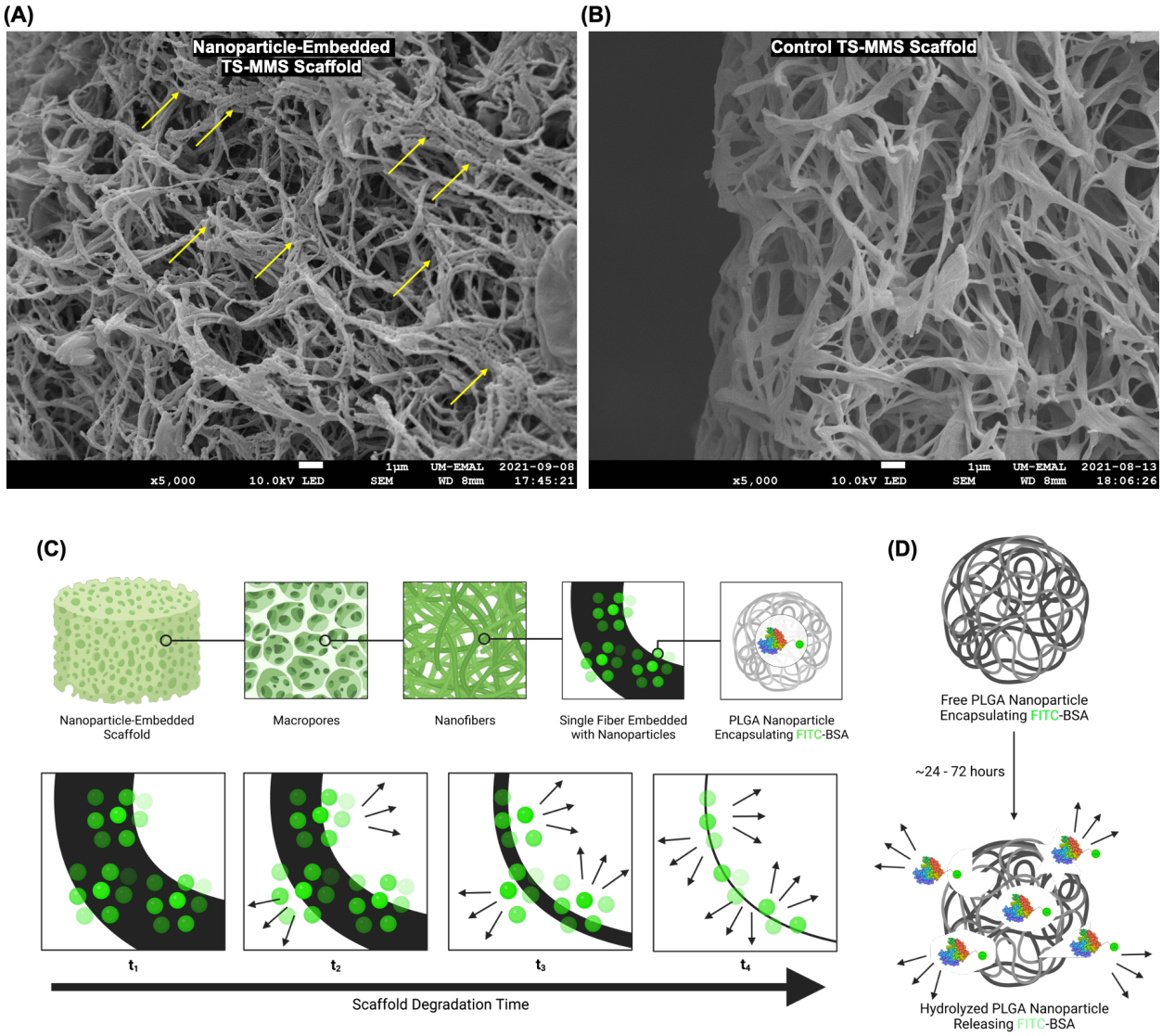

Figure 3.13: Nanofiber characterization of TS-MMS scaffolds with an embedded nanoparticle drug delivery system installed via the sugar-particle adhesion method and the hypothesized hydrolytic mechanism of sustained therapeutic release from the nanofibers. (A) Representative scanning electron microscopy image of the nanofibers for a TS-MMS scaffold with embedded PLGA nanoparticles encapsulating FITC-BSA installed via the sugar-particle adhesion method. (B) Representative scanning electron microscopy image of the nanofibers of a control TS-MMS

scaffold without a drug delivery system. (C) Visual schematic of the hypothesized mechanism of sustained nanoparticle and therapeutic release through the gradual degradation of the nanofibers containing the embedded nanoparticle drug delivery system. (D) Visual schematic of the PLGA nanoparticle hydrolysis to release the encapsulated therapeutics.

The TS-MMS scaffold embedded drug delivery system was investigated for its sustained release via a release kinetics experiment whereby the TS-MMS scaffolds were allowed to gradually degrade in PBS at 37C to release rhodamine b from the embedded PLGA nanoparticles (**Figure 3.14A**). The PBS supernatant of each sample was collected at each time point and measured for its fluorescent intensity as an indicator of rhodamine b concentration released from the TS-MMS scaffold with an embedded drug delivery system (**Figure 3.14A**). These mean fluorescent measurements were cumulatively added to the prior sum mean fluorescent intensity to create a plot of cumulative rhodamine b release from the TS-MMS scaffold (**Figure 3.14B**). These results demonstrated that the TS-MMS scaffolds sustained release at least for the duration of 40 days, but were projected by a nonlinear regression curve fit for logistic growth to continue releasing rhodamine b for approximately 90 days (**Figure 3.14B**). Ultimately, this experiment successfully demonstrated the sustained release mechanism of the TS-MMS scaffold with an embedded nanoparticle drug delivery system, hypothesized by the mechanism in **Figure 3.13C**.

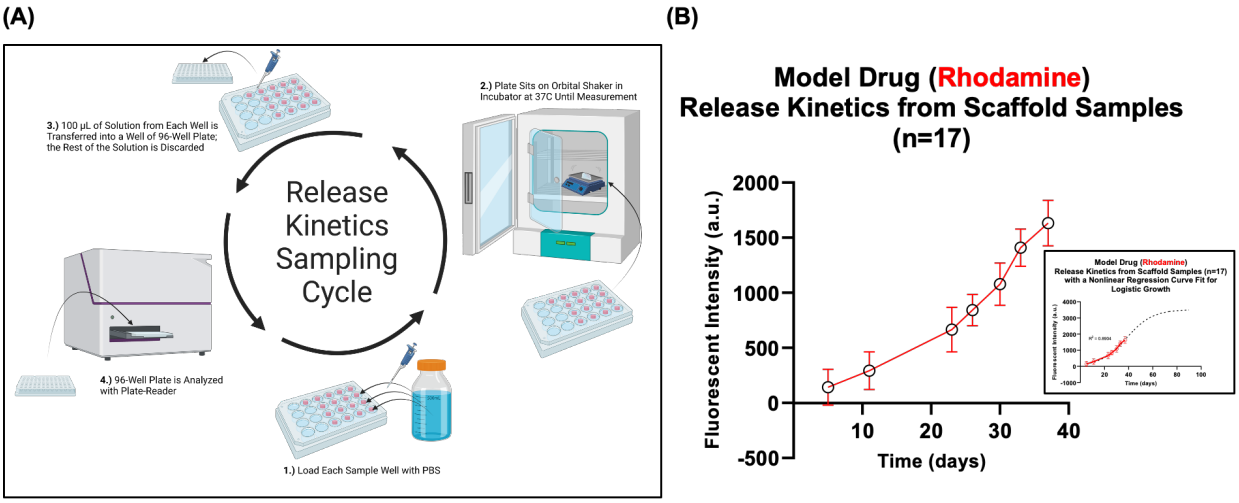

Figure 3.14: Release kinetics experiment from a TS-MMS scaffold with an installed PLGA nanoparticle drug delivery system encapsulating rhodamine b installed via the sugar-particle adhesion method. (A) Visual schematic of the experimental setup and supernatant collection cycle to quantify the scaffold release kinetics of rhodamine b at each time point. (B) Scatter plot of the measured cumulative mean fluorescent intensities of rhodamine b in the supernatant of the collected release test samples for every time point of collection. This is a measure of how much total rhodamine b has been released at every time point. Error bars are depicted as the propagated measured standard deviation for the cumulative mean fluorescent intensity at each time point. The right-hand graph is a nonlinear regression curve fit for logistic growth fitting these data points.

3.3.3 Biological Proof-of-Concept of TS-MMS Scaffold with Drug Delivery

The biological efficacy of the drug delivery system and the macropore shape memory of the TS-MMS scaffolds sought to be evaluated *in-vivo*. PLLA, TS-MMS, and TS-MMS scaffolds with an embedded nanoparticle drug delivery system encapsulating simvastatin, a known angiogenesis promoter, were fabricated;[3,6] half of these scaffolds were kept as virgin controls and the other half were subject to a whole thermal cycle as done in **Figure 3.9A** to significantly deform the scaffolds by a 50% compression and allow them to recover their macropores via thermosensitive shape memory. These scaffolds were then subcutaneously implanted in mice using a common subcutaneous scaffold implant model procedure, and the mice were allowed to recover for two weeks and four weeks before the scaffolds were explanted for investigation. It should be noted that

the mice were all genetically modified with the Col1GFP gene such that any cell in the mouse expressing osteoblastic gene phenotypes also expressed green fluorescent protein, and could be fluorescently visualized as green on the visible light spectrum. Additionally, these mice were all modified with the LysMCre and tdTomato gene such that any cell expressing a macrophage phenotype in the mouse also expressed tdTomato red fluorescent protein that could be visualized with fluorescence as red on the visible light spectrum.

The explanted scaffolds after two weeks were first visualized by confocal microscopy (**Figure 3.15A-D**). As expected, the deformed PLLA scaffolds had a large void in the center where there was no biological activity (**Figure 3.15A**). This was observed because the PLLA scaffolds had no mechanism of macropore shape memory to recover their spherical, open macropores during the recovery process after deformation. Thus, the cells from the surrounding mice tissues could not deeply penetrate the deformed PLLA scaffold with the compromised macropores. On the contrary, the TS-MMS deformed and virgin scaffolds both exhibited cell penetration throughout the entirety of the scaffold (**Figure 3.15A-C**). This again proved that the TS-MMS scaffolds could recover their macropores after a deformation upon reheating above 50C, and that this macropore recovery was biologically significant. It is also noteworthy to mention that the TS-MMS scaffolds exhibited a significantly higher density of osteoblasts throughout their macropores compared to the PLLA scaffold equivalents (**Figure 3.15C**). This is potentially because the reduced compressive and tensile moduli of the TS-MMS scaffold and the TSM biomaterial are more favorable for osteogenic differentiation of skeletal stem cells from a mechanobiology standpoint. PLLA is a highly rigid and stiff material whereas the TSM biomaterial is much more rubbery and less stiff, which may more closely resemble the extracellular matrix of trabecular bone that is highly conducive to osteogenesis and differentiation into osteoblastic fates. Finally, it is noteworthy to observe that the

TS-MMS scaffolds both had slightly more macrophages than the PLLA equivalents, suggesting that they were creating microvasculature at this time point.

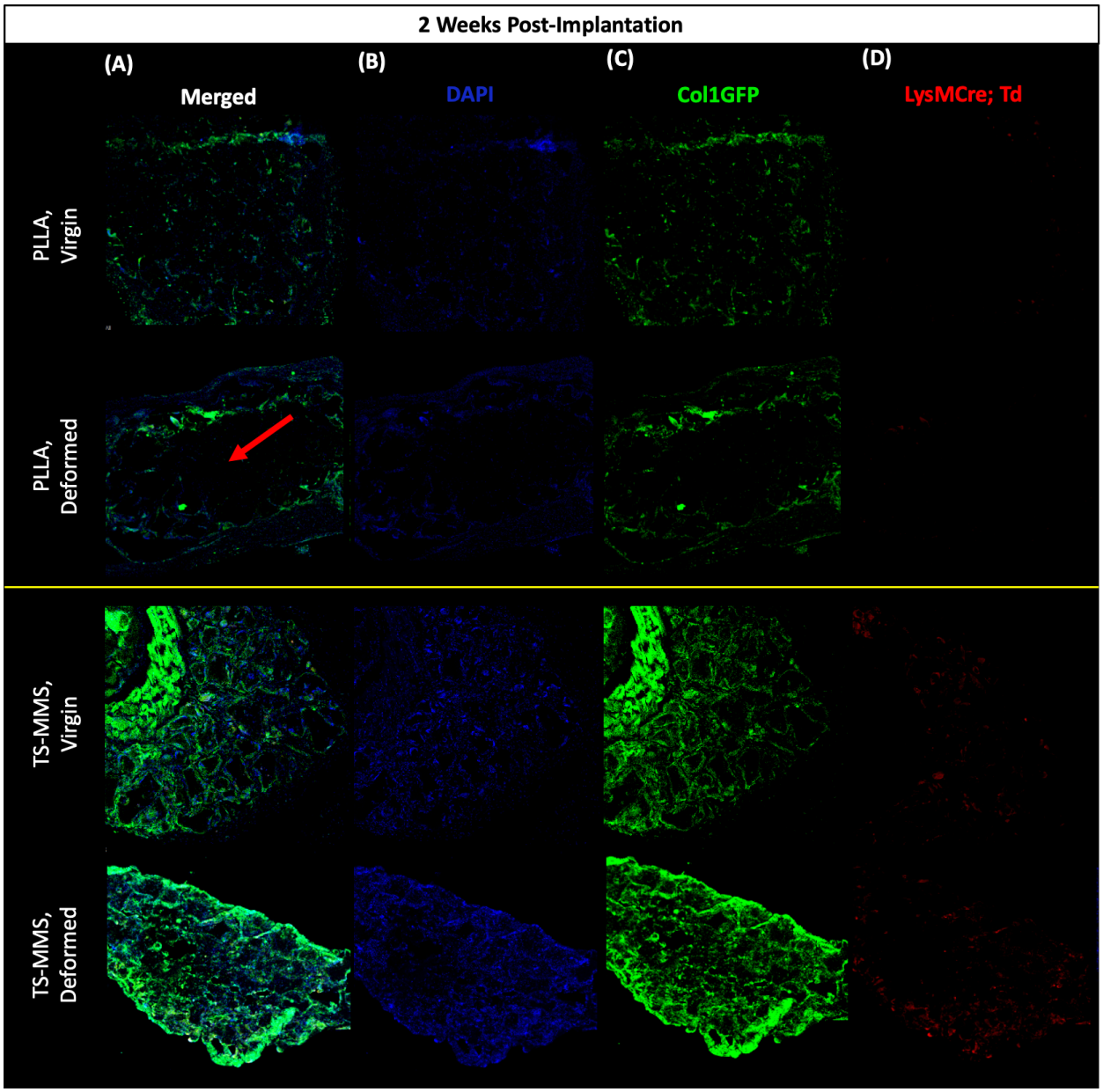

Figure 3.15: Confocal microscopy of the histology from the subcutaneous scaffold implant *in-vivo* experiment, 2 weeks post-implantation. (A) Representative confocal microscopy images of the explanted scaffold histology results using the merged laser channels from (B-D). Red arrow points to void with no signal in the deformed PLLA scaffold, which is due to its mechanically compressed macropores. (B) Representative confocal microscopy images of the explanted scaffold histology results after staining the cell nuclei with DAPI. This channel uses a 358 nm laser to excite the DAPI stain causing fluorescence in the blue visible light spectrum, where each dot

represents a cell nucleus. (C) Representative confocal microscopy images of the explanted scaffold histology results of osteoblast distribution within the scaffold using Col1GFP genetically-modified mice that express green fluorescent protein (GFP) in cells expressing an osteoblastic phenotype. This channel uses a 488 nm laser to excite the green fluorescent proteins causing fluorescence in the green visible light spectrum, where regions of intense green fluorescence represent high cell densities of osteoblasts. (D) Representative confocal microscopy images of the explanted scaffold histology results of macrophage distribution within the scaffold using LysMCre and tdTomato genetically-modified mice that express tdTomato, a red fluorescent protein, in cells expressing a macrophage phenotype. This channel uses a 554 nm laser to excite the tdTomato fluorescent proteins causing fluorescence in the red visible light spectrum, where regions of intense red fluorescence represent high cell densities of macrophages.

The explanted scaffolds after four weeks continued the previously observed trends and patterns for the PLLA and TS-MMS scaffolds that were imaged in **Figure 3.15**. The four week explanted scaffolds had the addition of the TS-MMS scaffolds with embedded nanoparticles encapsulating simvastatin for sustained, controlled release (TS-MMS + SIM). The TS-MMS + SIM virgin and deformed groups demonstrated higher cell densities throughout the macropores than the other scaffolds, suggesting that the simvastatin controlled release promoted chemotaxis and angiogenesis into the scaffolds. This hypothesis is defended by the observation of a higher macrophage cell density and presence within the TS-MMS + SIM scaffolds since macrophages are intricately involved with blood vessel vasculature formation and remodeling. Ultimately, the confocal microscopy results from these groups confirmed that the TS-MMS scaffolds succeeded in recovering their macropores in a biologically relevant manner and that the simvastatin controlled release further promoted the efficacy of the TS-MMS scaffolds with respect to integrating with the nearby tissue and promoting cell migration into the scaffold. Additionally, the TS-MMS scaffolds with and without simvastatin release were observed to have higher densities of osteoblasts, suggesting that osteogenesis was being promoted within the scaffolds.

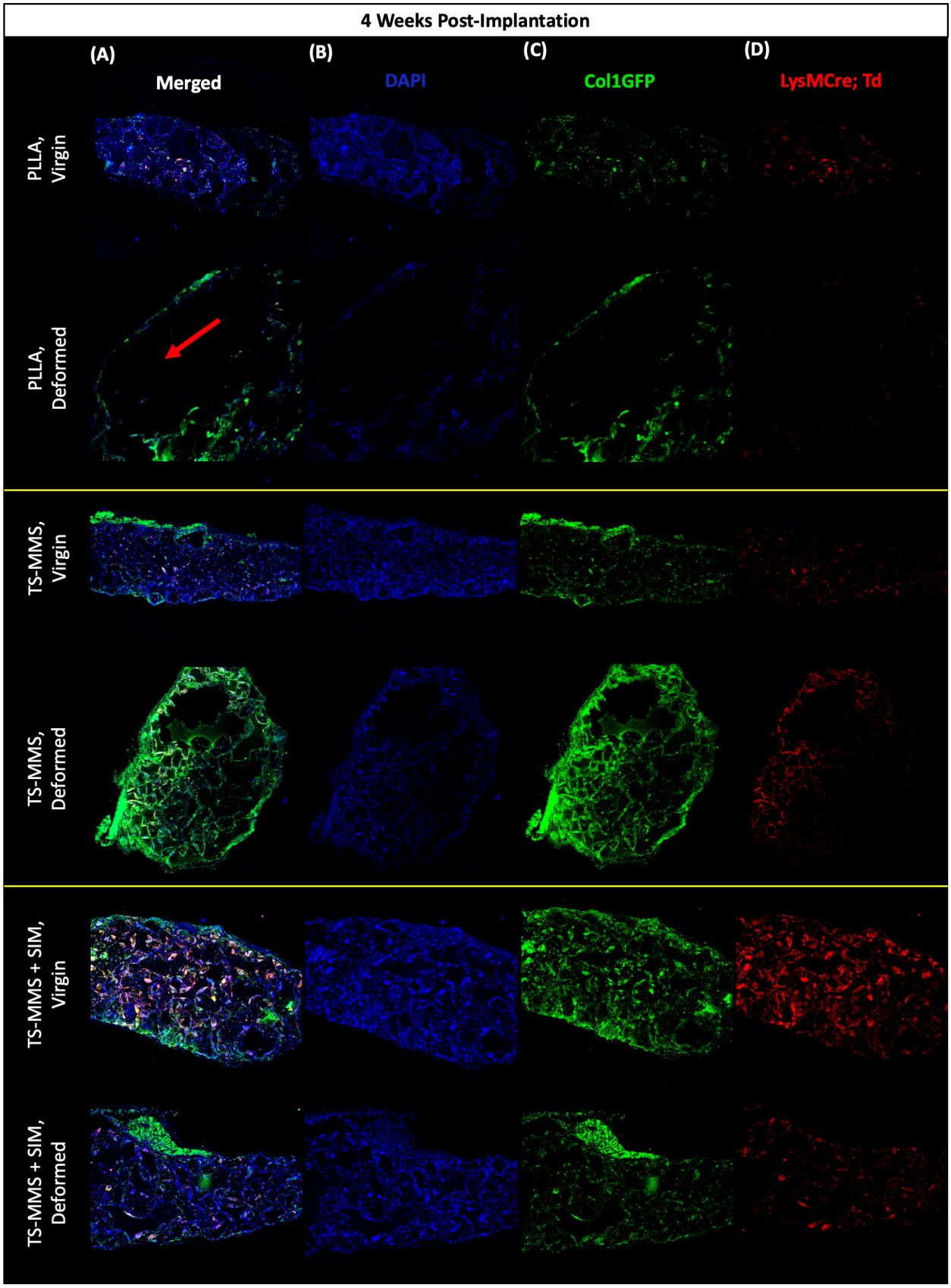
4 Weeks Post-Implantation
(A)
Merged
(B)
DAPI
(C)
Col1GFP
(D)
LysMCre; Td
PLLA, Virgin
PLLA, Deformed
TS-MMS, Virgin
TS-MMS, Deformed
TS-MMS + SIM, Virgin
TS-MMS + SIM, Deformed

Figure 3.16: Figure 3.15: Confocal microscopy of the histology from the subcutaneous scaffold implant *in-vivo* experiment, 4 weeks post-implantation. Note that TS-MMS + SIM represents TS-MMS scaffolds with embedded PLGA nanoparticle drug delivery systems encapsulating simvastatin for sustained release. (A) Representative confocal microscopy images of the explanted scaffold histology results using the merged laser channels from (B-D). Red arrow points to void with no signal in the deformed PLLA scaffold, which is due to its mechanically compressed macropores. (B) Representative confocal microscopy images of the explanted scaffold histology results after staining the cell nuclei with DAPI. This channel uses a 358 nm laser to excite the DAPI stain causing fluorescence in the blue visible light spectrum, where each dot represents a cell nucleus. (C) Representative confocal microscopy images of the explanted scaffold histology results of osteoblast distribution within the scaffold using Col1GFP genetically-modified mice that express green fluorescent protein (GFP) in cells expressing an osteoblastic phenotype. This channel uses a 488 nm laser to excite the green fluorescent proteins causing fluorescence in the green visible light spectrum, where regions of intense green fluorescence represent high cell densities of osteoblasts. (D) Representative confocal microscopy images of the explanted scaffold histology results of macrophage distribution within the scaffold using LysMCre and tdTomato genetically-modified mice that express tdTomato, a red fluorescent protein, in cells expressing a macrophage phenotype. This channel uses a 554 nm laser to excite the tdTomato fluorescent proteins causing fluorescence in the red visible light spectrum, where regions of intense red fluorescence represent high cell densities of macrophages.

H&E staining was additionally performed on the histology slices of the explanted scaffolds at four weeks to qualitatively observe the different tissue and cell types that were colonizing the scaffolds. All of the scaffolds were observed to be promoting skeletal stem cell and proginetor growth, but to varying degrees and maturities. The deformed PLLA scaffold had hardly any cell or extracellular matrix maturity, and very low cell density within the scaffold due to the compromised macropores (**Figure 3.17A**). The TS-MMS virgin scaffold was observed to have a slightly higher cell density than the deformed scaffold, but there was still cell presence throughout both TS-MMS scaffolds (**Figure 3.17B**). The TS-MMS scaffolds with simvastatin controlled release were observed to have very mature cell and extracellular matrix formations, supporting the hypothesis that the simvastatin was promoting migration and blood vessel formation within the TS-MMS scaffolds (**Figure 3.17C**).

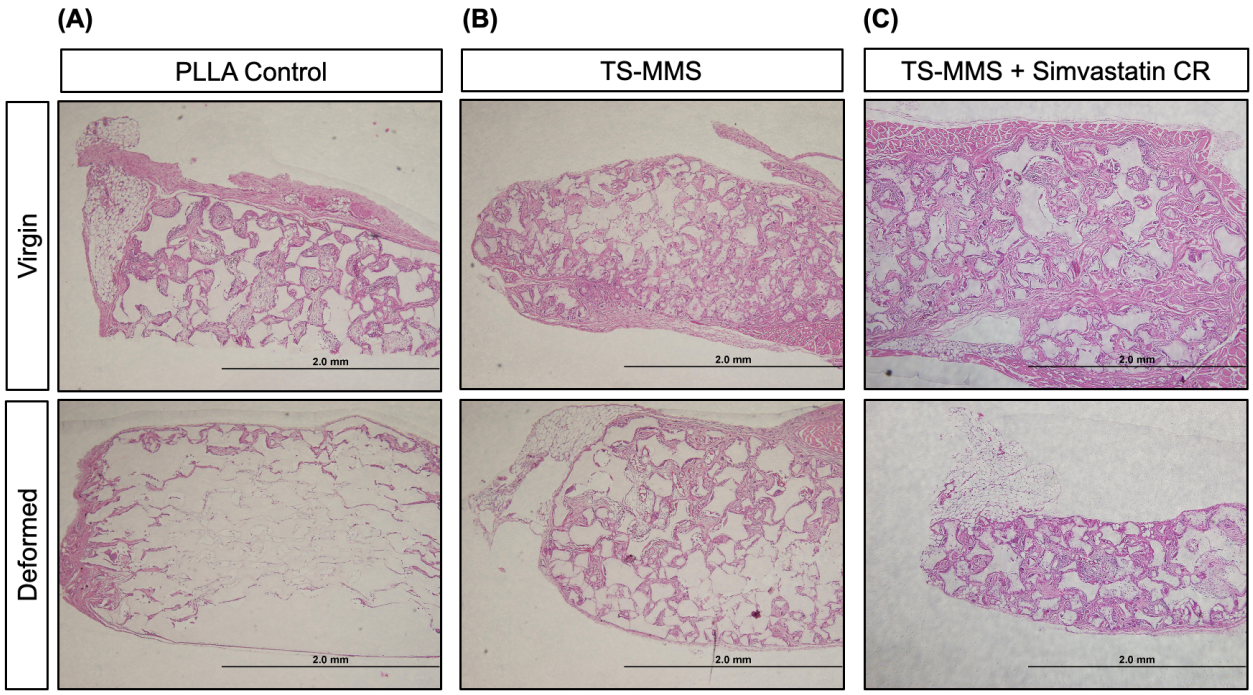

Figure 3.17: H&E staining results of the histology from the subcutaneous scaffold implant *in-vivo* experiment, 4 weeks post-implantation. (A) Representative wide field microscopy images of the explanted PLLA scaffold histology results stained with H&E for the virgin and 50% compression deformed then recovered scaffolds, respectively. Note that the PLLA scaffold does not recover its macropores after deformation. (B) Representative wide field microscopy images of the explanted TS-MMS scaffold histology results stained with H&E for the virgin and 50% compression deformed then recovered scaffolds, respectively. (C) Representative wide field microscopy images of the explanted TS-MMS scaffold with simvastatin controlled release (CR) histology results stained with H&E for the virgin and 50% compression deformed then recovered scaffolds, respectively.

To further investigate the formation of microvasculature within the explanted scaffolds, the histology slices for the scaffolds were stained with CD31 to visualize the 2D cross-sections of blood vessels. Blood vessels were observable in the virgin PLLA scaffold and both TS-MMS scaffolds after two weeks post-implantation (**Figure 3.18A**). Furthermore, not many blood vessels or cell migration into the scaffold was observed in the deformed PLLA scaffold, suggesting that the open, spherical macropores of the virgin PLLA and both TS-MMS scaffolds allowed for vascular penetration into the scaffold. These trends continued into the four week post-implantation

time point, with the exception of the added TS-MMS scaffolds with simvastatin controlled release. The TS-MMS + simvastatin CR group was observed to have significant microvasculature in the deformed and virgin scaffolds, suggesting that the macropores did recover their shape and that the scaffold did release simvastatin into the local environment to promote angiogenesis (**Figure 3.18B**). Ultimately, these experiments demonstrated that microvasculature formation was not dependent solely on simvastatin, but that open macropores were one of the most significant contributors to microvascular formation and that the simvastatin controlled release assisted this process.

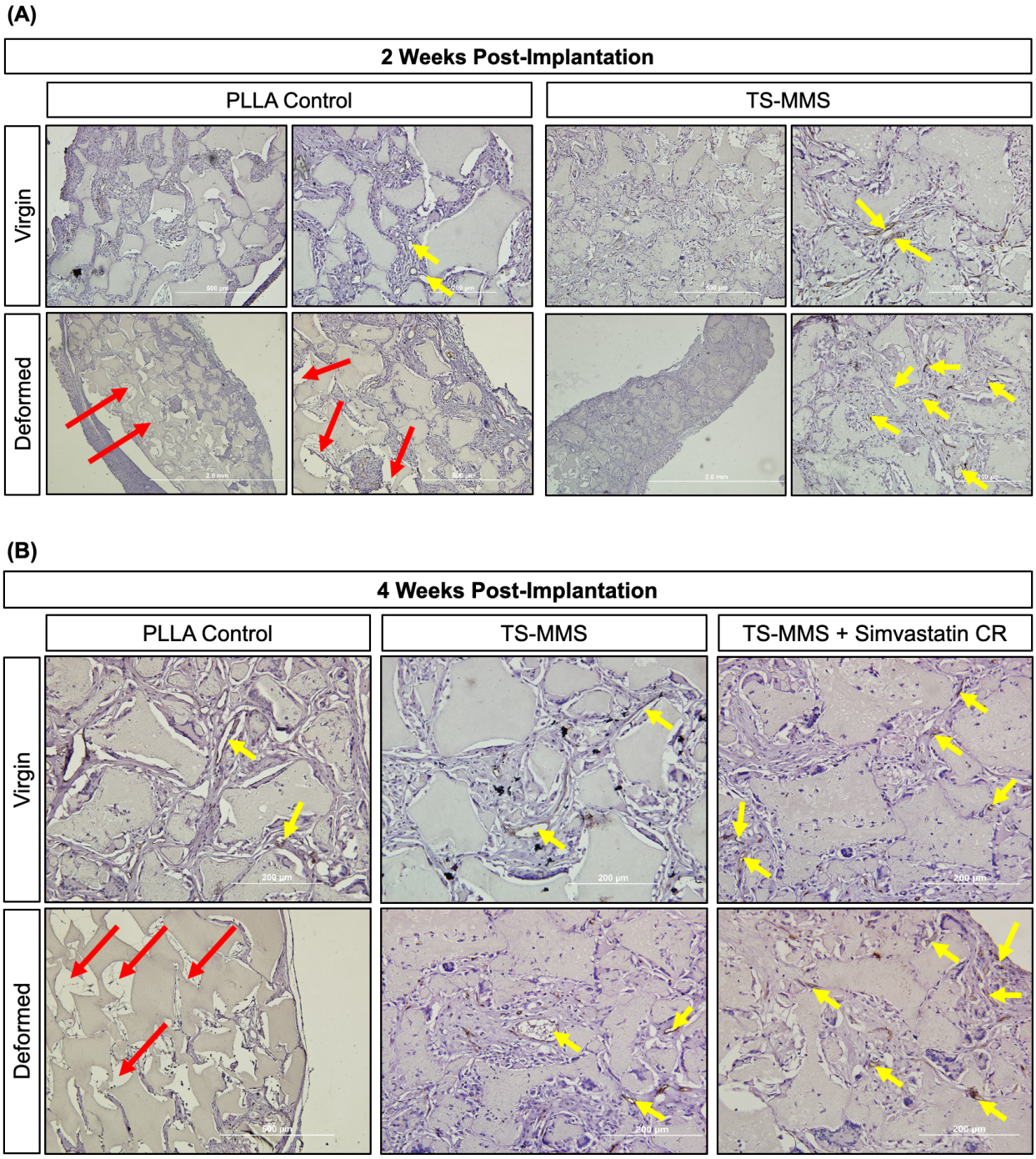

Figure 3.18: CD31 staining results of the histology from the subcutaneous scaffold implant *in-vivo* experiment showing where there is blood vessel vasculature. (A) Representative wide field microscopy images of the explanted scaffold histology results after 2 weeks post-implantation. (B) Representative wide field microscopy images of the explanted scaffold histology results after 4 weeks post-implantation. Yellow arrows point to areas of blood vessel vasculature and red arrows point to a lack of vasculature and tissue.

The final biological characterization performed on the explanted scaffolds was PSR staining of the four weeks post-implantation scaffolds to visualize collagen maturity. The deformed PLLA scaffold was observed to have no collagen in the center due to a lack of cell migration into the crushed macropores (**Figure 3.19A**). The virgin PLLA scaffold and both TS-MMS scaffolds were observed to have mostly immature collagen present throughout the scaffold showing early signs of extracellular matrix remodeling (**Figure 3.19A,B**). However, the TS-MMS scaffolds with simvastatin controlled release had significantly more collagen and more mature collagen than the other groups, suggesting that the simvastatin helped promote microvasculature and created a sufficient chemical environment to stimulate extracellular matrix remodeling and tissue maturation. This agrees with the results of the H&E stain in **Figure 3.17** and ultimately suggests that the simvastatin controlled release was promoting osteogenesis more than the other scaffolds. Ultimately, these *in-vivo* experiments demonstrated the biological efficacy and importance of the TS-MMS scaffolds and the embedded drug delivery systems toward guiding microvasculature, cell migration into and throughout the scaffold, and tissue maturation within the scaffold.

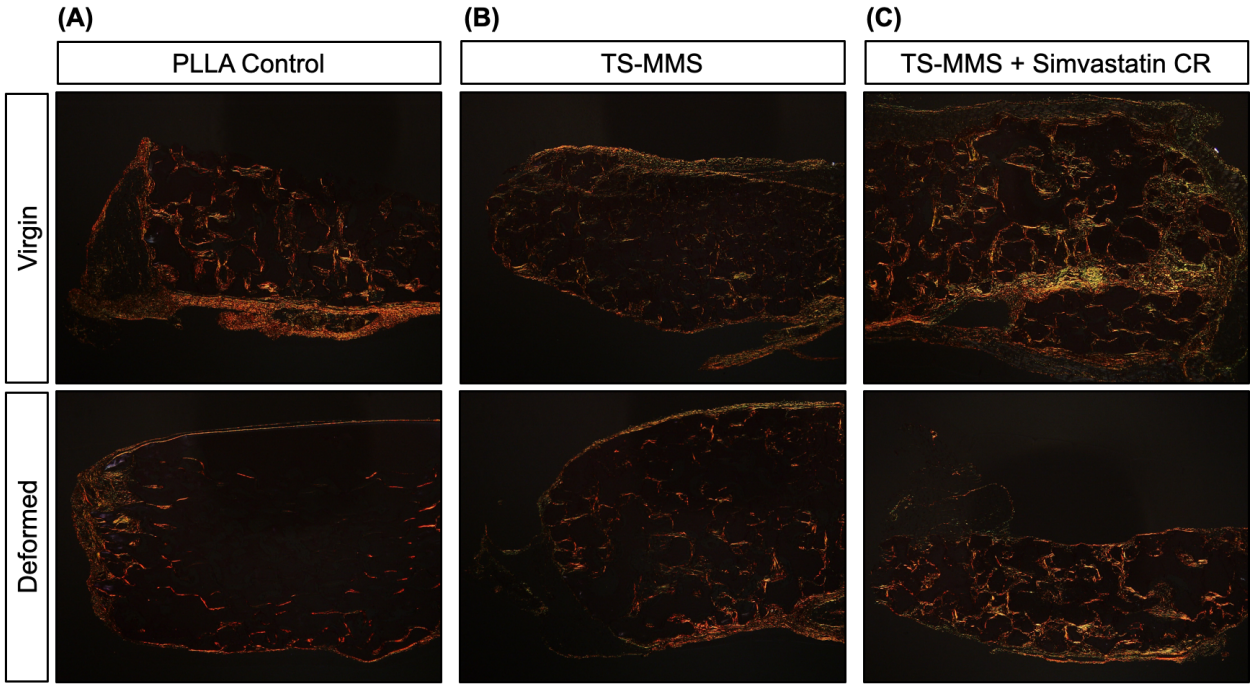

Figure 3.19: PSR staining results of the histology from the subcutaneous scaffold implant *in-vivo* experiment showing collagen maturity in the scaffolds, 4 weeks post-implantation. (A) Representative bright field microscopy images of the explanted PLLA scaffold histology results after staining the collagen extracellular matrix with PSR for the virgin and 50% compression deformed then recovered scaffolds, respectively. (B) Representative bright field microscopy images of the explanted TS-MMS scaffold histology results after staining the collagen extracellular matrix with PSR for the virgin and 50% compression deformed then recovered scaffolds, respectively. (C) Representative bright field microscopy images of the explanted TS-MMS scaffold with simvastatin controlled release (CR) histology results after staining the collagen extracellular matrix with PSR for the virgin and 50% compression deformed then recovered scaffolds, respectively.

3.4 Conclusion

This chapter utilized the TSM biomaterial introduced in chapter 1 and created a novel TS-MMS scaffold presenting a homogenous, nanofibrous morphology capable of thermosensitive shaping and thermosensitive macropore shape memory. This scaffold was optimized and characterized for its ability to be shaped and to recover its spherical macropores using thermal heat. Furthermore, a nanofiber-embedded nanoparticle drug delivery system was incorporated into the scaffold using a novel sugar-particle adhesion method which homogenously distributed

nanoparticles throughout the scaffolds, presenting a significant upgrade to the currently used solvent wetting method for installing nanoparticles onto a scaffold. The release from this drug delivery system was observed to be sustained for up to 40 days. Finally, these novel contributions to scaffolds were demonstrated *in-vivo* using TS-MMS scaffolds and TS-MMS scaffolds with a drug delivery system for simvastatin. The TS-MMS scaffolds were observed to recover their macropores significantly enough to be biologically effective at promoting cell migration, adhesion, microvascular formation, and osteogenesis; however, the TS-MMS scaffolds with simvastatin release ultimately presented the most significant advances in these areas as observed from the highly mature tissue and extracellular matrix that formed within those scaffolds. Future directions need to investigate the TS-MMS scaffolds at regenerating bone and promoting mineralization. Additionally, future studies should utilize different drug therapies installed into scaffolds with the sugar-particle adhesion method. Finally, there needs to be a true *in-vivo* macropore recovery experiment to confirm if recovering the scaffold macropores *in-vivo* is viable.

3.5 Materials and Methods

Materials and Reagents: Resomer 207S poly (L-lactic acid) was purchased from Evonik. All other reagents were purchased from Sigma Aldrich unless specifically mentioned in the below methods. Reagents were used as received unless otherwise specified.

Synthesis of Poly-ε-Caprolactone (PCL-diol): In the preparation of poly-ε-caprolactone (MW = ~10 kDa), 10 mL of ε-caprolactone monomer was added into a 50 mL round-bottom flask along with 89 μL of 1,4-butanediol (1 mol eq). Catalytic amounts (6.5 μL, 0.01 mol eq) of tin(II) 2-ethylhexanoate ($Sn(Oct)_2$) were added to a round-bottom flask with magnetic stir bar. The resulting

solution was stirred at a low speed under vacuum, and heated to 120C and maintained for 12 hours resulting in a highly viscous solution. The reaction mixture was cooled to room temperature to form a white solid. A minimum volume of dichloromethane (DCM) was added to dissolve the white solid; the resulting solution was precipitated into 300 mL of methanol (~5x volume) at 0C yielding a white solid. This solution was then centrifuged (3,500 rpm x 10 min) to concentrate the solid and remove the supernatant. This precipitation procedure was repeated three times to remove unreacted monomer and catalyst. The solid, PCL-diol, was allowed to dry for two days in a vacuum chamber and stored at -20C before further use. Molecular weight was assessed by gel permeation chromatography (GPC) in tetrahydrofuran (THF) solvent. Molecular characterization is performed by nuclear magnetic resonance spectroscopy (NMR, CDCl3) and Fourier-transformed infrared spectroscopy (FTIR).

Synthesis of Poly-ε-Caprolactone Diacrylate (PCL-DA): PCL-diol was functionalized with terminal acrylate functional groups to impart cross-linking ability. 5 g of PCL (MWavg = 10.47 kDa by GPC) was added to a 50 mL round-bottom flask and dissolved in a minimum volume of anhydrous DCM. 135 µL of triethylamine (TEA, 2 mol eq) was added with stirring at moderate speed (~500 rpm). After 15 minutes, 78 µL of acryloyl chloride (AC) was added dropwise into the solution over the course of 10 minutes using a syringe. The reaction was left to proceed overnight under moderate stirring, warming to room temperature as the ice bath melted. The resulting reaction mixture was precipitated into 300 mL of methanol (~5x vol) at 0C in a beaker to precipitate a white solid. This solution was then centrifuged (3,500 rpm x 10 min) to concentrate the solid and remove the supernatant. This precipitation procedure was repeated three times to remove unreacted AC and remove TEA. The solid PCL-DA was allowed to dry for two days in a

vacuum chamber and stored at -20C before further use. End group functionalization was confirmed by NMR (CDCl3) and FTIR.

Synthesis of Poly Lactic-co-Glycolic Acid (PLGA): In the preparation of poly lactic-co-glycolic acid (50:50 lactide-glycolide ratio, MW ~ 10,000 Da), *L*-lactide (7.6 mmol, 1.10 g, 1 mol eq) and ε-caprolactone (7.6 mmol, 0.88 g, 1 mol eq) were added to a round-bottom flask with benzyl alcohol (initiator, 0.2 mmol, 208 μL, 0.027 mol eq). The reaction was heated 120C under vacuum with moderate stirring then 100 μL of $Sn(Oct)_2$ (catalyst, 0.001 mol eq) was injected. After twelve hours, the reaction was opened to air and allowed to cool to room temperature resulting in a colorless solid. A minimum volume of DCM (approximately 20-30 mL) was used to completely dissolve this solid, and the resulting solution was precipitated into 300 mL of -20C methanol (10x vol eq) resulting in a white solid. The supernatant was poured off and the PLGA was dried for two days in a vacuum chamber and stored at -20C before further use. This precipitation procedure was repeated three times. The solid PLGA was allowed to dry for two days in a vacuum chamber and stored at -20C before further use. Chemical identity and lactide-glycolide ratio was confirmed by NMR (CDCl3) and FTIR. Molecular weight was determined by GPC.

Controlled Diameter Sugar Sphere Fabrication: Sugar spheres of a controlled diameter were fabricated to serve as a porogen template for scaffold polymer casting using a previously described method (add citation). Briefly, D-fructose as melted in an oven and emulsified in hot mineral oil containing 2% v/v Span80 surfactant. The emulsion mixture was quenched in an ice bath, stirring at 800 rpm. Once cool, the mineral oil solution was exchanged for hexanes five times until the supernatant was fully transparent, to remove mineral oil and Span80. Sugar spheres were separated

by size using molecular sieves (425 um, 250 um; Newark Wire Cloth Co, Newark NJ) and collected in vials containing hexanes, and stored at 4C until further use. Subsequent steps carried out under sufficient volumes of hexanes to prevent exposure of the sugar spheres to moisture.

Fabrication of Nanofibrous PLLA Scaffold: Nanofibrous, macroporous three-dimensional tissue engineering scaffolds made of PLLA were fabricated using a previously described sugar sphere porogen and thermally induced phase separation method. Briefly, sugar spheres of a uniform, selected diameter were added to cylindrical Teflon mold filled with hexane. The sugar spheres were annealed for 7 minutes at 37C . The hexane supernatant was removed and the sugar sphere template was placed in a vacuum chamber to evaporate the remaining solvent at 12-14 mmHg for approximately 60 minutes. Meanwhile, a PLLA polymer solution was prepared in THF at 10% w/v and warmed to 62C to dissolve completely. Once the sugar sphere templates were dry and the PLLA was dissolved, 0.8 – 1.2 mL of warm PLLA solution was quickly poured into each Teflon mold. The molds were transferred back into the vacuum and subjected to three rapid vacuum cycles to ensure the viscous polymer solution fully penetrated the sugar sphere template. The resulting scaffolds were immediately transferred to -80C freezer for 48 hours to induce thermally induced phase separation (TIPS) of the PLLA from THF, resulting in nanofiber formation throughout the scaffold. After 48 hours, the Teflon molds with the scaffolds were transferred to hexane on an orbital shaker set at 80 rpm for 1 day before the hexane solvent was discarded. The scaffolds were removed from the Teflon molds and submerged in distilled water to dissolve the sugar spheres. After 1 day in water on the orbital shaker set at 80 rpm, the scaffolds were cut and stored at -80C until further use.

Synthesis of Nanofibrous, Thermosensitive Memorized Microstructure (TS-MMS) Scaffolds: Nanofibrous, macroporous three-dimensional tissue engineering scaffolds a similar procedure. In essence, a low molecular weight PCL-DA (~10 kDa) was crosslinked within a high molecular weight PLLA matrix to synthesize a semi-interpenetrating mesh (semi-IPM) within the PLLA. First, a solution of a specified w/w ratio of PCL-DA to PLLA (for example, 40% PCL-DA/60% PLLA) was constituted in THF at 15% total polymer w/v, and heated to 62C to completely dissolve. Separately, sugar sphere templates were prepared in Teflon molds as described. A 3 mM stock solution of Irgacure® 2959 photoinitiator was prepared in methanol. When the sugar templates were dried and the polymer solution was dissolved, 1.7% v/v ratio photoinitiator stock solution was injected into the polymer solution (170 μL photoinitator per 10 mL of polymer solution). The resulting solution was quickly stirred and poured into the Teflon molds with the sugar sphere templates (0.8 – 1.2 mL of solution per sugar sphere template). The polymer solution penetrated the sugar spheres by the vacuum cycling and subjected to UV-induced crosslinking (FisherScientific® UV Crosslinking Chamber , λ = 256 nm) at E = 10 J for up to 10 minutes. After this time elapsed, the Teflon molds were rapidly transferred into a -80C freezer for 2 days to induce TIPS. Subsequent steps are the same as in the PLLA scaffold fabrication procedure. TS-MMS scaffolds were stored at -80C until further use.

Encapsulated-Rhodamine PLGA Nanoparticle Fabrication: Nanoparticles were prepared by a w/o/w double emulsion method with rhodamine b as a model small-molecule drug. Briefly, 15 mg of rhodamine b was dissolved in 500 μL (X mM) of distilled water (ddH_2O). Separately 250 mg of PLGA (50:50, MW = 7-17kDa, Sigma #) was dissolved in 1.50 mL of DCM (X mg/mL) in a 50 mL Falcon Tube. Both solutions were kept on ice once fully dissolved. 160 μL of the drug

solution was added to the PLGA solution and sonicated by a probe sonicator for 35 s on ice to create a w/o emulsion (X kV power). Immediately after, the w/o solution was poured into 5 mL of 1% w/v polyvinyl alcohol in distilled water on ice and the resulting solution was sonicated by the probe sonicator for 35 s on ice, resulting in the w/o/w emulsion. The w/o/w emulsion was transferred into to a 20 mL glass vial, washing the Falcon Tube with distilled water (diH_2O) to maximize particle yield. The w/o/w emulsion was stirred at 1300 rpm overnight in a fume hood to allow for organic solvent evaporation. The nanoparticles were concentrated and washed of the PVA and excess drug by 6 rounds of centrifugation at 9000 rpm for 20 min at 5 C, each, refreshing diH_2O between rounds. Particles were reconstituted in ddH2O and lyophilized and stored at -20 C until further use.

Encapsulated-Simvastatin PLGA Nanoparticle Fabrication: Nanoparticles were prepared by a w/o/w double emulsion method with simvastatin. First, a 38 mM simvastatin stock solution was prepared by constituting simvastatin (40 mg, 9.6 μmol) in 1 mL of ethanol and 1.5 mL of 1 M NaOH. The resulting solution was heated at 50C for 2 hours until clear and then neutralized to pH 7 with HCl. Separately, 100 mg of PLGA (50:50, MW = 7-17kDa, Sigma) was dissolved in 1.51 mL of DCM in a 50 mL Falcon Tube. Both solutions were kept on ice, then 250 μL of the simvastatin solution was added to the PLGA solution and sonicated by a probe sonicator for 60 s on ice to create the w/o emulsion (X kV). The w/o/w emulsion was transferred into to a 20 mL glass vial, washing the Falcon Tube with distilled water (diH_2O) to maximize particle yield. The w/o/w emulsion was stirred at 1300 rpm overnight in a fume hood to allow for organic solvent evaporation. The nanoparticles were concentrated and washed of the PVA and excess drug by 6

rounds of centrifugation at 9000 rpm for 20 min at 5 C, each, refreshing diH_2O between rounds. Particles were reconstituted in ddH2O and lyophilized and stored at -20 C until further use.

Encapsulated-BSA PLGA Nanoparticle Fabrication: Nanoparticles were prepared by a w/o/w double emulsion method. Briefly, a specified-concentration protein solution (1% w/v FITC-BSA, Sigma) in PBS was prepared while 225 mg of PLGA (50:50, MW = 7-17kDa, Sigma) was dissolved in 1.80 mL of DCM in a 50 mL Falcon Tube. Both solutions were kept on ice once fully dissolved, then 320 µL of the protein solution was added to the PLGA solution and sonicated by a probe sonicator for 35 s on ice to create a w/o emulsion. The w/o/w emulsion was transferred into to a 20 mL glass vial, washing the Falcon Tube with distilled water (diH_2O) to maximize particle yield. The w/o/w emulsion was stirred at 1300 rpm overnight in a fume hood to allow for organic solvent evaporation. The nanoparticles were concentrated and washed of the PVA and excess drug by 6 rounds of centrifugation at 9000 rpm for 20 min at 5 C, each, refreshing diH_2O between rounds. Particles were reconstituted in ddH2O and lyophilized and stored at -20 C until further use.

Fabrication of Nanofibrous Scaffolds with Nanofiber-Embedded PLGA Nanoparticles: Scaffolds with embedded PLGA nanoparticles were fabricated by a novel nanoparticle loading procedure based on the sugar sphere porogen and thermally induced phase separation method. A known mass of PLGA nanoparticles were constituted in hexane and mixed with sugar spheres to facilitate reversible hydrophilicity-mediated aggregation fo PLGA nanoparticles on the sugar sphere surface. A sugar sphere template was formed from the nanoparticle-coated sugar spheres, dried, and casted with hot, dissolved polymer solution to encapsulate the sugar spheres and

nanoparticles, as described above with thermally induced phase separation at -80C for 48 hours, where PLLA nanofibers precipitate from solution, encapsulating the PLGA nanoparticles. A desired weight (15 mg in most experiments) of PLGA nanoparticles was loaded into a 1.5 mL Eppendorf® microtube with 1 mL of hexane and 2 µL of Span80. This solution was vortexed until homogenous and added to enough sugar spheres to fabricate one cylindrical scaffold with a diameter of 21 mm and a height of 6 mm (standard size). The mixture was stirred by-hand briefly such that the nanoparticles appeared equally distributed. The coated sugar spheres and hexane solution was transferred into a Teflon mold by a transfer pipette, and scaffolds were fabricated as described.

Evaluation of Drug-Release Kinetics from Scaffold: Once fabricated, scaffolds were cut using an 8 mm biopsy punch for invitro analysis. Each scaffold slice was subject to physiologic conditions and allowed to slowly degrade. Fluorescence spectroscopy was used to measure the concentration of released encapsulant, rhodamine B or FITC-BSA. UV-Vis photospectroscopy was used to quantify simvastatin. Scaffolds were individually placed into a 48-well cell culture plate with 400 µL of PBS and kept at 37 C incubator oven on a plate shaker set to approximately 110 rpm. At each specified time point, l the PBS solution from each well was removed and transferred into a 1.5 mL Eppendorf® microtube and stored at -80C for subsequent analysis. The same volume of fresh PBS was added each time. This process was repeated for the sample collection at every time point for the duration of the experiment. A Thermo Scientific™ Varioskan™ LUX Multimode Microplate Reader was used to quantify the fluorescence. These data were exported and analyzed using Prism.

Sterilization of Biomaterial Constructs: Prior to all *in vitro* and *in vivo* work, PLLA scaffolds were sterilized by a dual-sterilization method. First, constructs were sterilized by ethylene oxide gas according to the manufacturer's protocol (Anpro). Secondly scaffolds were washed with 70% ethanol for 30 minutes, followed by washing with PBS then with cell culture media, immediately before cell seeding. The purpose of the ethanol wash is twofold – first, a secondary sterilization method, and second, to "wet" the surface of the hydrophobic PLLA scaffold prior to cell seeding.

UV-VIS Spectroscopy: Simvastatin was dissolved as describe and its absorbance was measured using a Hitatchi U-2910 spectrophotometer in a quartz cuvette. Concentration was determined using a standard curve.

Nuclear Magnetic Resonance (NMR) Spectroscopy: Synthesized polymers were characterized by nuclear magnetic resonance (NMR) spectroscopy to confirm their molecular identity and reaction efficiency. 1H spectra were recorded with a Varian MR400 spectrometer operating at 400 MHz and room temperature. Spectra were observed in deuterated chloroform ($CDCl_3$). Spectral analysis is carried out in VnmrJ (Version 4.2, Agilent) and MestReNova (Version 12.0.0-2000080, Metrelab Research).

Scanning Electron Microscopy: The surface morphology of all biomaterial constructs was observed by scanning electron microscopy (JEOL JSM-7800 FLM) with an accelerating voltage of 5 kV and working distance of 10-15 mm. Prior to observation, samples were coated with gold using a sputter coater (Desk II, Denton Vacuum Inc.).

Confocal Laser Microscopy: Fluorescently active probes were observed from substrates by confocal laser microscopy (Nikon Eclipse C1).

Statistical Methods: All data are reported as mean ± standard deviation and represent a minimum sample size of n>3. Statistical analysis was carried out in GraphPad Prism v8. Student's t-test was used to determine statistical significance of observed values between experimental groups where $p < 0.05$ was considered significant. Tukey's test was used to determine differences between group means as a single-step method to compare multiple means and determine statistical significance between. Statistical analyses were carried out under the guidance of the University of Michigan Consulting for Statistics, Computational and Analytical Research Center. In all graphics, significance is noted as: * $p<0.05$, ** $p<0.01$, ***$p<0.001$, ****$p<0.0001$.

Image Analysis: All image analysis was carried out in Fiji imaging software (Image J Image J, V 1.0.0-rc-69/1.52p). Images were imported as raw files (.TIF). Analyses were carried out using batch macros following optimized protocols.

X-ray Diffraction: A Rigaku Ultima IV Diffractometer was used to acquire small angle X-ray scattering spectra from solid phase polymer samples. X-ray generation occurs within a 2.2 kW Cu K-alpha radiation long-fine focus tube (0.4 x 12 mm) with cross beam optics. Scans are performed with a Theta/Theta wide angle goniometer from -3deg to +154deg (2 theta) at 1 degree/minute. Signal is detected with a D/teX-ULTRA high-speed detector.

Shape-Memory Thermal Cycling: A digital ceramic hot plate with temperature probe was used to regulate the temperature of water baths. Scaffolds were placed in the water bath and held under water for 30 seconds gently using forceps. After this time, the scaffolds were mechanically coiled by-hand around a 1 mm diameter metal rod (approximately 2-4 coils). This was immediately transferred into an ice bath to rapidly lock the new structure. To complete the thermal cycle and trigger shape-memory, the locked-structure film was transferred back into the 80 C water bath and rapidly found its flat, straight original shape with high integrity. This comprised one shape-memory thermal cycle and was repeated several times for some films.

Compressive Modulus Testing: Mechanical properties of scaffolds were measured using an MTS Synergie 200 mechanical tester (MTS Systems, Inc.). Scaffolds with dimensions of 15.0 mm in diameter and 3.0 mm in thickness were prepared, n=5 per pore size. Compressive modulus was defined as the initial linear modulus on the resulting stress-strain curve, with a strain rate of 1.0 mm/minute.

Subcutaneous implantation in mice: Nanofibrous scaffolds (8 mm diameter x 1.5 mm height) as described above were implanted subcutaneously into LysMCre; Td; Col1eGFP Bmice aged 8-10 weeks old. All animal procedures were performed following a protocol approved by the University of Michigan Institutional Animal Care and Use Committee (IACUC). Mice were anesthetized via isoflurane inhalation and a midsagittal incision was made on the dorsa of each mouse. On each side of the midline, two subcutaneous pockets were made by blunt dissection such that four cell-scaffold constructs were implanted into each mouse in distinct regions. Incisions were closed with surgical staples and animals were given analgesic medication (carprofen) to manage pain. Mice

were monitored closely and showed no adverse signs. At 2- and 4-weeks' time following subcutaneous implantation, mice were sacrificed by inhalation of CO2 and bilateral pneumothorax. Constructs were carefully explanted and fixed in 4% paraformaldehyde prior to subsequent histologic processing. All animal procedures were prospectively approved of by the Institutional Animal Care and Use Committee (IACUC) at the University of Michigan.

Histologic preparation of frozen sections: After fixation in 4% paraformaldehyde (PFA), PFA is exchanged for PBS for 24 hours at 4C, then the PBS is exchanged for 30% sucrose for 4 days at 4C. After 4 days, sucrose solution is removed and samples are submerged in OCT embedding compound for 4 hours, individually. After this time, allowing OCT to penetrate the porous scaffold, the constructs are arranged individually in a mold made from aluminum foil and the sample is positioned while the mold is frozen on dry ice. Once frozen, samples are stored at -80C. For histologic preparation, samples are thawed to -20C and serial sections are collected (10-12 um thickness) from a cryotome.

Visualization of frozen sections: Frozen sections are thawed from -20C and gently washed in PBS containing 0.1% Triton (PBST 0.1%) three times. A 1:1000 solution of Hoescht stain is applied according to the manufacturer's instructions to identify the nuclei of cells. Hoescth staining solution is removed by a kim wipe and the slidefs are washed three times in PBS before a coverslip is fixed with ProLong Gold Anti-Fade fixative.

Histologic preparation of paraffin Sections: Samples prepared for frozen section are thawed sufficiently to melt the OCT compound. Samples are carefully removed from OCT and submerged

in PBS and placed on a shaker. PBS is exchanged daily for 10 days to remove all OCT. Samples are dehydrated using an ethanol gradient and embedded in paraffin. Paraffin sections are cut at 5 um thickness and stained with standard histologic preparations.

CD31: Histologic sections prepared from paraffin were treated with xylene and an ethanol gradient to de-paraffinize. Antigen retrieval was performed by incubation in 10 mM citrate buffer (pH 6.0). Sections were sequentially incubated in 5% BSA for 60 minutes and with primary antibodies (CD31, 1:100) overnight at 4°C and DAB chromogen, mouthed with a coverslip and imaged with a bright field microscope (Olympus).

Bright field Microscopy: Samples were embedded in paraffin according to standard protocols and sectioned with a microtome to collect 5 um sections in the region of interest. Histologic sections prepared from paraffin were treated with xylene and an ethanol gradient to de-paraffinize. Standard protocols were followed for hematoxylin and eosin (H&E) and picrosirius red staining.

Fluorescence Microscopy: Samples were embedded in OCT embedding compound and maintained at -20degC for cryosectioning. Serial sections were cut at 10 um thickness, counterstained with DAPI (1:1,000 dilution) and imaged by confocal laser microscopy (Nikon Eclipse C1, University of Michigan School of Dentistry).

Bibliography

1. Bhattacharya, S.; Hailstone, R.; Lewis, C. L. Thermoplastic Blend Exhibiting Shape Memory-Assisted Self-Healing Functionality. *ACS Appl. Mater. Interfaces* **2020**, *12* (41), 46733–46742.

2. Lutzweiler, G.; Ndreu Halili, A.; Engin Vrana, N. The Overview of Porous, Bioactive Scaffolds as Instructive Biomaterials for Tissue Regeneration and Their Clinical Translation. *Pharmaceutics* **2020**, *12* (7), 602.

3. Kureishi, Y.; Luo, Z.; Shiojima, I.; Bialik, A.; Fulton, D.; Lefer, D. J.; Sessa, W. C.; Walsh, K. The HMG-CoA Reductase Inhibitor Simvastatin Activates the Protein Kinase Akt and Promotes Angiogenesis in Normocholesterolemic Animals. *Nat Med* **2000**, *6* (9), 1004–1010.

4. Essa, D.; Kondiah, P. P. D.; Choonara, Y. E.; Pillay, V. The Design of Poly(Lactide-Co-Glycolide) Nanocarriers for Medical Applications. *Front Bioeng Biotechnol* **2020**, *8*, 48.

5. Jenvoraphot, T.; Thapsukhon, B.; Daranarong, D.; Molloy, R.; Supanchart, C.; Krisanaprakornkit, S.; Topham, P. D.; Tighe, B.; Mahomed, A.; Punyodom, W. Tetracycline-Loaded Electrospun Poly(l-Lactide-Co-ε-Caprolactone) Membranes for One-Step Periodontal Treatment. *ACS Appl. Polym. Mater.* **2022**, *4* (4), 2459–2469.

6. Weis, M.; Heeschen, C.; Glassford, A. J.; Cooke, J. P. Statins Have Biphasic Effects on Angiogenesis. *Circulation* **2002**, *105* (6), 739–745.

7. Risco, C.; Sanmartín-Conesa, E.; Tzeng, W.-P.; Frey, T. K.; Seybold, V.; de Groot, R. J. Specific, Sensitive, High-Resolution Detection of Protein Molecules in Eukaryotic Cells Using Metal-Tagging Transmission Electron Microscopy. *Structure* **2012**, *20* (5), 759–766.

8. Pisani, S.; Genta, I.; Modena, T.; Dorati, R.; Benazzo, M.; Conti, B. Shape-Memory Polymers Hallmarks and Their Biomedical Applications in the Form of Nanofibers. *Int J Mol Sci* **2022**, *23* (3), 1290.

9. Pisani, S.; Genta, I.; Modena, T.; Dorati, R.; Benazzo, M.; Conti, B. Shape-Memory Polymers Hallmarks and Their Biomedical Applications in the Form of Nanofibers. *International Journal of Molecular Sciences* **2022**, *23* (3), 1290.

10. Swanson, W. B.; Omi, M.; Woodbury, S. M.; Douglas, L. M.; Eberle, M.; Ma, P. X.; Hatch, N. E.; Mishina, Y. Scaffold Pore Curvature Influences MSC Fate through Differential Cellular Organization and YAP/TAZ Activity. *Int J Mol Sci* **2022**, *23* (9), 4499.

11. Lagreca, E.; Onesto, V.; Di Natale, C.; La Manna, S.; Netti, P. A.; Vecchione, R. Recent Advances in the Formulation of PLGA Microparticles for Controlled Drug Delivery. *Prog Biomater* **2020**, *9* (4), 153–174.

12. Abbasi, N.; Hamlet, S.; Love, R. M.; Nguyen, N.-T. Porous Scaffolds for Bone Regeneration. *Journal of Science: Advanced Materials and Devices* **2020**, *5* (1), 1–9.

13. Santoro, M.; Shah, S. R.; Walker, J. L.; Mikos, A. G. POLY(LACTIC ACID) NANOFIBROUS SCAFFOLDS FOR TISSUE ENGINEERING. *Adv Drug Deliv Rev* **2016**, *107*, 206–212.

14. Capuana, E.; Lopresti, F.; Ceraulo, M.; La Carrubba, V. Poly-l-Lactic Acid (PLLA)-Based Biomaterials for Regenerative Medicine: A Review on Processing and Applications. *Polymers (Basel)* **2022**, *14* (6), 1153.

15. La Carrubba, V.; Pavia, F. C.; Brucato, V.; Piccarolo, S. PLLA/PLA Scaffolds Prepared via Thermally Induced Phase Separation (TIPS): Tuning of Properties and Biodegradability. *Int J Mater Form* **2008**, *1* (1), 619–622.

16. Ghersi, G.; Pavia, F. C.; Conoscenti, G.; Mannella, G. A.; Greco, S.; Rigogliuso, S.; La, C. V.; Brucato, V. PLLA Scaffold via TIPS for Bone Tissue Engineering. *Chemical Engineering Transactions* **2016**, *49*, 301–306.

17. Guo, P.; Hu, B.; Gu, W.; Xu, L.; Wang, D.; Huang, H.-J. S.; Cavenee, W. K.; Cheng, S.-Y. Platelet-Derived Growth Factor-B Enhances Glioma Angiogenesis by Stimulating Vascular Endothelial Growth Factor Expression in Tumor Endothelia and by Promoting Pericyte Recruitment. *Am J Pathol* **2003**, *162* (4), 1083–1093.

18. Raica, M.; Cimpean, A. M. Platelet-Derived Growth Factor (PDGF)/PDGF Receptors (PDGFR) Axis as Target for Antitumor and Antiangiogenic Therapy. *Pharmaceuticals (Basel)* **2010**, *3* (3), 572–599.

19. Pfau, M. R.; McKinzey, K. G.; Roth, A. A.; Grunlan, M. A. PCL-Based Shape Memory Polymer Semi-IPNs: The Role of Miscibility in Tuning the Degradation Rate. *Biomacromolecules* **2020**, *21* (6), 2493–2501.

20. Rodrigues, N.; Benning, M.; Ferreira, A. M.; Dixon, L.; Dalgarno, K. Manufacture and Characterisation of Porous PLA Scaffolds. *Procedia CIRP* **2016**, *49*, 33–38.

21.Swanson, W. B.; Omi, M.; Zhang, Z.; Nam, H. K.; Jung, Y.; Wang, G.; Ma, P. X.; Hatch, N. E.; Mishina, Y. Macropore Design of Tissue Engineering Scaffolds Regulates Mesenchymal Stem Cell Differentiation Fate. *Biomaterials* **2021**, *272*, 120769.

22. Hasani-Sadrabadi, M. M.; Sarrion, P.; Nakatsuka, N.; Young, T. D.; Taghdiri, N.; Ansari, S.; Aghaloo, T.; Li, S.; Khademhosseini, A.; Weiss, P. S.; Moshaverinia, A. Hierarchically Patterned Polydopamine-Containing Membranes for Periodontal Tissue Engineering. *ACS Nano* **2019**, *13* (4), 3830–3838.

23. Vozzi, G.; Flaim, C.; Ahluwalia, A.; Bhatia, S. Fabrication of PLGA Scaffolds Using Soft Lithography and Microsyringe Deposition. *Biomaterials* **2003**, *24* (14), 2533–2540.

24. Cruz, K. P.; Patricio, B. F. C.; Pires, V. C.; Amorim, M. F.; Pinho, A. G. S. F.; Quadros, H. C.; Dantas, D. A. S.; Chaves, M. H. C.; Formiga, F. R.; Rocha, H. V. A.; Veras, P. S. T. Development and Characterization of PLGA Nanoparticles Containing 17-DMAG, an Hsp90 Inhibitor. *Frontiers in Chemistry* **2021**, *9*.

25. Chen, J.; Hamilton, L. E.; Mather, P. T.; Henderson, J. H. Cell-Responsive Shape Memory Polymers. *ACS Biomater. Sci. Eng.* **2022**, *8* (7), 2960–2969.

Appendix A

Biomaterial Molecular Characterization

This appendix contains the NMR spectra for the synthesized biomaterials and one synthesized TSM membrane.

A.1 PLLA Characterization

100 mg of PLLA was dissolved in 500 µL of deuterated chloroform.

NMR:

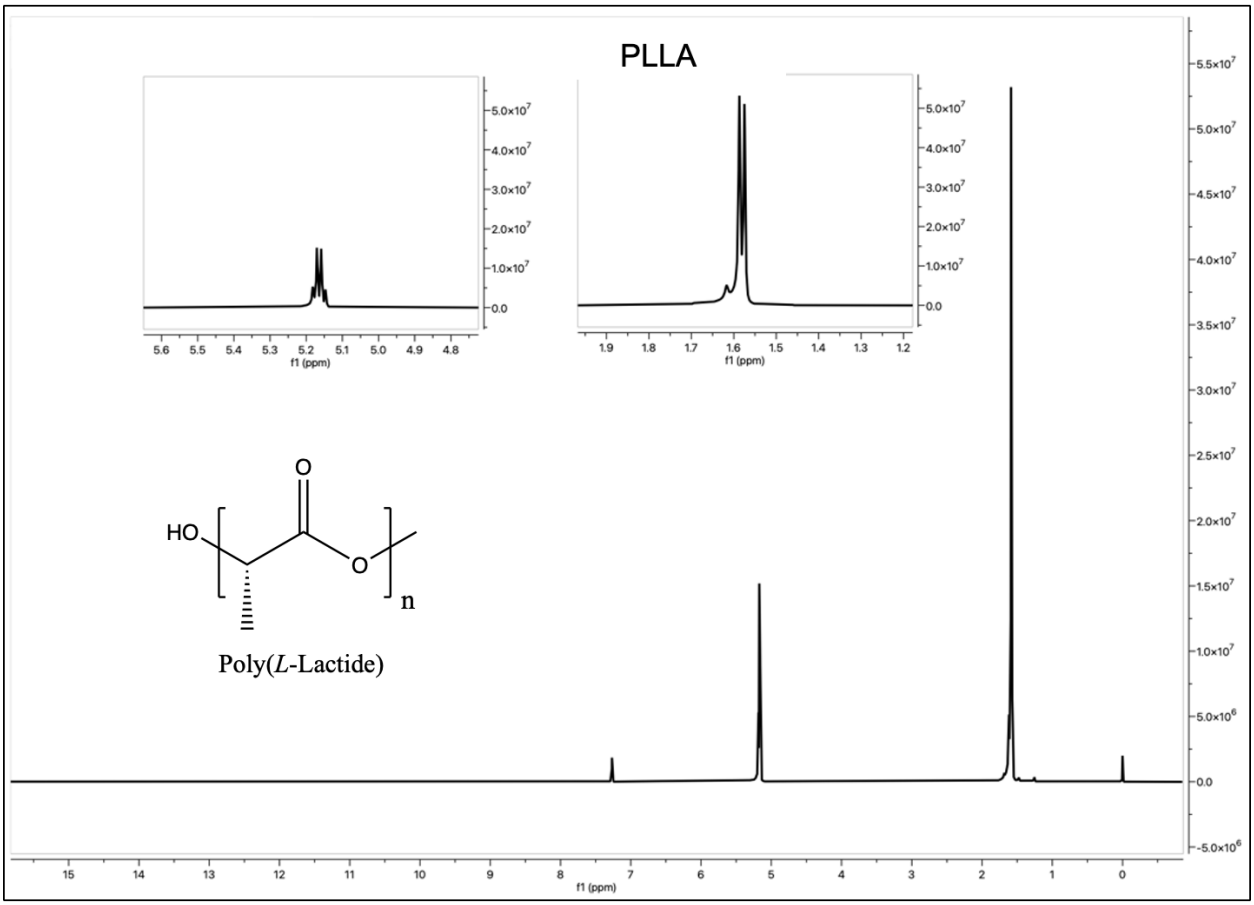

A.2 PCL Characterization

100 mg of each synthesized PCL polymer was dissolved in 500 µL of deuterated chloroform.

NMR:

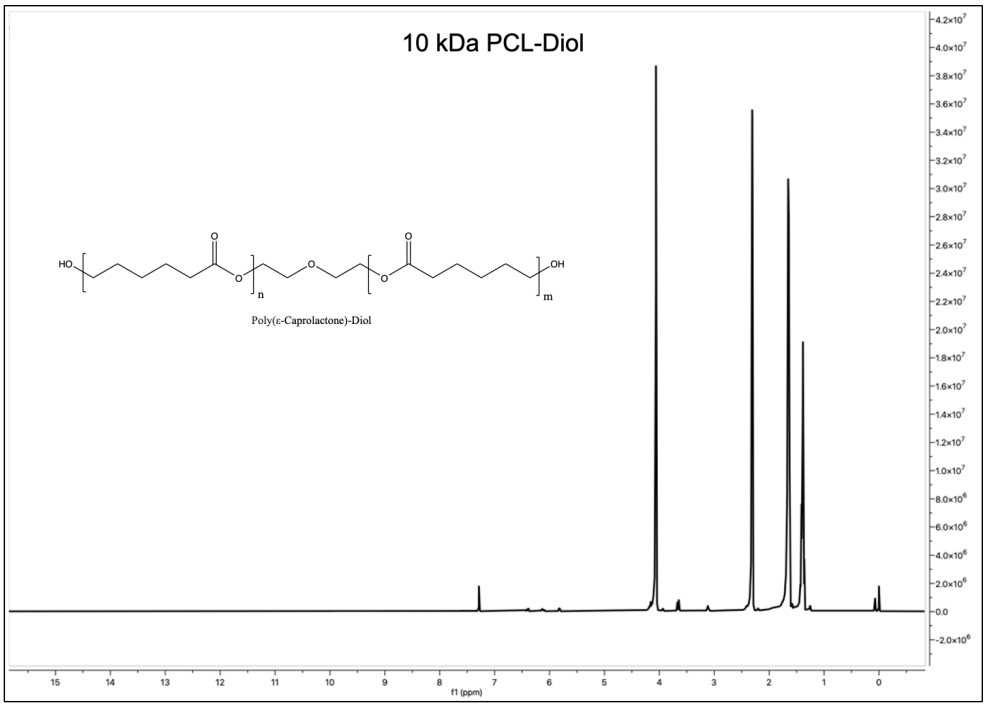

NMR:

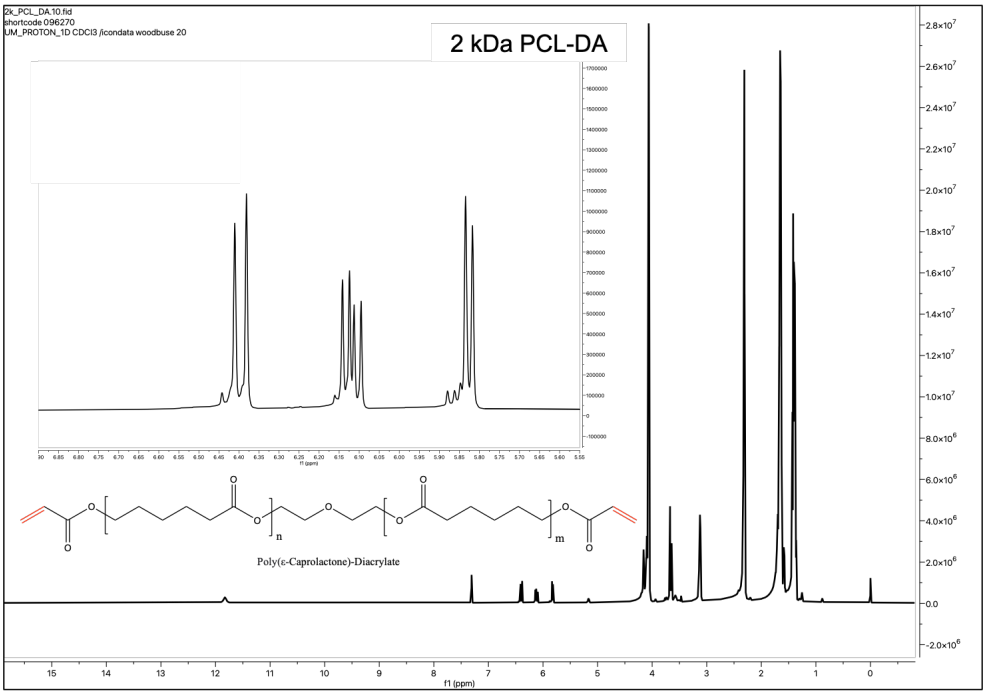

NMR:

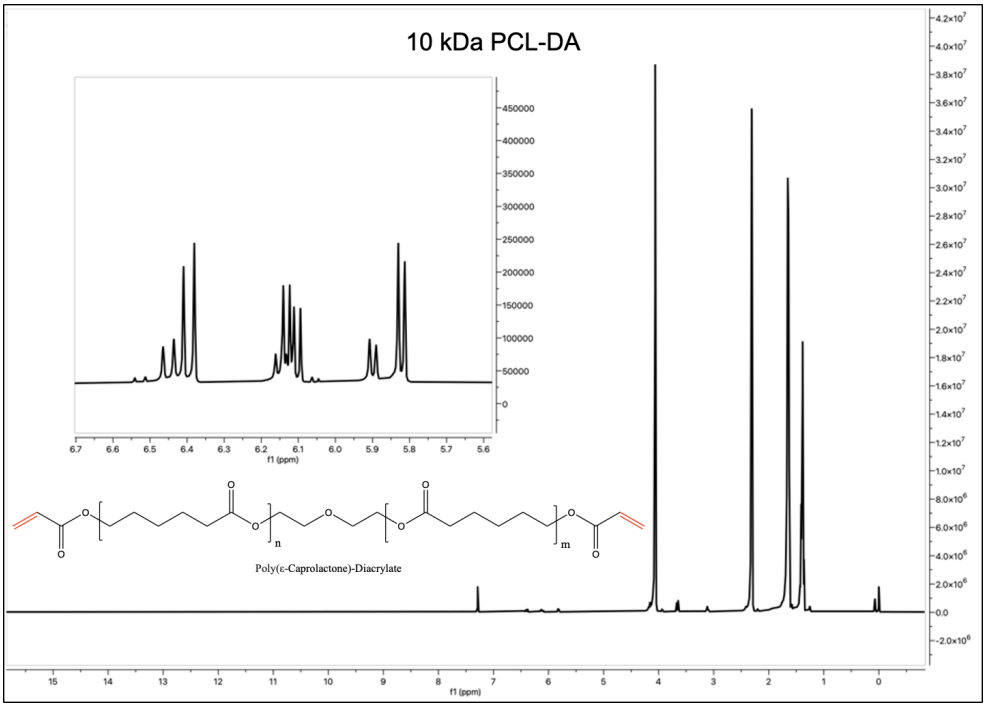
10 kDa PCL-DA
Poly(ε-Caprolactone)-Diacrylate
f1 (ppm)

NMR:

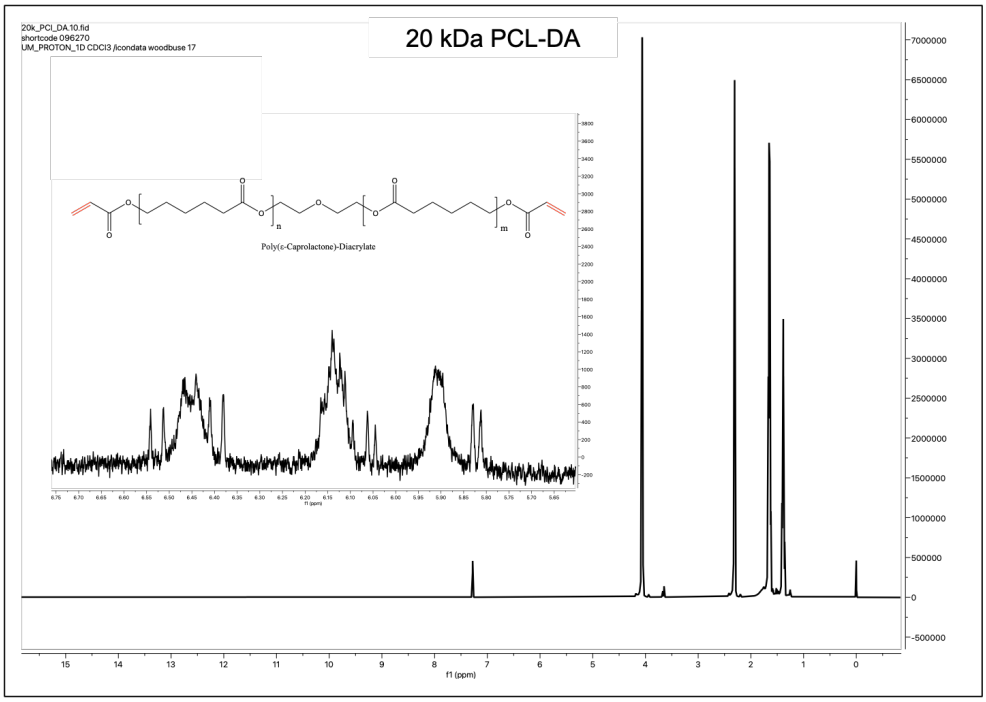
20k_PCL_DA.10.fid
shortcode 096270
UM_PROTON_1D CDCl3 /icondata woodbuse 17
20 kDa PCL-DA
Poly(ε-Caprolactone)-Diacrylate
f1 (ppm)

A.3 PLGA-DA Characterization

100 mg of synthesized PLGA-DA was dissolved in 500 µL of deuterated chloroform.

NMR:

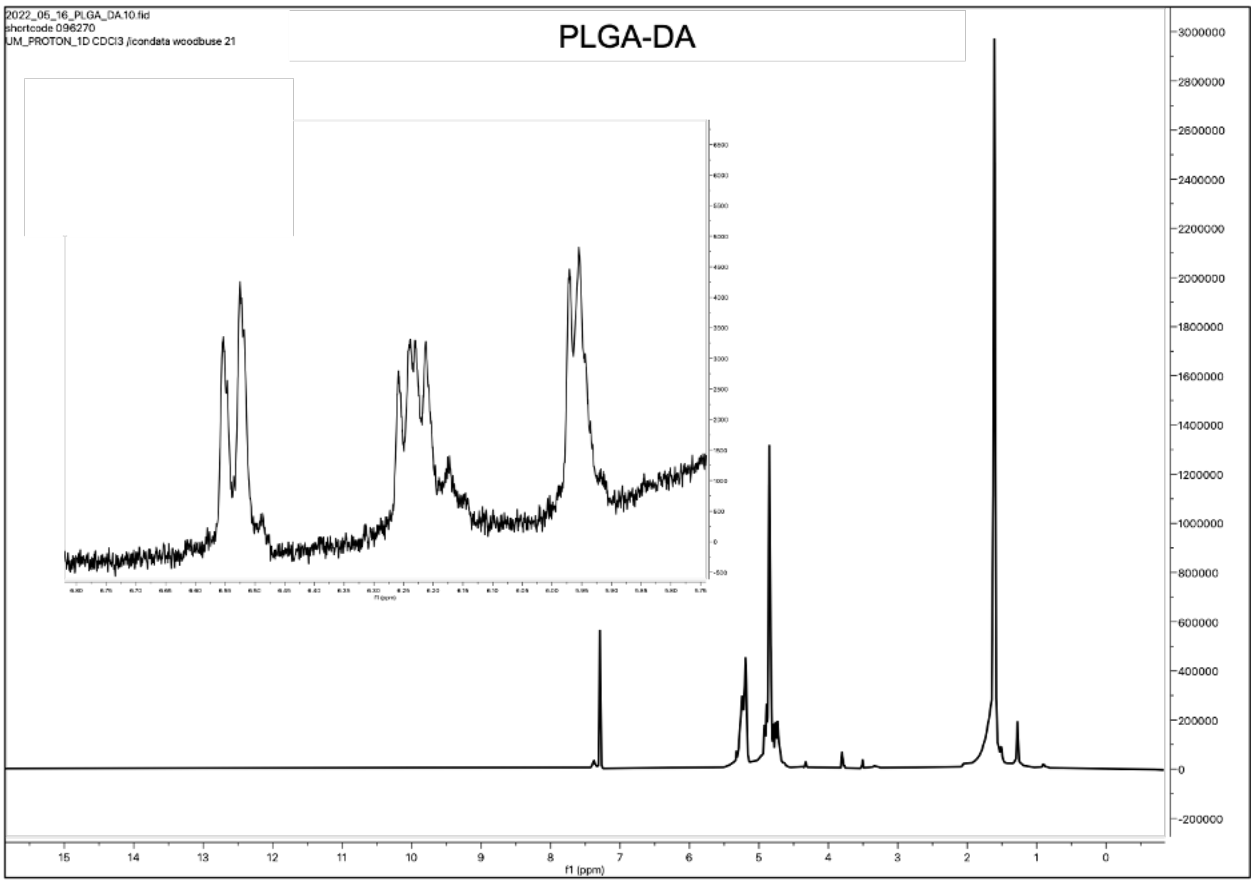

A.4 Characterization of an Optimized Thin Film Containing all Biomaterials

A vertical cross-section of the TSM biomaterial thin film was taken and weighed approximately 200 mg. This was dissolved in 1000 µL of deuterated chloroform and 500 µL was used for spectroscopic characterization.

NMR: